The Dissertation Committee for Elizabeth Stacia Curry-Logan Certifies that this is the approved version of the following dissertation:

Modes of deformation in ice in dynamic regions: applications to basal crevasses and calving

Committee:

Luc Lavier, Co-Supervisor

Ginny Catania, Co-Supervisor

Marc Hesse

Omar Ghattas

Doug MacAyeal

Modes of deformation in ice in dynamic regions: applications to basal crevasses and calving

by

Elizabeth Stacia Curry-Logan, B.A.

Dissertation

Presented to the Faculty of the Graduate School of

The University of Texas at Austin

in Partial Fulfillment

of the Requirements

for the Degree of

Doctor of Philosophy

The University of Texas at Austin

December 2015

Dedication

For my wife and my family.

Acknowledgements

Many people have contributed to this dissertation in many ways. I foremost must thank Luc Lavier for always sticking with me, and for telling me to quit freaking out all the time. Ginny Catania for taking me under her wing, providing me with data, ideas, and tons of advice and support. My committee members for being there when I needed them and dedicating their time to supervising my research. Eunseo and Eh for teaching me so much about code and numerical modeling. Philip Guererro, Judy Sansom, and Nancy Hard for being the backbone to UTIG and enabling my studies to run smoothly. My office mates Sebastian and Bud for providing stimulating conversation and numerous procrastination activities, and Cassie and Annie for giving me distractions. Eleanor Picard for being there when I needed a break. All of my fellow graduate students with whom I have shared frustrations and hilarity. And finally my ever-patient wife Tina and my mother, father, and brother who have always had faith in me, especially when I had no faith in myself.

Modes of deformation in ice in dynamic regions: application to basal crevasses and calving

Elizabeth Stacia Curry-Logan, PhD

The University of Texas at Austin, 2015

Co-Supervisors: Luc Lavier and Ginny Catania

Calving remains one of the most important yet unresolved aspects of glacier and ice sheet flow. Providing better constraints on global mean sea level rise will depend on our ability to simulate the dynamic flow of ice as it is discharged into the oceans. The work of this dissertation focuses on the important role basal crevasses play in the discharge of ice from glaciers and ice streams and how we can better model the formation and development of these features, particularly with regard to ice rheology during failure. First we make use of a large amount of ice penetrating radar data to image and understand the geometry and location of these features along the grounding line of the Siple Coast, in Antarctica. These data motivate the use of a thin-elastic beam approximation to the stresses that promote failure there, and the model is applied to all grounding lines across Antarctica, producing order-of-magnitude predictions where basal crevasses have already been observed. The simplicity of this model leads to the development of a more complex numerical model capable of visco-elasto-plastic simulation, DynEarthSol3D (DES), which performs the only time-dependent benchmark test designed for higher-order Stokes models. DES performs reasonably well against purely viscous numerical models and executes several experiments with idealized geometries exploring the roles that ice thickness and grounding line curvature play in the

formation of basal crevasses in elastoplastic ice. Finally, with the implementation of a ductile-brittle transition zone based on longitudinal strain rate, we model the development of grounding line basal crevasses using visco-elasto-plastic rheology. Here we explore the roles that ice thickness and basal melting play in the formation and development of basal crevasses in ice as it is advected from resting on bedrock to floating in the ocean. We find that the inclusion of an extra measure of weakening to simulate the infiltration of buoyant ocean water in the basal crevasses is a crucial mechanism in developing the failure pattern seen in the floating portions of Thwaites Glacier and other glaciers around the world. The features that we simulate are truly semi-brittle, in that they require both viscous and elastic components of stress and a failure mechanism to develop.

Table of Contents

List of Tables

List of Figures

Introduction

In the coming centuries the need to understand how the world environment is evolving due to climate change will be great. The impacts from our changing environment are already felt everywhere, from the coasts where extreme weather costs us billions of dollars in damage and lives lost, to the interiors where drought threatens our ability to provide food reliably. To face these problems policy makers as well as the general public need information with ever-increasing levels of certainty. Indeed, the recalcitrance of our society to act in ways that could mitigate the far-reaching consequences of climate change reflects the inertia of the current economic and political systems in place – systems that demand more certainty in climate forecasts every year.

While the 2007 Intergovernmental Panel on Climate Change (IPCC) left little doubt that anthropogenic climate change is currently underway, the report exposed our lack of understanding surrounding the expected changes in ice bodies around the world. The projections of global mean sea level rise presented then did not incorporate the anticipated contributions of glaciers and ice sheets under a warming climate. Emphasized in particular was our need to evaluate the expected rapid changes in the extent of ice bodies on the decadal to century scale. Since 2007 researchers have largely risen to this challenge, developing more sophisticated numerical models for the prediction of ice flow and extent, with the 2013 IPCC report now presenting the findings of glacier and ice sheet contributions to sea level rise.

Largely absent from these findings however is the role that rapid dynamical changes are likely to play in expected sea level rise. While a large suite of models exists to predict the oceanic and atmospheric responses to increased greenhouse gas emissions, only one model (Jevrejeva et al., 2012b) included the effects of ice that is not assumed to be at steady state under the climate warming scenarios tested. This is largely due to the numerical challenges associated with the simulation of ice: the material exhibits features typifying both a solid and non-Newtonian liquid. While most scientists have chosen to formulate the ice flow problem in terms of fluid flow, the remaining uncertainty in the prediction of ice extent stems from the dual nature of ice as both a solid and fluid. Those changes that occur on the decade to century timescale result from a complex interaction of processes occurring at the ice-ocean interface that affect the ice flow, including the melting of ice in contact with ocean water and the mechanical removal of ice via iceberg detachment, called calving. An attempt to provide a projection of sea level rise for Antarctica with the inclusion of rapid dynamical changes that result from the interplay of these features of ice flow resulted in an estimate of -.018 to .2 m of sea level equivalent (IPCC AR5, 2013), and cited a lack of process-based models capable of such a projection for the large range. The work of this dissertation aims to further our understanding of the link between dynamical ice flow and the resulting failure patterns in ice that lead to calving.

Calving or basal melting?

Whereas previously calving was thought to be the dominant mass loss mechanism in Antarctica, accounting for 75% of all ice flux to the ocean (Jacobs et al., 1992), more recent estimates revised that contribution to essentially half of all ice discharged into the ocean, splitting the budget with basal melting (Rignot et al., 2013; Liu et al., 2015). Despite this reduction, calving remains an important aspect of the mechanisms by which global mean sea level will rise. Moreover, calving and basal melting do not act as separate processes: Liu et al. [2015] showed that in Antarctica, regions of high basal melt coincided with regions of high calving, suggesting that the two are intimately linked and must be accounted for simultaneously in prognostic simulations of ice flow. One example that illustrates the connection between ice melting, calving, and ice flow is the Larsen B Ice Shelf, which collapsed over a matter of weeks in February and March of 2002. While the ice shelf was already riddled with cracks on both the bottom and surface of the ice, the additional destabilizing mechanism of melt water ponds at the ice surface led to the spectacular disintegration of the ice shelf, where the ponds at the surface acted as additional loads on top of the ice and aided in the full thickness penetration of fractures (Scambos et al., 2003; Sergienko and MacAyeal, 2005; Glasser and Scambos, 2008). In addition to the extra force they provided directly in propagating surface cracks, the melt water ponds provided flexural forces that likely aided in the propagation of basal cracks to the surface (MacAyeal and Sergienko, 2013). The result of the interplay then between ice shelf melting and fracture was the complete loss of the ice shelf and the buttressing forces it provided to the glaciers that fed it from the land. Those glaciers accelerated by as much as eightfold after the loss of the ice shelf (Rignot et al., 2004; Rott et al., 2011).

Other areas where ice melting and calving have interacted to produce ice acceleration and thinning have occurred in the Northeast sector of Greenland (Khan et al., 2014) and in the West and Northwest sectors of Greenland (Csatho et al., 2014). These are areas where either atmospheric warming episodes or the intrusion of warm ocean waters into fjords led to the rapid retreat of glaciers. Thus the development of a numerical model to simulate the prognostic behavior of glaciers that includes both melting and calving should be the goal for a more complete future picture of ice sheet and glacier behavior. But while ice sheet melting is a relatively easy feature to incorporate in numerical models, ice failure is not, and remains to be implemented in large-scale prognostic ice sheet models.

Calving then and now

The earliest attempts to formulate a quantitative approach to calving have focused on the role that individual fractures or crevasses played in the detachment of icebergs. These formulations often assumed that the depth to which a crevasse will propagate is at a location where the forces tending to open a crevasse are balanced by those tending to close it. Nye [1955, 1957], Weertman [1973], and van der Veen [1998a,b] all adopt some form of this assumption, with different aspects considered in each. For example, while Nye's formulation depends only on strain rate, Weertman included the effects that the geometry of the crevasse and concentrations of stress at the crack tip have on the crevasse depth. Van der Veen extended these concepts by incorporating Linear Elastic Fracture Mechanics as a failure criterion and deriving crevasse depth models for both mode I and II fractures. But while these models perform reasonably well in matching observed fields of crevasse depths, they remain static formulations that do not describe how the crevasse evolves over time, eventually creating an iceberg, and further give no formulation for characterizing the spacing of crevasses, which ultimately determines iceberg size and calving rate.

More recent models of ice failure have made use of damage mechanics to simulate the time dependent failure of ice (Pralong et al., 2006; Duddu and Waisman, 2013a). These models formulate the mechanical degradation of ice in terms of a critical strain that is correlated with damage. Once a critical damage is reached the ice is considered to effectively have no strength, and loses its load bearing capacity. The subsequent weakening of ice is then wrapped into the viscosity term, where damaged ice leads to faster ice flow via decreased viscosity. While Duddu et al. [2013b] have simulated the time dependent failure of ice using this framework, researchers have yet to simulate ice failure for larger ice bodies throughout time. Borstad et al. [2012] used damage mechanics to assess the stability of the Larsen B Ice Shelf prior to collapse, but work with this framework has not been used in a dynamic, time-dependent way anywhere.

One very recent model used a discrete element method to simulate the generation of icebergs from Helheim Glacier in Southeast Greenland (Bassis and Jacobs, 2014). This model simulated intact ice as a tight packing of particles bound together by elastic forces. Once the force between any two given particles exceeded some yield strength the ice was considered broken. This method has successfully reproduced a range of calving styles, from the frequent serac-style mode where ice detaches in small chunks frequently, to the tabular iceberg mode, where large, stable blocks of ice detach sporadically. While this method was largely successful, it only incorporated elastic stresses in the ice – whereas many researchers have formulated calving laws for ice based on a viscous stress assumption. Thus a model that simulates the visco-elastic deformation of ice while incorporating a realistic and time-dependent failure criterion would be a very powerful tool, helping improve our predictions of iceberg calving and ultimately sea level rise. The work of this dissertation set out to accomplish this task.

Chapter 1 explores how basal ice imaged in ground-penetrating radar fractures as it traverses the grounding line in the Siple Coast of Antarctica. Basal fractures there extend deep into the interior of the ice, with a relatively regular spacing. We show that ice thickness correlates inversely with fracture size, and that fracture heights can be estimated using a thin-elastic beam approximation. This method is tested at the grounding line of every major ice shelf in Antarctica, including Pine Island and Thwaites Glaciers in the Amundsen Sea embayment, and good agreement between the method and previously observed fractures is found. This confirms our belief that in order to accurately estimate the size of crevasses elasticity must be incorporated into the ice.

The finding in Chapter 1 that elasticity must be included in the stress evaluation motivates Chapter 2, wherein we explore the role that the assumption of different rheologies has on patterns of ice failure and flow. We present a new numerical model, DynEarthSol3D (DES), which can simulate the time-dependent, self-consistent failure of ice. We examine the results of DES in a benchmark test designed for higher-order stress models and find that, despite its complexity and fundamental difference between those viscous Stokes models for which the test was intended, DES performs reasonably well and is suitable for ice simulation. Because our findings in Chapter 1 indicated that the formation of basal crevasses, which can eventually propagate through the thickness of the ice to form icebergs, depends on the bending of the ice and the local ice thickness, we tested basal crevasse formation for a suite of parallel-sided slabs of different thickness undergoing different degrees of bending. We found that the mean basal crevasse spacing increases with increasing ice thickness and decrease with increasing tilt angle. These experiments were executed for ice with an elasto-plastic rheology and Mohr-Coulomb failure criterion, and helped us determine reasonable values for failure parameters.

Chapter 3 takes the simulations from chapter 2 one step further and simulates idealized glaciers of different thicknesses as they advect over a fixed grounding line, where stresses are applied. These experiments are carried out for three different ice thicknesses with four different rates of basal melting applied uniformly, on Maxwell viscoelastic and visco-elasto-plastic ice. We find that basal melting results in velocity increases due solely to increases in ice thickness gradient and that thinner ice produces relatively wider spaced crevasses. We employed a strain rate threshold in the case of visco-elasto-plastic ice to determine the rheology at any given element, where ice with a high strain rate behaves in a brittle fashion while slowly deforming ice behaves in a ductile manner. Lastly, we simulated Thwaites Glacier and observed the formation of basal crevasses and boudins there.

Chapter 1: A novel method for predicting fracture in floating ice

Liz Logan[1], Ginny Catania[1,2], Luc Lavier[1,2], and Eunseo Choi[3]

[1] Department of Geological Sciences, University of Texas at Austin

[2] Institute for Geophysics, University of Texas at Austin

[3] Center for Earthquake Research and Information, University of Memphis

* Chapter 1 has been published as is in the Journal of Glaciology, doi:10.3189/2013JoG12J210

ABSTRACT

Basal crevasses may play an important precursory role in determining both the location and propagation of rifts and iceberg dimensions. For example, icebergs calved recently from Thwaites Glacier have the same width as surface undulations strengthening the connection between basal crevasses, rifting, and calving. We explore a novel method for estimating the heights of basal crevasses formed at the grounding lines of ice shelves and ice streams. We employ a thin-elastic beam (TEB) formulation and tensional yielding criterion to capture the physics of flexed ice at grounding lines. Observations of basal crevasse heights compare well with model predictions in the Siple Coast of the Ross Ice Shelf. We find that the TEB-method is most accurate in areas of low strain rate. We also test the method in other areas of Antarctica to produce order of magnitude maps of grounding line basal crevasses and find general agreement to reported observations assuming basal crevasses develop in spatio-temporal sequence and are advected downstream. This method is computationally cheap and could be relatively easy to implement into damage-oriented large-scale ice models which aim at physically simulating calving and fracture processes.

1. INTRODUCTION

Fast-moving glaciers and ice streams discharge across their grounding lines into ice shelves or floating tongues that provide a retarding force for grounded ice flowing into the ocean. There have been several recent observations of collapse or retreat of these floating regions, including the Wilkins, Wordie, and Larsen B Ice Shelves, as well as Thwaites Glacier (Doake and Vaughan, 1991; Joughin and others, 2008; Scambos and others, 2009; Braun and Humbert, 2009; MacGregor and others, 2011). One spectacular example is the collapse of the Larsen B Ice Shelf, which resulted in the acceleration of glaciers that fed the ice shelf by as much as 5 times their original flow speeds—an acceleration that has since largely been sustained over the past decade (Scambos and others, 2004; Rott and others, 2011). Ice shelf disintegration and calving are intrinsically linked to the formation of ice shelf fractures, including surface and basal crevasses (Doake and others, 1998; MacAyeal and others, 2003; Scambos and others, 2003; Glasser and Scambos, 2008; Scambos and others, 2009). Crevasses form in response to—and thus relieve—locally high tensional stresses, and their presence affects the strength of ice (Glasser and Scambos, 2008; McGrath and others, 2012b). Thus to accurately predict calving in numerical models it may be necessary to first understand the circumstances and patterns under which both surface and basal crevasses initialize, propagate, and are advected (Albrecht and Levermann, 2012; Duddu and Waisman, 2012). Accurate and computationally inexpensive methods for predicting crevasse heights can yield extra insight on the timing and predicted calving style of ice shelves, as the time it takes for a crevasse to penetrate the thickness of the ice directly affects the calving rate (Kenneally and Hughes, 2006). State-of-the-art ice sheet models either use empirical and heuristic calving laws which do not capture all types of calving behavior and are not physically deterministic (e.g., Alley and others, 2008; Albrecht and others, 2011) or else neglect the calving problem entirely (e.g., Rutt and others, 2009). In this context then the connection between predictive calving laws and crevassing is apparent: the fracture of ice represents the crux of the calving process.

Few have devoted study solely to basal crevasses. Jezek and Bentley (1983) showed basal crevasses to be nearly ubiquitous in the Ross Ice Shelf (RIS). More recent studies have shown basal crevasses to be present in several locations of the Larsen C Ice Shelf (Luckman and others, 2012; McGrath and others, 2012), on Pine Island Glacier (Bindschadler and others, 2011; Vaughan and others, 2012), the Filchner-Ronne Ice Shelf (Rist and others, 2002), and the Amery Ice Shelf (McGrath and others, 2012b). Basal crevasses have likely played a significant role in the development of rifts which preceded the disintegration of the Wilkins Ice Shelf (Braun and Humbert, 2009). In that case, merging ice streams of different thickness resulted in a bending moment due to buoyancy contrasts which promoted the formation of fractures and rifts. In addition, basal crevasses can be more than one hundred meters wide at their bases making them extremely vulnerable to plumes of warm ocean water which can widen the crevasse walls through melt (Weertman, 1973; Van der Veen, 1998a; Khazendar and Jenkins, 2001; Sergienko and MacAyeal, 2005; Bindschadler and others, 2012; McGrath and others, 2012; Vaughan and others, 2012). Finally, two adjacent basal crevasses can create a concave-down ridge between the two basal crevasse crack tips whereby the induced flexure creates corresponding surface crevasses (Luckman and others, 2012; McGrath and others, 2012a, 2012b; Vaughan and others, 2012). Given their seeming ubiquity in floating ice, it is reasonable to suggest that basal crevasses likely existed in the Larsen B Ice Shelf, and further—as McGrath and others [2012a,2012b] show—played some role in the initiation of surface crevasses which subsequently filled with melt water and led to shelf disintegration. Clearly then, basal crevasses affect the stability of ice shelves, and deserve focus in light of their ubiquity and ability to damage and localize ice shelf melting, and thus impact calving and sea level rise.

In this paper we focus on basal crevasses which initiate at grounding lines. The grounding lines of glaciers and ice shelves are dynamic, and their location can change in response to large scale mass losses or gains. A great effort by many researchers has been undertaken recently to understand the physics and dynamics of this crucial region (e.g. Conway and others, 1999; Rignot and Jacobs, 2002; Shepherd and others, 2001; Schoof 2007; Jacobs and others, 2012) and state-of-the-art ice-dynamic models continue to develop numerical techniques for appropriately capturing the stresses in this region (e.g. Hindmarsh R, 2004; Le Meur and others, 2004; Favier and others, 2012). In this paper we explore a simple method aimed at reconciling the observations of basal crevasses—fractures often assumed to be expressions of brittle deformation—seen at grounding lines where viscous ice dynamics are important. Our method can provide an upper bound for predicting the heights of basal crevasses formed at grounding lines motivated by our assumption that these particular features form in response to the bending that occurs as ice begins to float and achieves hydrostatic equilibrium. This method is motivated by a two-part hypothesis: first, that the extensional stresses here can be approximated by a thin elastic beam formulation (TEB: Timoshenko and Woinowsky-Krieger, 1959; Bodine and Watts, 1979; Turcotte and Schubert, 1982), and second, that yielding occurs by brittle mode I failure (Schulson and Duval, 2009: chapter 10). We test our hypotheses against observations of basal crevasses detected from ice-penetrating radar in the Siple Coast region of the Ross Ice Shelf (RIS), and extend the test to other regions of interest in Antarctica. This method is computationally cheap and could be easy to incorporate into any damage formulation or large-scale ice-dynamic model. Further, areas of TEB-model failure indicate that a more complicated constitutive model may be appropriate. Thus using this method to delineate areas of misfit provides modelers with a metric that can help optimize the use of computationally expensive numerical techniques.

2. METHODS

We observed basal fracture diffraction patterns in the Siple Coast region of the RIS using ice-penetrating radar and modeled their propagation heights. Basal crevasses were imaged using a ground-based radar system towed along 19 separate transects (Figure 1A). The radar data (Figure 1B) were acquired and processed as described in Catania and others (2010). We identified basal crevasses in the data by picking the apex of the hyperbolic diffraction near the ice-bed interface commonly assumed to result from basal crevasses (e.g., Jezek and Bentley, 1983). We also use Landsat-7 ETM+ band 8 imagery (15 m resolution; Cavalieri and Alvaro, 2009) to observe topographic depressions commonly thought to result from basal crevasses (Bindschadler and others, 2012; McGrath and others, 2012; Vaughan and others, 2012) at the Thwaites Glacier grounding line to examine the connection between basal crevasses and calving in this area.

2.1 Loading via flexure

Much of the previous work done to understand the formation of both surface and basal crevasses has proceeded based on the assumption that crevasses are mode I fractures resulting from high extensional stress (e.g., Weertman, 1973; Van der Veen, 1998a, 1998b; Rist and others, 2002; Mottram and Benn, 2009; Luckman and others, 2012; McGrath and others, 2012). When these formulations have been tested against in-situ crevasse depth measurements, the local background stress (often approximated as the stress which produced the crack) must be estimated, and is typically assumed to be a viscous stress given by the local strain-rate field. In dynamic regions—such as glacier termini (Mottram and Benn, 2009) and highly straining areas of floating ice shelves (Rist and others, 2002; Luckman and others, 2012; McGrath and others, 2012)—this assumption is largely justified and has been fairly successful in reproducing observed surface and basal crevasse depths and heights. Along the Siple Coast grounding line (particularly the slow-moving areas of Siple Dome and Kamb Ice Stream, KIS) the low strain rates beg another model (Figure 1A, the second invariant of strain rate calculated from Rignot and others, 2011). Similarly, we assume that basal crevasses in the Siple Coast result from high extensional stresses, but we explore the idea that flexure produces sufficiently high stresses for the ice to fail. This formulation requires that crevasses never extend higher than half the thickness of the ice at the grounding line where they initiate, as they would be propagating into ice which is in compression rather than extension (our data show this to be the case).

Others (e.g., Hughes, 1983; Jezek and Bentley, 1983; Langhorn and Haskell, 2004) have posited that grounding line basal crevasses result from cyclic tidal flexure. Correspondingly, our ice-penetrating radar data show that basal crevasses only appear at and downstream of the grounding line, as the grounding line represents a hinge in the tidal flexing process. Flexural bending that occurs due to tides has been well-documented (Vaughan, 1995; Horgan and Anandakrishnan, 2006; Brunt and others, 2010a, 2010b) and kinematic GPS from our campaign show that in this region the tides flex the grounding line by approximately 1 m (Figure 1C). However, the most striking topographic feature in this area is the slope-break, an ice surface feature which results from the ice decoupling from the bed and achieving hydrostatic flotation (Horgan and Anandakrishnan, 2006; Sayag and Worster, 2011; Schoof, 2011). Spatial changes in ice surface slope due to spatial changes in basal boundary conditions (resting on solid material to floating on water) can be seen in both elastic and viscous media (Sayag and

Worster, 2011; Schoof, 2011). The Glen-derived (1955, 1957) viscous creep law used in other studies (Mottram and Benn, 2009; McGrath and others, 2012) to estimate the stress field yields stresses an order of magnitude smaller than stresses calculated via beam flexure and slope break. Curvatures derived from tidal bending versus those due to hydrostatic flotation reveal that slope-break-derived curvatures are 1 to 2 orders of magnitude larger than those calculated by a 1 m tidal uplift. Thus we propose that a flexed thin elastic beam formulation may capture the loading mechanism responsible for the basal crevasses we imaged.

Having properly motivated our use of the thin-beam stress formulation (ice thickness << bending wavelength and the slope-break deflection is sufficiently small), the longitudinal stress induced by a flexed beam has the following form:

$$\sigma_{xx} = \kappa\, y\, \omega''(x) \qquad (1)$$

where y is the positive depth in the beam below the neutral plane (Figure 2), $\omega''(x)$ is the topographic curvature in the x-direction, and

$$\kappa = E\,(1 - \nu^2) \qquad (2)$$

where E and ν are the Young's modulus and Poission's ratio of the material (Timoshenko and Woinowsky-Krieger, 1959; Bodine and Watts, 1979; Turcotte and Schubert, 1982). Reported Young's modulus values vary depending on field- and lab-derived measurements, and we test values between 1 and 10 GPa (Vaughan, 1995; Schulson and Duval, 2009). We assume Poisson's ratio to be ν = .325 (Gammon and others, 1983; Schulson and Duval, 2009).

Curvature is simply the second derivative of the ice topography field, and we interpolate the surface elevation field normal to the grounding line (Lebrocq and others, 2010) to calculate its second derivative. The resolution of the surface elevation and grounding line data is 5 km. Curvatures from this data set showed good agreement with curvatures calculated from kinematic GPS along our radar transects at 1 km, 3 km, and 5 km spacings. The average flexural distance of the RIS is 3.2 km with a standard deviation of 2.6 km, thus our use of the 5 km topographic resolution is reasonable (Brunt and others, 2010a).

The thin beam model assumes that the ice shelf surface topography is reflective of the curvature at its neutral depth—where flexed ice transitions from extending to compressing. We see no drastic decreases in ice thickness throughout the radar data and proceed under the assumption that the depth to the neutral plane is constant near the grounding line and reflected by the ice surface topography. The curvature field calculated from the topographic data reveals areas of negative curvature (where surface is concave-down and would be extending rather than compressing) but these are on average smaller than the positive curvature values, and further, might instead result from ice surface vertical sinking produced by two adjacent basal crevasses (McGrath and others, 2012a, 2012b; Vaughan and others, 2012). These authors attribute surface cracks between basal crevasses to this type of surface flexure.

We assume that there is no vertical load on the beam (as our static formulation obviates the inclusion of transient vertical forces, such as tides), and, because the deflection due to buoyancy is small compared to the deflection in Sayag and Worster (2011) the internal shear stresses are correspondingly small. Additionally, the strain rates in this study region are small compared to other studies (e.g. Luckman and others, 2012; McGrath and others, 2012a), thus we do not include an in-plane stress in the formulation, which could accommodate for the extra viscous stresses seen elsewhere. In other regions where there is a large in-plane stress (i.e., areas of high strain rate) the compression in the upper half of the beam can be overcome, shifting the neutral plane higher, resulting in basal crevasses that penetrate to heights greater than half the thickness of the ice (as in

McGrath and others, 2012b). If the in-plane stress is high enough, the crack tip can propagate the full thickness of the ice, allowing the basal crevasse to develop into a rift.

2.2 Yielding criterion

There are two common formulations used to predict fracture propagation length in ice (for both surface and basal crevasses): the 'zero-stress' model and Linear Elastic Fracture Mechanics ('zero-stress'—Nye, 1955; LEFM—Van der Veen, 1998a, 1998b; Mottram and Benn, 2009). Both methods require knowledge of the local stress field. If the stress is assumed to result from viscous deformation, both models must assume two material flow-rate parameters which derive from viscous creep flow laws (Goldsby and Kohlstedt, 2001; Mottram and Benn, 2009). The 'zero-stress' model has been further modified to allow for tuning of a yield strain rate where crevasse depth or height data have been available (Vaughan, 1993; Mottram and Benn, 2009). Similarly, LEFM represents material yielding in the form of the critical stress intensity factor (Van der Veen, 1998a, 1998b). Where crevasses have been observed in equilibrium with the surrounding stress field, both yielding criteria have been applied with success. In other cases where crevasses are not obviously in equilibrium with the surrounding stress state (Mottram and Benn, 2009) or evidence exists indicating mixed-mode fracture (series 2 crevasses in Luckman and others, 2012) the 'zero-stress' model and LEFM tend to overestimate or underestimate crevasse depths respectively, sometimes by a factor of 2 to 3. Regarding the speed at which the fracture tip propagates, if cracks are assumed to form quickly—such that the mechanical energy needed to form new crevasse wall surfaces is not dissipated through viscous creep deformation—LEFM is a valid yield formulation. Assuming instead that crevasses form slowly, the 'zero-stress' model or sub-critical crack formulation (Weiss, 2004) may be more applicable (Schulson and Duval, 2009).

Based on our loading assumption and its computational simplicity, we instead propose that failure at the grounding line (regardless of the rate of failure) may be estimated as the depth to which the material can no longer support stress in tension. That is, brittle deformation occurs when stress exceeds a given yield strength. Thus when σ_{xx} is equal to a certain tension limit σ_T , we can solve for the thickness of the beam that exceeds the tensional yield strength. This would be the height to which a grounding line basal crevasse can propagate, given by:

$$h_c = \frac{h_i}{2} - \frac{\sigma_T}{\kappa\omega''} \qquad (3)$$

where h_i is the ice thickness and κ is as in Equation 2. A large literature of lab-derived yield strengths exists (Schulson and Duval, 2009: chapter 10 references). The yield strength for lab-prepared ice samples depends on many factors, including crystal size, preparation method, loading method, and ice temperature, but is generally 1 MPa. From -30°C to 0°C the tensional strength of ice is between 1.1 and 1.0 MPa (Schulson and Duval, 2009).

3. Results and Discussion

We applied TEB theory to grounding lines throughout Antarctica and, where possible, compared the model results to observations of basal crevasses.

3.1 Siple Coast

We observed 256 basal crevasse diffraction patterns in 19 separate radar transects covering 4 different regions in the Siple Coast: Siple Dome North (SN), Siple Dome South (SS), Kamb Ice Stream (KIS), and Whillans Ice Stream (WIS). We found an inverse relationship between crevasse height and ice thickness (Figure 3, black points), which can be explained using a TEB framework if the maximum bending stress for thicker ice is less than the maximum bending stress for thinner ice (Figure 4). This implies that the buoyancy-induced curvature for thicker ice is less than that for thinner ice.

Table 1 shows the mean and standard deviation of the difference between the observed and modeled values for different values of Young's modulus. No crevasses were predicted for the field-derived Young's modulus estimate of 1 GPa (Vaughan, 1995). The reason this value produces no estimates is not obviously apparent, but we suggest that it may better represent grounding lines characterized by higher strain rates or may reflect lack of certainty in ice thickness when the estimates were made, as the method used to estimate the Young's modulus is highly sensitive to ice thickness.

Figure 3 shows the TEB model produces results within the range in observation, with two noteworthy exceptions. Basal crevasse heights at SN are predicted to be 3 times higher than observed. Close examination of strain rates in this region (Figure 1A) reveals that our observed basal crevasses are in close proximity to the Bindschadler Ice Stream southern shear margin. Indeed, the ice velocity sea-ward of the grounding line is transverse to our radar lines in this area. We conclude that the observed misfit at SN is indicative of high shear stresses (i.e., viscous in-plane stress), and a more complex or mixed-mode fracture model needs to be considered where the grounding line is co-located with ice stream shear margins. Another location of misfit results at SS, for which our underestimated crevasses lie in a region complicated by changes in ice flow (Catania and others, (2006); Fig 1A). Indeed, Catania and others (2010) imaged a former grounding line upstream of its present location and it is possible that these basal crevasses formed long ago, when the direction and magnitude of grounding line flexure may have been different. Additionally, the geometry of the grounding line at this location is curved, and could indicate that the direction of flexure is more complicated than a 1-dimensional stress formulation allows. TEB theory predicts no basal crevasses for WIS, for which only a few, comparatively short (< 50 m in height) basal crevasses were observed. WIS has a well-noted ice plain and undergoes a more diffuse ungrounding than more classic grounding lines (Bindschadler, 1993; Walter and others, 2011; Winberry and others, 2009). So it is not surprising that the topography of WIS is not sufficiently curved to produce large (> 100 m) crevasse heights, as in the other areas.

3.2 Other areas

We perform the same analysis (Figure 5) on other grounding lines around Antarctica. The TEB model is most sensitive to curvature and predicts basal crevasses to exist at nearly all grounding lines. Our observations of 256 basal crevasses in the Siple Coast spanning 4 dynamically different grounding zones suggest that it may be reasonable for basal crevasses to exist without the associated topographic undulations typically used to infer their presence. It is also reasonable however that the assumptions which may be justified in the Siple Coast are not necessarily true elsewhere. Namely, our assumption that in-plane viscous stress is negligible is certainly not justified for all grounding lines around Antarctica, and this must be remembered when applying the TEB method elsewhere. Further, it is unlikely that any basal crevasses initiated through bending at the grounding line remain unmodified as they enter changing environments, either by melting / refreezing or by additional strain as the basal crevasses enter faster moving areas of the ice shelf. Basal crevasse heights could easily be modified by the time they reach the locations where other authors have observed them, and so we approach the analysis simply to explore the order of magnitude accuracy of the TEB method under the assumption that basal crevasses form in temporal sequence and are advected downstream to regions where others have observed them.

Several isolated examples of basal crevasses forming mid-shelf in the Larsen C Ice Shelf have been explored where bending cannot be invoked as an explanation (Luckman and others, 2012; Figures 2B and 5A,C,D). Here the propagation heights of basal crevasses were modeled using a viscous stress model and LEFM as a yielding criterion, with moderate success. Closer to grounding lines, Luckman and others (2012) and McGrath and others (2012a, 2012b) also observed long trains of basal crevasses approximately 100 m in height emerging near the shear margins of the Joerg and Churchill Peninsulas (Figure 5A). The TEB method estimates grounding line basal crevasse heights of approximately 100 to 150 m at the grounding line upstream and shear margin directly adjacent to these observations. Ice is shearing along these margins and so this may represent an over-estimate, just as in SN, where the grounding line curvature and strain rates were similarly high. In the Ronne-Filchner Ice Shelf, Rist and others (2002) observed basal crevasses far from the grounding line of Rutford Ice Stream (Figure 5B) of order 300 m in height. The TEB method estimates grounding line basal crevasses forming upstream of these observations approximately 400 m in height, and it may be that a combination of viscous deformation or basal melting can account for the misfit.

The TEB method also predicts basal crevasses to be present at the grounding lines of large pinning islands and ice rises such as Berkner Island and the Korff and Henry Ice Rises (Filchner-Ronne, Figure 5B) as well as Roosevelt Island and the Crary and Steershead Ice Rises (RIS, Figure 5D). Catania and others (2010; Figure 5A) imaged the eastern margin of Roosevelt Island and observed basal crevasses there between 100 – 130 m in height. The TEB prediction over-estimates this value by approximately 50 m (Figure 5D). We again attribute this over-estimation to high shear stresses, as in the case of SN, where these observations were made along a shear margin.

Most striking from the TEB crevasse maps is that regions of topographically undulated flow bands often follow directly downstream of areas in which the approximation predicts relatively high basal crevasse heights—strengthening the idea that basal crevasses can play a central role in determining the location of rifts and large-scale ice shelf damage. One such location appears on the Amery Ice Shelf (Figure 5C) stemming from the Charybdis Glacier: surface depressions appear close to the grounding line and—after rounding Single Promontory—develop into a long train of undulated topography that approaches the calving front. Additionally, the topographically undulated zones on the floating shelves of Pine Island (PIG) and Thwaites Glaciers (TG) appear directly downstream of locations where TEB-predicted basal crevasses appear to be comparatively large (Figure 5E).

While both PIG and TG are fast-flowing and have experienced recent dynamic changes—including high basal melt rates and grounding line retreat (e.g. Bindschdler and others, 2012; Vaughan and others, 2012)—a close inspection of the TG grounding line provides further motivation for the inclusion of basal crevasses in ice dynamic models. A Landsat-7 image from January 2013 (Figure 6) shows undulated topography which we believe may indicate the onset of basal crevasses. Measurements of the surface depression spacing (yellow bars) were compared to measurements of the freshly calved icebergs (red bars). The average spacing of the surface depressions is 1034 m and the average width of the freshly calved icebergs is 1035 m (standard deviations 217 and 224 m, respectively). This suggests that, at least in areas where basal crevasses persist long enough to reach the calving front, iceberg geometry can be controlled to a first order by the spacing of basal crevasses.

4. CONCLUSIONS

Our results show that the TEB formulation applied at or upstream of observed basal crevasses produces order-of-magnitude crevasse heights. The model is more accurate at grounding lines where strain rates are low and may best be used to infer where stresses are dominantly viscous if the misfit between observed and modeled basal crevasse height is large. Additionally, areas where the TEB method predicts comparatively high basal crevasses appear directly upstream of areas of topographically undulated and damaged ice. In light of their ability to determine ice berg geometry in some locations—notably Thwaites Glacier—we suggest it is important to incorporate the effects of basal crevasses when modeling calving processes.

ACKNOWLEDGEMENTS

This work was supported by US National Science Foundation grant ARC-0941678. We thank Joe MacGregor for assistance with satellite imagery. We also thank two anonymous reviewers and the scientific editor, Neil Glasser, who provided essential feedback and constructive criticism.

	5 GPa		7.5		10	
	N	*σ*	*N*	*σ*	*N*	*σ*
ALL	80	53	86	49	**77*	53
SS	101	46	**51*	25	62	47
KIS	**13*	10	102	44	73	43
SN	**66*	46	130	52	169	47

Table 1.1: Mean (N) and standard deviation (σ) of the absolute value of difference between observed and predicted crevasse heights for all four regions, tested against several vales of Young's modulus. No crevasses were predicted using E = 1 GPa (Vaughan, 1995). The value which minimizes the difference for all locations was 10 GPa; 5 GPa minimizes the difference for KIS and SN while 7.5 GPa minimizes the difference for SS. (*) denotes minimum for a particular group..

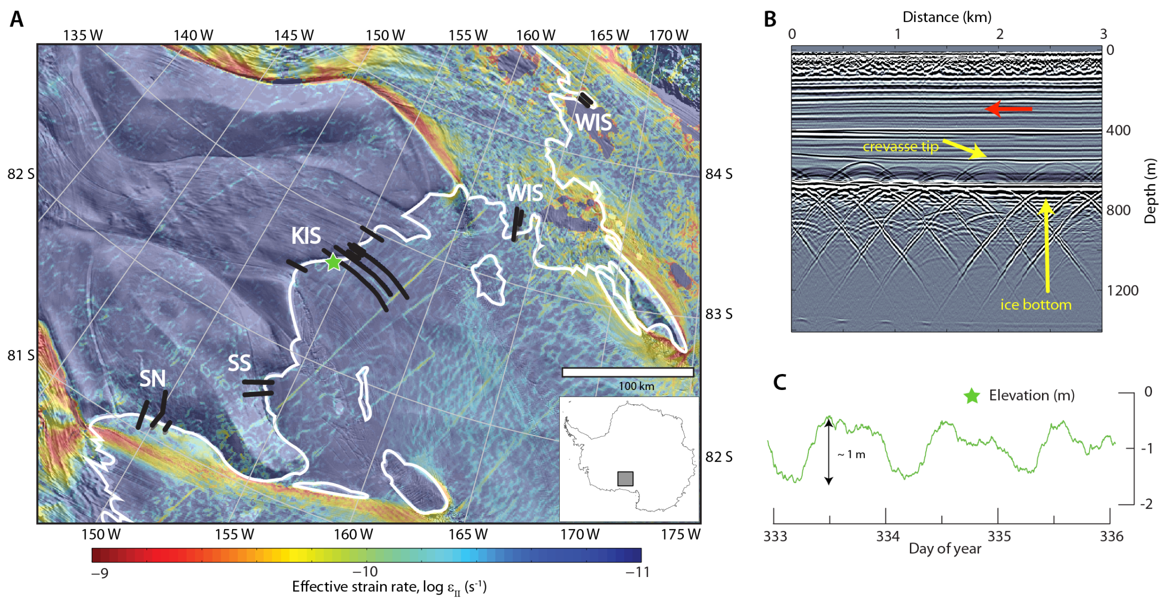

Figure 1.1: [A] Locations of radar profiles (thick black lines) in SN, SS, KIS, and WIS. Thin white line is the grounding line determined by Horgan and Anandakrishnan (2006). Kinematic GPS was recorded at the grounding line of KIS (green star). Background image is the MODIS Mosaic of Antarctica (MOA) (Haran and others, 2005) overlain by a color-scaled logarithmic plot of the computed effective strain rate in s^{-1} (Rignot and others, 2011) [B] Example of radar data showing typical hyperbolic diffraction patterns produced by basal crevasse crack tips and the ice-bottom interface (yellow arrows). Direction of ice velocity is shown by the red arrow. [C] Kinematic GPS taken at the location in panel [A] denoted by the green star. Tidal uplift is approximately 1 m.

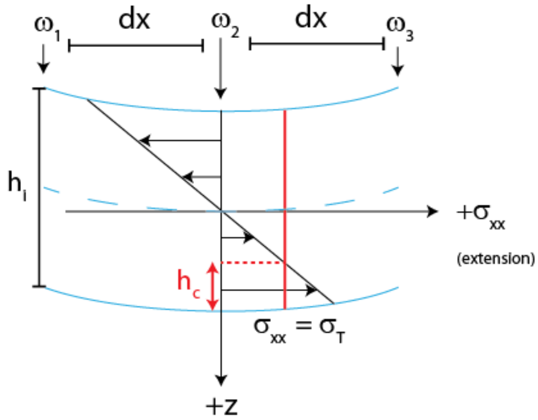

Figure 1.2: Schematic diagram of a characteristic thin beam. The applied bending moment compresses the upper half and extends the lower half of the beam. Extensive stress is positive, depth below the neutral plane (dashed blue line) is positive. The tensional yield strength (vertical red line) indicates where the beam can no longer support stress in tension (h_c, the basal crevasse height, red arrow). The stress profile depends on ice thickness (h_i) and curvature which is the second derivative of topography along the beam axis, in the x-direction (w''_x, green text), as well as Young's modulus and Poisson's ratio.

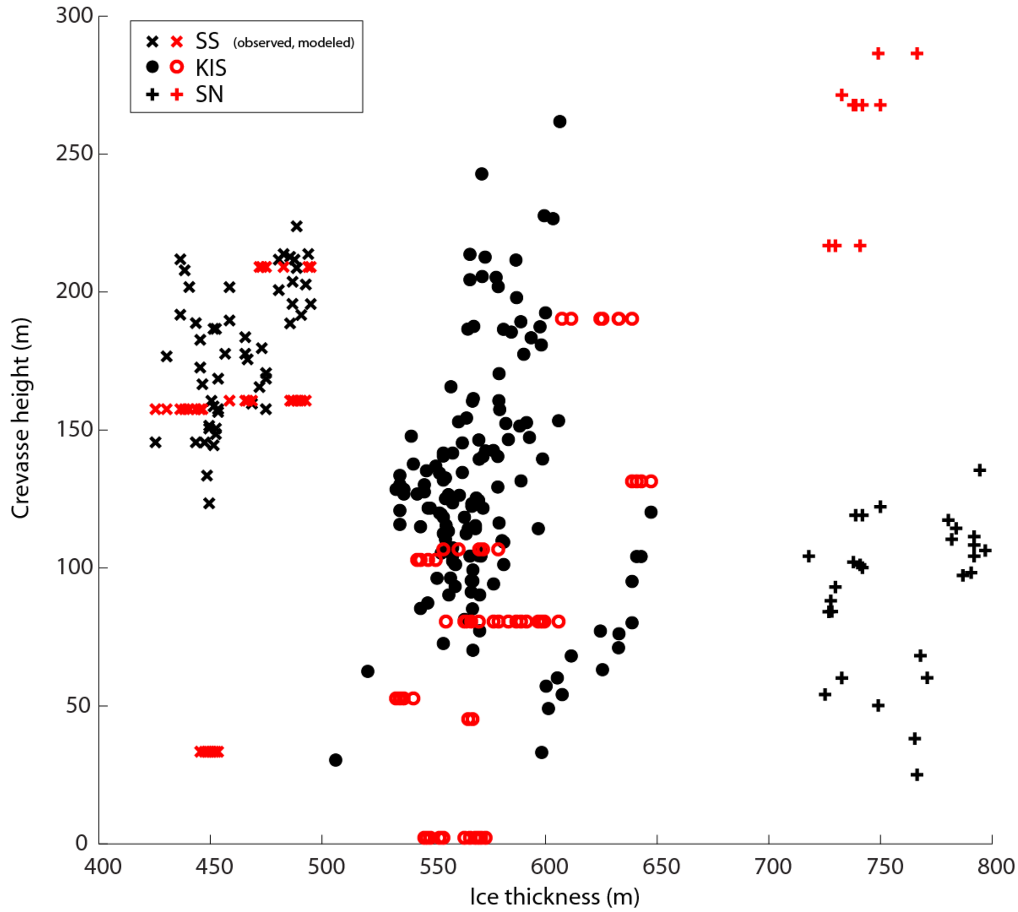

Figure 1.3: Predicted (red) vs. observed (black) basal crevasse heights. Most predictions are within the range of observation. Two areas of misfit can be attributed to high in-plane viscous stress (SN is collocated with Bindschadler Ice Stream shear margin) and previous grounding line location (SS). No crevasses are predicted for WIS, owing to its very low curvature as an ice plain.

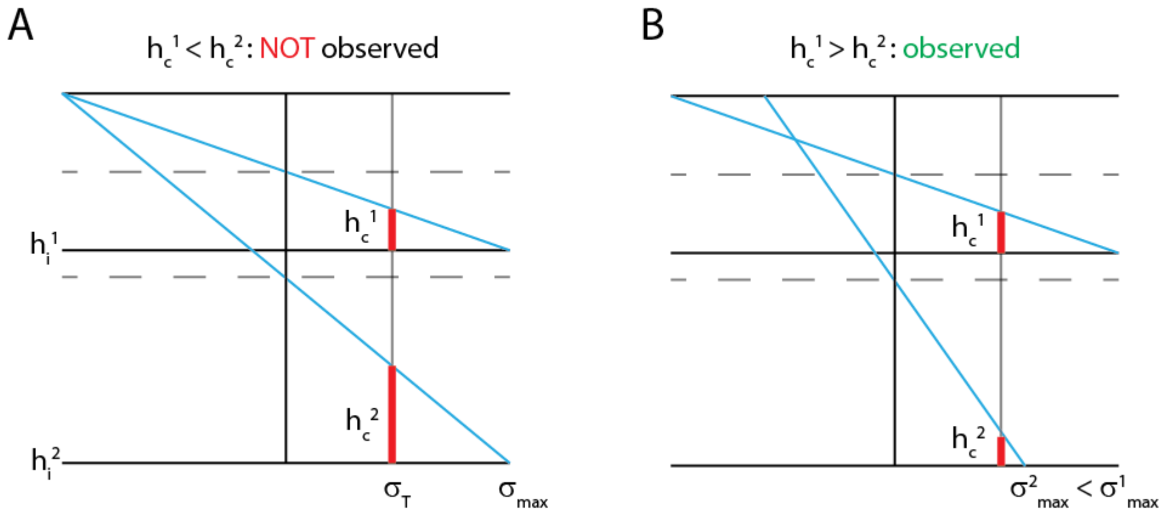

Figure 1.4: [A] Basal crevasses resulting from the same flexure applied to thinner (h_i^1) and thicker ice (h_i^2). Thicker ice produces bigger crevasses than thinner ice; this is not what we observe. [B] For smaller basal crevasses in thicker ice, it must be true that thicker ice experiences less induced bending stress (σ^2_{max}) than thinner ice ($\sigma^1_{max} > \sigma^2_{max}$).

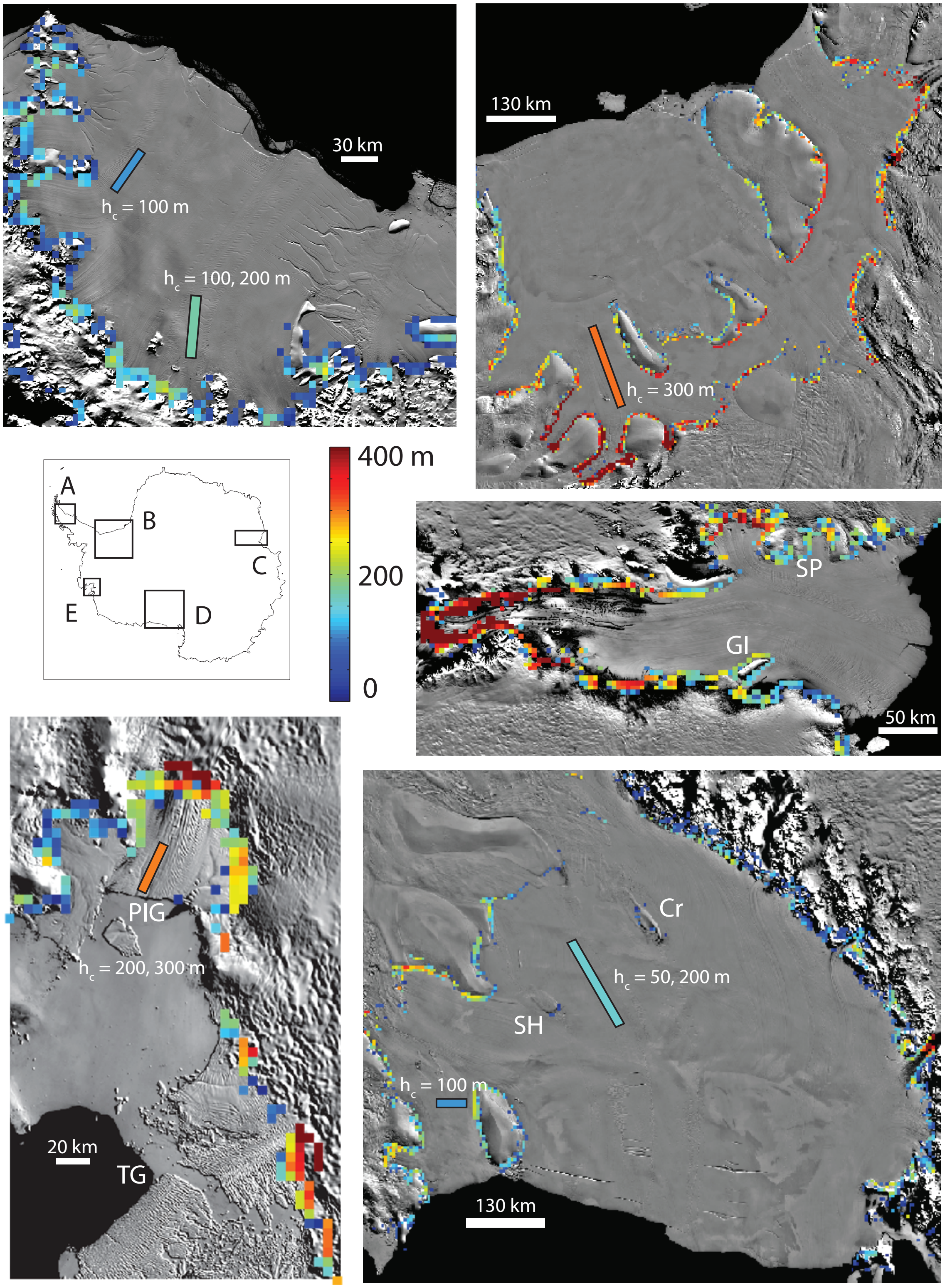

30 km
h_c = 100 m
h_c = 100, 200 m
130 km
h_c = 300 m
A
B
C
D
E
400 m
200
0
SP
GI
50 km
PIG
h_c = 200, 300 m
20 km
TG
Cr
h_c = 50, 200 m
SH
h_c = 100 m
130 km

Figure 1.5: Figure 5 MOA images overlain by the TEB-predicted basal crevasse heights, indicated by colorbar. Colored boxes with black outline are the approximate location and observed basal crevasse height from other radar studies. [A] Larsen C Ice Shelf compared with observations at Churchill (CP) and Joerg Peninsulas (JP) (McGrath and others, 2011; Luckman and others, 2011); [B] Ronne-Filchner Ice Shelf showing basal crevasses stemming from Rutford (Rut) Ice Stream, Kirchoff (KIR) and Henry (HIR) Ice Rises, and Berkner Island (BI) (Rist and others, 2002); [C] Amery Ice Shelf; undulated topography directly downstream of Charybdis Glacier (CG) and Single Promontory (SP); [D] Ross ice shelf (Jezek and Bentley, 1983); Roosevelt Island (RI, Catania and others, 2010); rifts develop directly downstream of Steershead (SH) and Crary (Cr) ice rises shown by basal crevasses; [E] Pine Island (Bindschadler and others, 2012) and Thwaites glaciers; central rift in Thwaites glacier develops directly downstream of high basal crevasses and shear margin. Large topographic undulations appear directly downstream from where high basal crevasses would be predicted in Pine Island glacier.

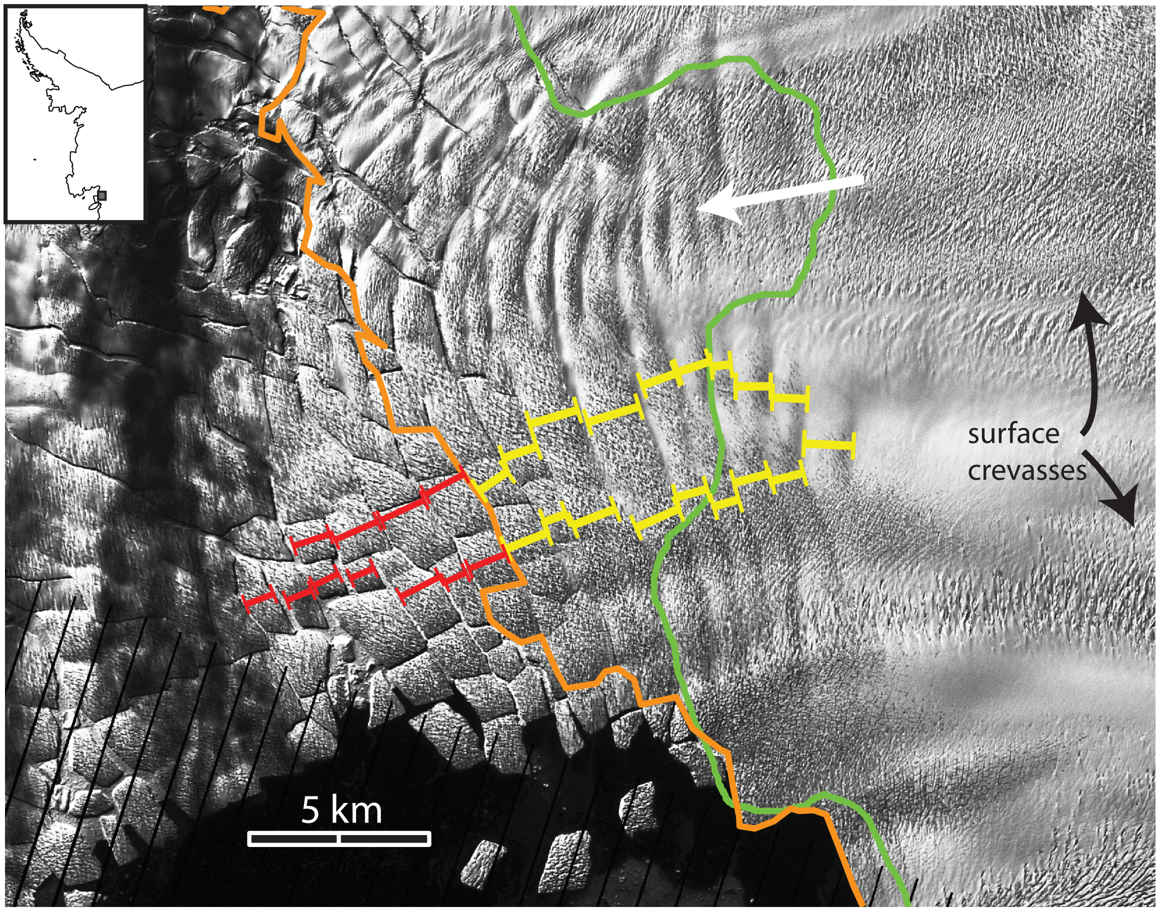

Figure 1.6: Landsat-7 ETM+ band 8 (15 m resolution) image of Thwaites Glacier (from January 2013) and MOA-derived grounding line (green line). Ice velocity is indicated by the thick white arrow. Surface crevasses appear as highly textured areas indicated by the black arrows. Spacing between topographic undulations (yellow bars) is compared to iceberg width (red bars). Ice still connected to TG is upstream of the calving front (orange line). Average distance between surface depressions is 1034 m; average width of icebergs is 1035 m (standard devations 217 and 224 m, respectively).

Chapter 2: DynEarthSol3D, a multi-rheology finite element method for modeling ice failure and dynamics

Liz Logan[1], Luc Lavier[1,2], Eunseo Choi[3], and Eh Tan[4]

[1] *Department of Geological Sciences, University of Texas at Austin*

[2] *Institute for Geophysics, University of Texas at Austin*

[3] *Center for Earthquake Research and Information, University of Memphis*

[4] *Institute of Earth Sciences, Academia Sinica, Taipei, Taiwan*

* Chapter 2 has been submitted as is to the Journal of Computational Geosciences

ABSTRACT

We present and explore a numerical model for the simulation of brittle failure for ice sheets. DynEarthSol3D (DES) is a multi-rheology finite element thermo-mechanical model. We perform the prognostic experiments designed for higher-order stress models as outlined in the ISMIP-HOM intercomparison project. While DES is executed with different boundary conditions and for different rheologies the model performs well compared with linearly-viscous Stokes models. DES is also executed for the simulation of a parallel-sided slab on an inclined plane going through a bend. This experiment is designed to show how DES might simulate a glacier advecting over the grounding line as it is subjected to hydrostatic floatation. We explore the effect that different ice thicknesses and different tilt angles have on the size and spacing of crevasses formed going through the bend. These experiments are done for several values in cohesion drop for the Mohr-Coulomb failure criteria, which are used in the following chapter to simulate more realistic grounding line scenarios, where ice melts and hydrostatic stress boundary conditions are applied.

1. INTRODUCTION

The ability to accurately predict sea-level change as a result of polar ice mass loss depends critically upon the ability of climate and ice sheet models to capture the physics of brittle fracture and non-linear viscous flow. In the past five years ice sheet models have largely risen to the challenge of simulating large scale steady state viscous flow, leading to the development of the latest class of ice sheet models that represent ice physics across many flow regimes and in three spatial dimensions. These are non-linear viscous thermo-mechanical models that solve the so-called full-Stokes (FS) equations (e.g., Gagliardini and Zwinger, 2008; Larour et al., 2012). Models based on shallow ice (SIA) and shallow shelf (SSA) approximations of the FS equations are also in wide use and simulate ice flow in most areas (Levermann et al., 2012; Lipscomb et al., 2013). Regardless of their computational cores, most models are designed largely for steady state flow, or diagnostic execution; to our knowledge only three models simulate prognostic, time-dependent ice flow (Martin et al., 2004; Gagliardini and Zwinger, 2008; Larour et al., 2012). Despite these computational advances many pertinent questions in glaciology remain that could potentially be addressed with a computational framework, particularly with regard to water flow within and under an ice sheet and mechanical failure of ice at ice sheet margins. However the inclusion of smaller scale physics to capture subglacial hydrology or ice fracture within an ice flow model often imposes too large a computational cost to remain a tractable problem. Thus both FS and SIA/SSA formulations employ parametrizations for the most complicated aspects of their systems, including: basal sliding, grounding line evolution, and the calving front – where ice mechanically fails.

Ice rheology has been studied using both geophysical observations and laboratory experiments (Budd & Jacka, 1989; Sammonds et al., 1998). Over short time scales ice behaves elastically before yielding and flowing viscously. Over long time scales ice behaves as a viscous fluid for which the viscosity is non-linearly dependent on both temperature and effective stress (Glen, 1957). The resulting law is called Glen's flow law and can be written as:

$$\dot{\varepsilon}_e = A\sigma_e^n \tag{1}$$

where A represents an Arrhenius temperature relation and $\dot{\varepsilon}_e$ is the effective strain rate (the square root of the second invariant of the strain rate tensor). Laboratory experiments also show that ice strain-rate hardens and that it starts to fracture in a brittle manner at high strain rate (Schulson and Duval, 2009). In nature, calving results from the fracture of ice and is a consequence of brittle or ductile fracture (van der Veen, 1998a; Weiss, 2004). Ductile fracture is initiated by the formation of distributed voids that eventually coalesce to form a fracture. Ductile fracture is a slow process for which weakening by voids occurs over a prolonged stress plateau. On the other hand, the breaking or damage process for brittle fractures occurs abruptly for a given value of stress.

Most numerical models simulate the long-term (years to thousands of years), large-scale behavior of ice sheets using a simple non-linear viscous formulation to calculate the stress tensor (e.g., Larour et al., 2012). Indeed for simulating long term flow of ice sheets this is an excellent approximation as the Maxwell viscoelastic stress relaxation timescale (time to dissipate elastic stresses) is on the order of a hours to days, depending on local material properties (MacAyeal & Sergienko, 2013). Because they ignore elastic stresses, the use of a viscous constitutive formulation in FS and SIA/SSA models may preclude their ability to self-consistently represent the elastic failure of ice and thus the retreat of ice due to calving. When calving is simulated, parameterizations depend empirically on strain rate fields derived from viscous stresses (Albrecht and Levermann, 2012; Levermann et al., 2012).

While it is true that the Maxwell viscoelastic relaxation time – the time it takes for the elastic component of stress to dissipate – is on the order of hours to days, the need remains in ice modeling to self-consistently simulate the growth and subsequently track features that result from brittle deformation. For example, calving via the detachment of large, tabular icebergs is an important end-member of observed calving styles (Amundsen and Truffer, 2010). The fractures that determine the size of tabular bergs—such as those in the Amery Ice Shelf 'loose tooth', and thus the calving rate in these locations – are exactly those features that result from brittle or ductile deformation over yearly to decadal time scales (Bassis et al., 2008). Thus while the elastic component of stress relaxes away over long-term simulations, the features which result from the elastic component of stress remain and affect the dynamics of ice (Glasser and Scambos, 2008). Here we present a Lagrangian numerical technique that allows for both elastic and viscous component of ice deformation to be taken in to account. We specifically explore how fractures form and propagate as a function of ice thickness, slab tilt, and Mohr-Coulomb failure properties in an advecting elastoplastic ice slab.

2. Model description

DES (DynEarthSol3D) is a robust, adaptive, three dimensional finite element model that solves the momentum balance and heat equation in Lagrangian form using unstructured meshes.

2.1 Equations of motion

While most FS models neglect acceleration and formulate ice flow as a static problem, momentum conservation in DES takes the full dynamic form:

$$\rho \dot{u} = \nabla \cdot \sigma + \rho g \tag{2}$$

where ρ is the material density, $\boldsymbol{u}$ is the velocity vector, $\boldsymbol{\sigma}$ is the Cauchy stress tensor, and $\boldsymbol{g}$ is the acceleration due to gravity. The dot above $\boldsymbol{u}$ is the total time derivative, and variables in boldface are vectors or tensors. The $\nabla \cdot$ is the divergence operator. The momentum equation is discretized using an unstructured grid based on triangles (2D) or tetrahedra (3D). The displacement $\boldsymbol{x}$, velocity $\boldsymbol{u}$, acceleration $\boldsymbol{a}$, force $\boldsymbol{f}$, and temperature T are defined on linear (P1) elements, while other physical quantities (e.g., stress $\boldsymbol{\sigma}$ and strain $\boldsymbol{\varepsilon}$) and material properties (e.g., density $\boldsymbol{\rho}$ and viscosity $\boldsymbol{\eta}$) are piecewise constant over elements. Conservation of mass is enforced via elasticity rather than the standard incompressibility condition. A general schematic of DES' solution scheme is shown in Figure 1.

The temperature field of the ice is modeled using the following heat equation:

$$\rho c_p \dot{T} + v \cdot \nabla T = k \nabla^2 T \tag{3}$$

where T is the temperature in Kelvin, c_p is the heat capacity of ice, and k is the thermal conductivity of ice. For the temperature field we impose Dirichlet boundary conditions on the ice surface and base, as well as at any water boundaries. While we are focused primarily on the failure of ice, the nonlinear dependence of viscosity on temperature necessitates that we track and solve for the temperature field within the ice, especially where the ice is in contact with warmer water.

Boundary value problems must be complemented with appropriated boundary conditions to ensure that they are well-posed, and we present more detailed descriptions of these in the Section 3 where our simple experiments are described. In DES we make use of both stress and velocity boundary conditions. In simulations where ice is frozen to its bed we prescribe that the basal velocity be zero, $\boldsymbol{u}_b = \boldsymbol{0}$. Ice at the surface is subject to a stress-free boundary condition, or $\boldsymbol{\sigma} \cdot \boldsymbol{n} = \boldsymbol{0}$. Floating ice is subject to a stress condition as well, where the applied stress is equal to the weight of the water column displaced by the ice. As yet, grounding lines are prescribed *a priori* and do not evolve according climate variables.

2.2 Numerical considerations

The most basic numerical difference between DES and other widely used ice models relates to the numerical formulation as explicit rather than implicit in time. The use of the explicit time method means that the time step is limited to very small values, on the order of $\Delta X_{min}/u_{elastic}$ where ΔX_{min} is the smallest length of an element facet and $u_{elastic}$ is the elastic wave speed (from the CFL condition). The advantage of using this method is that the cost of each time step is small (compared to implicit methods where advancing by one large time step involves the solving of large, ill-conditioned linear systems) and the implementation of non-linear rheologies is simple.

Because we have multiple rheologies and evaluate stresses due to different constitutive laws, we determine the appropriate time step based on the dominating deformational mechanism. The time step is chosen as the minimum between

$$\Delta t = \min\{ \Delta t_{elastic} , \Delta t_{maxwell} \} \tag{4}$$

where

$$\Delta t_{elastic} = \Delta X_{min}/2c\, u_{char} \tag{5.a}$$

$$\Delta t_{maxwell} = \eta_{min}/4G \tag{5.b}$$

and ΔX_{min} is the mimimum element facet length in the mesh, c is the inertial scaling parameter related to the dynamic relaxation, u_{char} is the characteristic advective speed, η_{min} is the minimum allowable viscosity, and G is the shear modulus. This scheme ensures that the dominating deformational mechanism is adequately resolved in time. As such the time steps in DES are on the order of seconds to hours, depending largely on mesh parameters and the characteristic speed of the simulation as determined by the phenomenon the user wishes to resolve.

In addition to the dynamic time-stepping routine, several other numerical techniques are employed that distinguish this model from implicit finite element schemes commonly used to solve FS systems. DES solves the time-dependent momentum balance equation by damping the inertial forces at each time step, giving rise to the quasi-static solution. Originally proposed by Cundal [1989], this variant of dynamic relaxation applies forces at each node in the domain opposing the direction of the node's velocity vector:

$$ma_i = (f_{damped})_i = f_i - \chi\, sgn\, (u_i)|f_i| \tag{6}$$

where the subscript i denotes the i-th component of a vector and the sgn(*) denotes the signum function. χ is a user-supplied damping factor (χ = 0.8 has been shown to ensure stability, Choi et al., 2013).

The linear triangular elements used in DES are known to suffer volumetric locking when subject to incompressible deformations (e.g., Hughes, 2000). Because we model phenomena that require imcompressible plastic and viscous flow, we use and anti-volumetric-locking correction based on the nodal mixed discretization methodology (Detournay and Dzik, 2006; De Micheli and Mocellin, 2009). The technique simply averages the volumetric strain rate over a group of neighboring elements and then replaces each element's volumetric strain rate with the averaged one. Choi et al. [2013] describes this technique in greater detail.

Finally, DES makes use of adaptive remeshing. Based on the quality constraints selected by the user, DES assesses the mesh quality at fixed step intervals and remeshes if elements are found in violation (e.g., if a triangular element contains an angle smaller than some input threshold). New nodes may be inserted into the mesh or the mesh topology changed through edge flipping. The nodes are provided to the *Triangle* library (Shewchuk, 1996) to construct a new triangulation of the domain. After the new mesh is created the boundary conditions, derivatives of shape functions, and mass matric are recalculated. When deformation is distributed over a large region or the whole domain, remeshing may result in a new mesh quite different from the old one. Because of this possibility the fields associated with nodes (e.g., velocity and temperature) are linearly interpolated from the old mesh to the new. For data associated with elements (e.g., strain and stress) DES uses a conservative mapping described in detail by Choi et al. [2013].

2.3 Constitutive relation

In DES the updated stress tensor in the momentum equation is calculated using the strain rate and strain tensors. These are determined by the constitutive relation. For the Maxwell viscoelastic (VE) rheology, viscosity is determined by Glen's flow law:

$$\eta = \frac{1}{2} A^{-1/n} \dot{\varepsilon}_e^{(1-n)/n} \tag{7}$$

The stress update is given by:

$$dev(\sigma^{t+\Delta t}) = 2\eta \, dev\,(\dot{\varepsilon}^t) + K\, tr(\varepsilon) \tag{8}$$

where dev(*) and tr(*) indicate the deviatoric component and trace of the quantity in the parentheses, and K is the bulk modulus. For the Maxwell VE case the constitutive update is given by the total deviatoric strain increment which is composed of a viscous and elastic contribution corresponding to the mechanical analog of a spring and dashpot in series:

$$dev(\Delta\varepsilon) = \frac{dev(\Delta\sigma_{VE})}{2G} + \frac{dev(\sigma_{VE})\,\Delta t}{2\eta}\,. \tag{9}$$

Substituting $\Delta\varepsilon$ with $\varepsilon^{t+\Delta t} - \varepsilon^t$, $\Delta\sigma_{VE}$ with $\sigma_{VE}^{t+\Delta t} - \sigma^t$, and σ_{VE} with $\left(\sigma_{VE}^{t+\Delta t} + \sigma^t\right)/2$, the equation above is reduced to:

$$\sigma_{ve}^{t+\Delta t} = dev(\sigma_{ve}^{t+\Delta t}) + \Delta t\, K\, tr(\dot{\varepsilon}^{t+\Delta t})\, I\,. \tag{10}$$

The elastoplastic (EP) stress σ_{EP} is computed using linear elasticity and the Mohr-Coulomb (MC) failure criterion with a general (associative or non-associative) flow rule. Following a standard operator-splitting scheme (e.g., Lubliner, 1990; Simo and Hughes, 2004; Wilkins, 1964), and elastic trial stress $\sigma_{et}^{t+\Delta t}$ is first calculated as:

$$\sigma_{et}^{t+\Delta t} = \sigma^t + \left(K - \tfrac{2}{3}G\right) tr(\dot{\varepsilon}^{t+\Delta t}) I\Delta t + 2G\dot{\varepsilon}^{t+\Delta t}\Delta t. \tag{11}$$

If the elastic trial stress is on or within a yield surface, that is, $f\left(\sigma_{et}^{t+\Delta t}\right) \geq 0$, where *f* is the yield function, then the stress does not need a plastic correction. In this case $\sigma_{ep}^{t+\Delta t}$ is set equal to $\sigma_{et}^{t+\Delta t}$. If $\sigma_{et}^{t+\Delta t}$ is outside the yield surface, then it is projected onto the yield surface using a return-mapping algorithm, (e.g., Simo and Hughes, 2004).

In the case of a Mohr-Coulomb material, it is convenient to express the yield function for the tensile failure as

$$f_t(\sigma_3) = \sigma_3 - \sigma_t \tag{12}$$

where σ_1 and σ_3 are the maximal and minimal principal stresses with the convention that tension is positive, and σ_t is the yield stress in tension. For shear failure the corresponding stress envelope is defined as

$$f_s(\sigma_{1,}\sigma_3) = \sigma_1 - N_\phi\sigma_3 + 2C\sqrt{N_\phi} \tag{13}$$

where *C* is the material's cohesion, ϕ is the internal friction angle, and $N_\phi = \frac{1+\sin\phi}{1-\sin\phi}$. To guarantee a unique decision on the mode of yielding (tensile versus shear), we define an additional function that bisects the obtuse angle made by two yield function on the $\sigma_1 - \sigma_3$ plane, as

$$f_h(\sigma_{1,}\sigma_3) = \sigma_3 - \sigma_t + \left(\sqrt{{N_\phi}^2 + 1} + N_\phi\right)\left(\sigma_1 - N_\phi\sigma_t + 2C\sqrt{N_\phi}\right). \tag{14}$$

Once yielding occurs, that is $f_s < 0$ or $f_t > 0$, the mode of failure is decided based on the value of f_h. Shear failure occurs if $f_h < 0$ and tensile otherwise.

The flow rule for frictional materials is in general non-associative, meaning the direction of plastic flow in the principal stress space is not the same as the direction of the vector normal to the yield surface. The plastic flow potential for tensile failure can be defined as

$$g_t(\sigma_3) = \sigma_3 - \sigma_t \tag{15}$$

while the plastic flow potential for shear is

$$g_s(\sigma_1, \sigma_3) = \sigma_1 - \frac{1+\sin\psi}{1-\sin\psi}\sigma_3 \ . \tag{16}$$

When there is plastic failure, the total strain increment is given by

$$\Delta\varepsilon = \Delta\varepsilon_{el} + \Delta\varepsilon_{pl} \tag{17}$$

where $\Delta\boldsymbol{\varepsilon}_{el}$ and $\Delta\boldsymbol{\varepsilon}_{pl}$ are the elastic and plastic strain increments. The plastic strain increment is normal to the flow potential surface and can be written as

$$\Delta\varepsilon_{pl} = \beta\frac{\delta g}{\delta\sigma} \tag{18}$$

where β is the plastic flow magnitude. β is computed by requiring that the updated stress state lies on the yield surface,

$$f\left(\sigma_{ep}^{t+\Delta t}\right) = f\left(\sigma^t + \Delta\sigma_{ep}\right) = 0. \tag{19}$$

In the principal component representation, $\sigma_A = E_{AB}\epsilon_B$ where σ_A and ϵ_A are the principal stress and strain, respectively, and E is a corresponding elastic moduli matrix with the following components:

$$E_{AB} = \left(K_S - \frac{2}{3}G\right) \text{ if } A \neq B \text{ and} \tag{20.a}$$

$$E_{AB} = \left(K_S + \frac{4}{3}G\right) \text{ otherwise.} \tag{20.b}$$

By applying the consistency condition and using $\sigma_{et}^{t+\Delta t} = \sigma^t + E \cdot \Delta\epsilon$, we obtain the following formula for β,

$$\beta = \frac{\sigma_{el,3}^{t+\Delta t} - \sigma_t}{\frac{\delta g_t}{\delta\sigma_3}} \text{ for tensile failure and} \tag{21.a}$$

$$\beta = \frac{\sigma_{el,l}^{t+\Delta t} - N_\phi\sigma_{el,3}^{t+\Delta t} + 2C\sqrt{N_\phi}}{\sum_B\left(E_{1B}\frac{\delta g_s}{\delta\sigma_B} - N_\phi E_{3B}\frac{\delta g_t}{\delta\sigma_B}\right)} \text{ for shear failure.} \tag{21.b}$$

Likewise, $\delta g/\delta\sigma$ takes different forms according to the failure mode:

$$\delta g/\delta\sigma_1 = 0 \tag{22.a}$$

$$\delta g/\delta\sigma_2 = 0 \tag{22.b}$$

$$\delta g/\delta\sigma_3 = 1 \text{ for tensile failure and} \quad (22.c)$$

$$\delta g/\delta\sigma_1 = 1 \tag{23.a}$$

$$\delta g/\delta\sigma_2 = 0 \tag{23.b}$$

$$\delta g/\delta\sigma_3 = \frac{1+\sin\psi}{1-\sin\psi} \text{ for shear failure.} \quad (23.c)$$

Once $\Delta\varepsilon_{pl}$ is computed, σ_{ep} is updated as

$$\sigma_{ep} = \sigma_{et}^{t+\Delta t} - E \cdot \Delta\varepsilon_{pl} \tag{24}$$

in the principal component representation and transformed back to the original coordinate system. After the viscoelastic stress and elastoplastic stress are evaluated, we compute the second invariant of the deviatoric components of each, and following the minimum energy principle, select the smaller of the two as that element's stress update.

3. EXPERIMENTS AND RESULTS

In Choi et al. [2013], DES performed the benchmark tests for Maxwell VE, Mohr-Coulomb EP, and VEP rheologies to validate and verify the numerical method. These tests included: 1 – flexure of a finite-length elastic plate; 2 – thermal diffusion of a half-space cooling plate; 3 – stress build-up in a Maxwell viscoelastic material; 4 – Rayleigh - Taylor instability; and 5 – Mohr-Coulomb oedometer test. Thus DES has been verified and validated and is already in use in fields relating to crustal deformation. However for the purposes of comparison and to test DES' appropriateness for cryospheric uses we executed several experiments designed to highlight both the model's flexibility and promise as a tool that might be useful for exploring processes related to ice failure in dynamic regions.

3.1 Comparison of non steady-state full Stokes solver and EP, VE and VEP non steady state cases.

Great effort has been put forward in comparing and benchmarking different approximations of Stokes flow in Lagrangian and Eulerian frameworks, which employ mostly steady state solvers (Pattyn et al., 2008). Pattyn et al. [2008] published the results of the first ice sheet model inter-comparison project for higher-order stress models (ISMIP-HOM) wherein 28 Stokes flow models of varying complexity performed the same five 'benchmark' experiments to evaluate "the conditions under which different higher-order solutions are viable and to determine whether numerical issues affect the result."

All experiments were designed to be isothermal with constant viscosity, and only one out of the five experiments was time-dependent. While DES is a very unique Lagrangian explicit solver that is not limited to non-Newtonian steady-state Stokes flow, it is still possible to gain insights in the physics of ice sheet flow by comparing a non-Stokes solver like DES that includes the effect of elastic stress and plastic deformation to the very few non-steady-state Stokes solvers presented in Pattyn et al. [2008]. In order to get a first-order comparison between those non steady state models that participated in the experiment and DES, we executed DES according to the time-dependent, prognostic experiment. As DES is not formulated for steady state problems we felt this to be the best fit in terms of experimental setup. We therefore compare the state of stress and deformation for the cases of an elastoplastic (EP), Maxwell viscoelastic (VE) and visco-elasto-plastic (VEP) slab of ice (Figure 2 and 3) to each other and to the non steady state Stokes solver to see if any fundamental characteristics of ice sheets physics can be described by such simple experiments. For completion we also compare the surface deflection of the 3 previous cases to the non steady state cases (Figure 2.3) described in Pattyn et al. [2008].

The non steady state experiment (F) from Pattyn et al. [2008] entails the time-dependent simulation of a parallel-sided slab running over a Gaussian bump inclined at 3°. The viscosity is constant and set to 7.3669 x 10^{13} Pa s. The ice thickness is H = 1000 m and domain size is taken to be L = 100H, with a Gaussian bump of amplitude 100 m and width 10,000 m located at the center of the domain. For computational reasons we scaled all geometric elements of this domain down to the width 10 km (instead of 100 km), and set a resolution of 50 m (Figure 2). Because DES' mesh refines dynamically and each node is free to move, we cannot prescribe the same periodic boundary conditions described in Pattyn et al. [2008]. Instead, we simulate the freely-slipping case and prescribe velocity of 200 m yr^{-1} as boundary conditions on the left, bottom, and right-hand side of the domain, with the surface remaining stress free (Figure 2). As a consequence of these boundary conditions there is no geometric steady state for this experiment to relax to, and so we simply run the slab over the bump until the deformation pattern is steady state. The temperature in the model is constant and set to 0° C. Because the boundary conditions play such an important role in the deformation of this experiment, we also executed the same setup on a flat slab, to see what – if any – impact DES' velocity boundary conditions have on the final result (Figure 3 – bottom panels).

3.1.1 Benchmark problem, tilted and flat

Figures 2A and 2B show the effective stress and strain within the ice for the three different constitutive laws employed by DES at 4 months real time for the model runs. For the EP case we use weakening of cohesion as a function of plastic strain (from 6 x 10^5 Pa → 1 x 10^5 Pa over .001 of plastic strain) to simulate damage in the ice as fractures propagate. The state of stress in the EP case is an order of magnitude higher (~10^6 Pa) than the VE or VEP case (~10^5 Pa), especially in the lower part of the ice sheet. In the EP case the stresses decrease from top to bottom and are affected by the localization of deformation in tensional and shear fractures around the bump. The state of stress also shows some structure near the boundary where the ice slab is sliding up and down under gravity. For the VE and VEP cases the stresses are highest around the bump and lowest near the surface of the ice slab. They reach a maximum of about 2 x 10^5 Pa at the bottom of the ice slab for VE and a maximum of 4 x 10^5 Pa at the bottom of the ice slab for the VEP case. The effective strain (square root of the second invariant of the strain tensor) shows localized deformation in the EP case that is mostly due to the accumulation of plastic strain either in shear or tension. However a large amount of strain accumulates at the bottom of the ice slab around the Gaussian asperities for the VE and VEP cases, with a maximum on the downstream side of the bump (Figure 2).

Figure 3 displays the comparison of the surface deflection and velocity obtained from DES after 4 months of motion over the bump for the EP, VE and VEP cases. In both the titled and flat scenarios the EP rheology is very different from the VE and VEP rheologies. The VE and VEP rheologies are very similar in both deflection and velocity while the EP cases behave as rigid slab sliding over a bump. The VE and VEP cases not only slide over the bump but also flow internally from left to right. The resulting surface velocity is about 40 m yr^{-1} higher in the viscous cases than in the elastic cases. When the ground is flat the difference in deflection and velocity is less pronounced and is closer to the benchmark results.

The tilted versus flat (top versus bottom) cases shown in Figure 3 indicate that the use of non-periodic boundary conditions in these experiments affects the deformation of the ice greatly. Both the VE and VEP cases show a large amount of deformation due to gravity which is reflected in their surface deflection slope (Figure 3A). This demonstrates that VE or VEP ice is very weak compared to the much stiffer EP ice rheology, which matches very closely to the ISMIP-HOM FS simulations. The bottom panels of Figure 3 show that all rheologies in DES match the FS linearly-viscous models well when the effect of the boundary conditions is removed. That is, the mismatch between DES and the FS models from the ISMIP-HOM experiment is due largely to the interaction between gravity acting on a fluid and boundary conditions that serve to hold the ice back rather than letting it flow out of the domain, as periodic boundary conditions would.

We conclude that when DES is compared to the other models in the ISMIP-HOM prognostic experiment, the model performs remarkably well when the effect of non-periodic boundary conditions is removed. The large discrepancy between the ISMIP-HOM model participants and DES for the case when DES is executed on the inclined plane indicates that DES is not recommended for the simulation of ice in scenarios that require periodic boundary conditions, or in situations where the goal is to see steady-state behavior.

The larger stress magnitude of the EP case (~10^6 Pa) compared to the VE and VEP (~10^5 Pa) cases (Figure 2) can be explained by the persistence of the elastic strength of the ice slab that diffuses over a short time scale for the VE case. Experimental evidence shows that for the range of stresses and strain rates observed in ice sheets the viscosity varies between 10^{11} Pa s and 10^{15} Pa s (MacAyeal and Sergienko, 2013), which for a Young Modulus of 9 GPa represents an elastic stress relaxation time scale in the VE and VEP cases of ~ 5.5 s to 15 hours. These time scales are well below the range of relevant deformation time scales in the experiments (months to years) and show that the elastic component of stress cannot persist over the time scales simulated in the VE and VEP cases. Moreover the stress magnitude resulting from the flow of ice (~2 – 4 x10^5 Pa) is below the laboratory-measured tensile strength of ice of 10^6 Pa. This result implies that ice must fracture at high strain rates. This is consistent with observations in lab experiments that show that a ductile to brittle transition in ice occurs when strain rates are higher that 10^{-8} - 10^{-7} s^{-1} (Schulson and Duval, 2009). Therefore stiffening of ice at high strain rate will be accompanied by fracture only at correspondingly high tensile stress ($>10^6$ Pa). The strain rate dependent nature of the transition from ductile to brittle implies that – depending on the viscosity – fracture in ice occurs on time scales of less than a few seconds to hours. This transition is dynamic and occurs only when rate of deformation and the tensile stress in ice are sufficiently high. The ductile-brittle transition in ice sheets is therefore fundamentally different from that of the Earth's lithosphere, which can maintain elastic stresses over millions of years (Choi et al., 2013).

Since we showed above that the use of VE or VEP rheologies (in DES) for the study of flow and fracture is contingent on the implementation of a dynamic ductile-brittle transition, we propose to use the EP rheology that has a steady state elastic state of stress to study how fractures propagate when an ice slab undergoes deformation for tensile stresses above the tensile strength of ice. For completion we compare the results of the EP case to that of the VEP case.

3.2 Tilted, bending slabs

Observations have shown that the bending that occurs as ice transitions from resting on land to floating in water promotes the failure of ice from the bottom up, called basal crevasses. These features appear with characteristic regularity in spacing, often persisting within the ice for long distances and promoting the eventual calving of ice (Bindschadler et al., 2011; Logan et al., 2013; McGrath et al., 2012a,b; Murray et al., 2014; James et al., 2014). In order to simulate an idealized version of this scenario, we test the effect that a forced bend has on a parallel-sided slab. Further, because bending or flexural stresses are determined largely by ice thickness and ice curvature (Logan et al., 2013), we performed a suite of sensitivity tests over a range of ice thicknesses and tilt angles for a range of ice weakening parameters and for both the EP and VEP rheologies. Figure 4 shows the effect that the EP and VEP rheologies have on the failure patterns of a 10 km long, 500 m thick slab advecting down an inclined plane tilted at 3° with a bend imposed at 10 km within the domain. We maintain the same velocities on the left, bottom, and right-hand sides of the domain set to 300 m yr^{-1}, and the ice is forced flat at the 10 km location within the domain (Figure 4). For the VEP case, the ice takes the full range of nonlinear viscosity, and the temperature of the ice varies linearly with depth, from the surface at -30°C to the base at 0°C.

Figure 4 shows the effective stress, plastic strain, and viscosity after twenty five years real model run time for the two rheologies. The effective stresses for the EP and VEP cases (Figure 4A) are different by 1 to 2 orders of magnitude. For the EP case the stresses are highest (about 1 MPa) on the basal surface and in a thin vertical line at the bend, whereas the VEP case shows only a slight increase in stress at the bend and nowhere else. The associated plastic strains – corresponding to the amount an element has strained once it has reached the yield stress – reflects this pattern: while the EP rheology has a localized and very high stress at the bend, promoting failure almost through the entire ice thickness, the correspondingly low stresses in the VEP show virtually no failure anywhere in the ice. One indicator as to why this might be can be seen in Figure 4C, where the effective viscosity, determined in the VEP case by Glen's flow law, shows that overall the ice is much stronger and stiffer for the EP rheology, while the VEP rheology shows very weak ice in the basal layer, the upstream side of the slope, and for approximately 5 km after the bend. The wideness of this weak zone immediately surrounding the bend contrasts with the EP rheology, where only a thin vertical section of ice is weak (~ 10^{13} Pa s) only at the ice bend, while the ice viscosity on the slope is an order of magnitude higher and the ice that has advected past the bend is almost 3 orders of magnitude higher. Thus the effective strains (Figure 4D) associated with the deformation are very localized for the EP rheology (limited to about 1 or 2 elements in width making for a very small process zone) and very diffuse for the VEP case, which shows a large process zone of basal strain before and after the bend in the ice. Because the VEP ice is comparatively so weak (Figure 4C) the ice topography reflects the effect of gravity much more: the left-hand side of the domain shows a steep depression at the ice surface, where the ice is essentially slumping toward the right-hand side of the domain, downhill.

3.2.1 Mohr-Coulomb properties of ice and associated failure patterns

We tested a range of values for cohesion on the Mohr-Coulomb failure envelope (Table 1) and set an angle of internal friction $\phi = 30°$ (Schulson, 2006). Table 2 shows all the relevant parameters used in the model that were not part of the parameter sensitivity test. Figure 4 shows outputs for the cohesion drop of $6x10^5$ to $3x10^5$ Pa over .001 accumulated plastic strain. The plastic strain for the EP rheology shows a very regular, localized mode of failure that is similar to an idealized version of a field of basal crevasses (Figure 4B). During model simulation the strain begins at the base of the slab at the bending fulcrum (similar to the grounding line of a glacier) and quickly propagates upward toward the surface. Over the total span of the model run time the ice slab that advects through the bend accumulates strain, but the simulation is dominated by the VE stresses and so localization features typified by purely brittle failure do not appear in the VEP case.

For each different experiment we simulated 3 different levels of plastic weakening by varying the magnitude of cohesion drop with the accumulated plastic strain, shown in column 4 of Table 1. The regularly spaced pattern of brittle failure only appeared for the EP rheology, and parameter sensitivity tests performed for the VEP rheology resulted in no change in the diffuse distribution pattern of failure. Figure 5A shows a sweep of results for variation in bending angle and a cohesion drop of $6\times10^5 \rightarrow 1\times10^5$ Pa over .001 accumulated plastic strain. Higher bending angles (> 5 degrees) led to more closely spaced basal crevasses as well as higher levels of accumulated plastic strain, > .05. Figure 5B shows the results for all three plastic weakening experiments for a tilt angle of 3° and a thickness of 500 m. Higher levels of plastic weakening produced marginally more damage but did not change the pattern or location of failure. Figure 6 shows the results for the pattern of brittle failure with varying ice thicknesses for a cohesion drop of $6\times10^5 \rightarrow 1\times10^5$ Pa over .001 accumulated plastic strain. Thicker ice produced more widely spaced basal crevasses. We measured the spacing of basal crevasses formed for both parameter sensitivity tests and plotted the results in Figure 7. Basal crevasses were counted as zones where plastic failure occurred in at least the bottom 3 elements (of resolution 50 m each) with corresponding plastic failure directly above in at least 3 elements. Both suites of parameter tests in ice thickness and tilt angle show that, to a first degree, basal crevasse spacing correlates positively with ice thickness and negatively with tilt angle.

4. Discussion

The experiments performed in this study are not meant to be exhaustive and wide-reaching; rather, they were performed to show the capabilities of DES and to report how the material deforms and fails given all the components of the model.

The experiments performed in Section 3.1 showed that DES largely captures the flow of ice irrespective of the chosen rheology. However, given that the mesh is not static it may not be advisable to simulate scenarios where periodic (wrap-around) boundary conditions are crucial. Figure 2 showing the surface deflection and surface velocity for the tilted experiments makes clear how important the boundary conditions are on impacting the location and magnitude of the bumps for the VE and VEP rheologies. The EP rheology on the other hand has a much higher effective viscosity, and as a consequence the material retains its stiffness throughout the simulation and does not 'slump' downward due to gravity. The similarity between the VE and VEP cases indicates that the Maxwell VE stress is almost always less than the Mohr-Coulomb EP stress. Thus the use of the minimum energy principle means that simulations largely express more ductile rather than brittle behavior. One of DES' advantages is that it can simulate time-dependent failure and, correspondingly, using DES to understand failure patterns in ice may prove challenging with the VEP constitutive law where the minimum energy principle decides the mode of deformation (ductile versus brittle).

Figure 4 shows the impact that the choice of constitutive law makes on the failure patterns at areas of bending (e.g., grounding lines). The plastic strain field shows a very regular spacing for EP rheology while the VEP rheology shows a diffuse zone. Because we do not actually simulate fractures – ice in DES is represented as a continuum material – we must assume that at some level of strain the ice in a simulation is considered broken. Zones of intense, vertical localization in the bending experiments we can consider to have ruptured and further, in essence, represent basal crevasses. These 'crevasses' form where the bending shear and extensional stresses are highest and are then advected away from the grounding line. In this light then the parameter test for 'crevasse' spacing versus ice thickness or tilt angle might imply a very simple calving law: Figure 7 shows from the EP simulations that the spacing of ‘crevasses’ is roughly half the local ice thickness, and for more highly tilted location we can expect that calving occurs in a more frequent serac-style manner. While this is an extremely over-simplified simulation of a glacier (2D, no tidal forcing, no melting, velocity boundary conditions instead of stress) the results here suggest that more work with DES could yield more robust conclusions if indeed any kind of calving law were to be inferred from numerical simulations of ice failure.

Finally, if it were true that a brittle-ductile-transition-zone based on the local strain-rate could be appropriately formulated into a type of VEP ice rheology (as in Schulson & Duval, 2009), our results in Figures 5 and 6 might imply a more realistic picture surrounding the formation of basal crevasses: the high strain-rates of both the VE and EP rheologies at these bending locations would limit the localization to a smaller process zone, and the outputs thus of the VEP rheology based on a brittle-ductile transition zone could be much more consistent with those of a purely EP rheology.

From very simple model runs we learned that contrary to lithospheric models of deformation, in ice, there is a dynamic ductile-brittle transition in ice that is likely very difficult to capture in numerical models. Therefore in this paper we limit our study to the EP case and explored how tensional and shear fractures would propagate in the case of an ice-slab bending. Bassis and Jacobs [2014] recently modeled the retreat of Helheim glacier with a model of tightly packed particles that interacted via elasticity and broke once a threshold stress was achieved, often due to the influences of basal topography and buoyancy due to flotation. We take their work further by including the effect of viscous stresses on ice deformation.

Future work with DES will explore the use of a brittle-ductile transition zone for this simple slab bending case. Following the results of that work more realistic boundary conditions can be implemented to simulate those processes of immense interest to the cryospheric and climate community, including: tidal and buoyancy stresses and ice shelf melting/accumulation. At present this study has shown that DES can reproduce the brittle rupture of ice, general ice flow characteristics, and idealized patterns of failure in simple situations, and can be recommended as a tool through which future studies of ice failure related to calving and ice dynamics can be conducted.

Parameter	Thickness, m ($\theta = 3°$)	Tilt angle, ° (H = 500m)	Plastic weakening, Pa ($\sigma_T = 1\ MPa\ ;\ \phi = 30°$)
	250	1	$6{\times}10^5 \rightarrow 5{\times}10^5$
	500	3	$6{\times}10^5 \rightarrow 3{\times}10^5$
	750	5	$6{\times}10^5 \rightarrow 1{\times}10^5$
	1000	7	
		9	

Table 2.1: Parameters used in sensitivity study for a tilted, bending slab. Each parameter in the thickness and tilt fields are varied over all three plastic weakening ranges.

Symbol	*Constant*	*Value*	*Units*
ϱ	Density of ice	911	kg m^{-3}
n	Power in Glen's Law	3	-
A	Multiplier in Paterson and Budd (1982)		
	if T < 263 K	3.615×10^{-13}	s^{-1} Pa^{-3}
	if T ≥ 263 K	1.733×10^{3}	s^{-1} Pa^{-3}
Q	Activation energy for creep in Paterson and Budd (1982)		
	if T < 263	6×10^{4}	J mol^{-1}
	if T ≥ 263 K	13.9×10^{4}	J mol^{-1}
σ_T	Strength in tension	1	MPa
K	Bulk modulus	9500	MPa
G	Shear modulus	3000	MPa
c	Heat capacity	2000	J kg^{-1} K^{-1}
k	Thermal conductivity	2.1	W m^{-1} K^{-1}

Table 2.2: Other parameters used in model runs whose values remained constant.

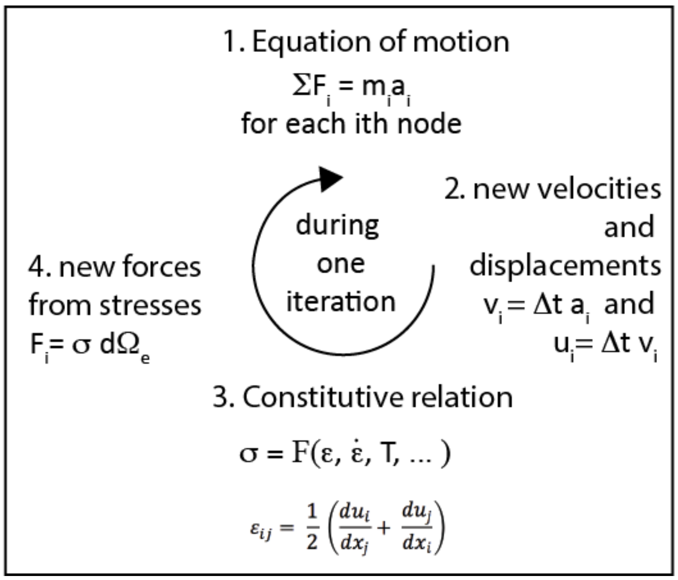

Figure 2.1: Schematic of one interactive cycle in DES.

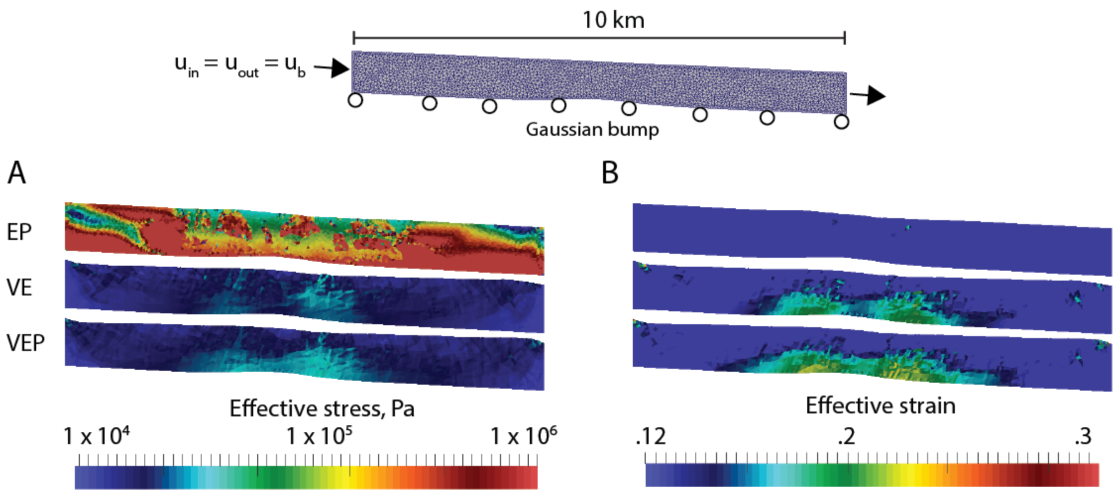

Figure 2.2: Top, showing the scaled experimental setup from the ISMIP-HOM prognostic experiment (Pattyn et al., 2008). Velocity boundary conditions are prescribed to be the same, incoming, outgoing, and on the basal side. [A] Effective stress and [B] effective strain outputs from DES for the 3 different constitutive models. That the VE and VEP models look so similar indicates that the VE stresses are almost always less than the EP stresses in ice, and thus are always chosen by the minimum energy principle.

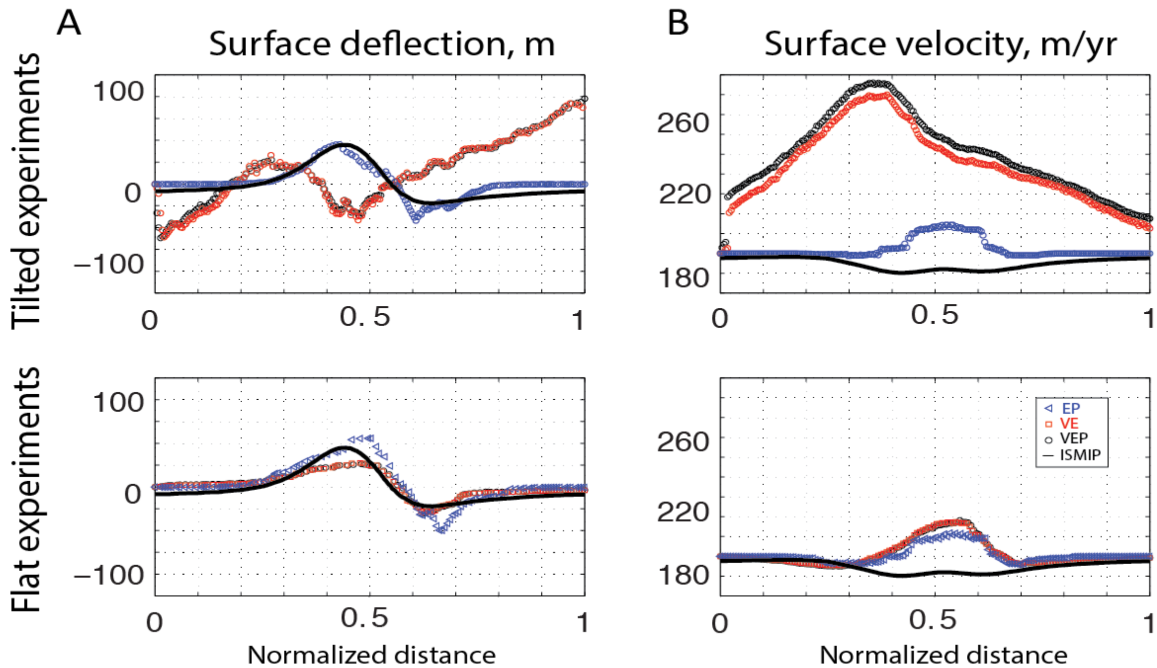

Figure 2.3: The [A] surface deflection and [B] surface velocity of the ice for the tilted (top) and flat (bottom) experiments, forced by the same boundary velocities. The misfit between DES and other models for the ISMIP-HOM experiment shows the disproportionate effect the boundary conditions have on the model. The bottom panels show that when the effect of the boundary conditions are removed there is almost no deviation from results of the other models.

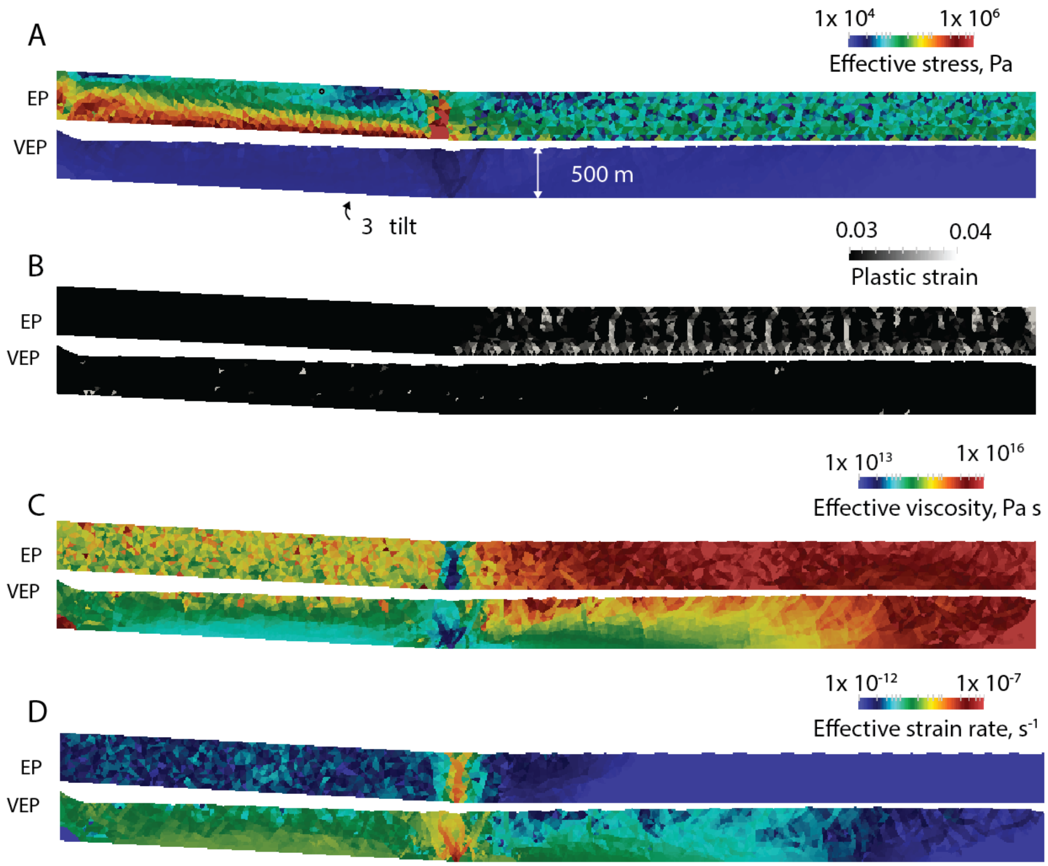

Figure 2.4: [A] Effective stress, [B] plastic strain, [C] effective viscosity, and [D] effective strain rate for a parallel-sided slab advecting down a 3° incline at 300 m yr^{-1} after 25 years real model run time. The VEP rheology is much weaker than the EP as is indicated by the effective viscosity field and the vertical deflection of the VEP surface toward the right-hand side of the domain. EP ice is much stiffer and stress concentrates much more at the grounding line, resulting in regularly spaced vertical lines of failure, whereas VEP rheology results in a diffuse stress field and distributed failure.

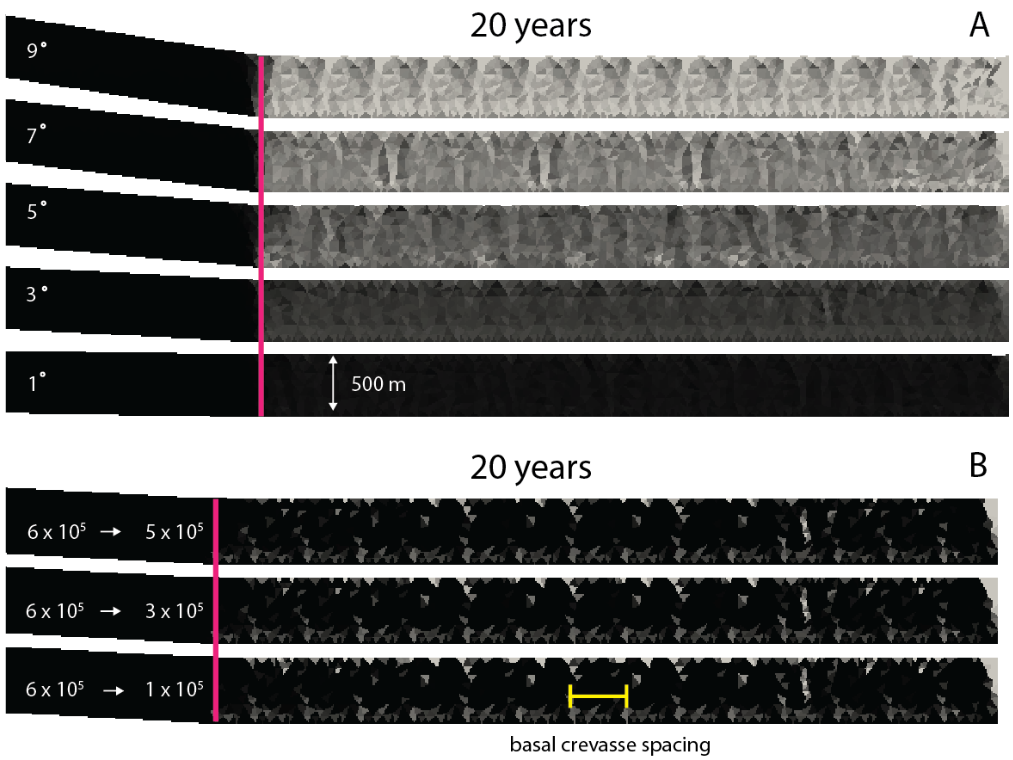

Figure 2.5: Plastic strain fields for experiments with [A] varying tilt degree for a plastic weakening of $6\times10^5 \rightarrow 3\times10^5$ Pa and [B] varying plastic weakening. Higher degrees of bending produced more tightly spaced crevasses and higher levels of damage. Increasing the rate of plastic weakening did not affect the pattern of failure, although higher rates of weakening did produce marginally higher levels of failure. The pink line shows the location of the forced bend.

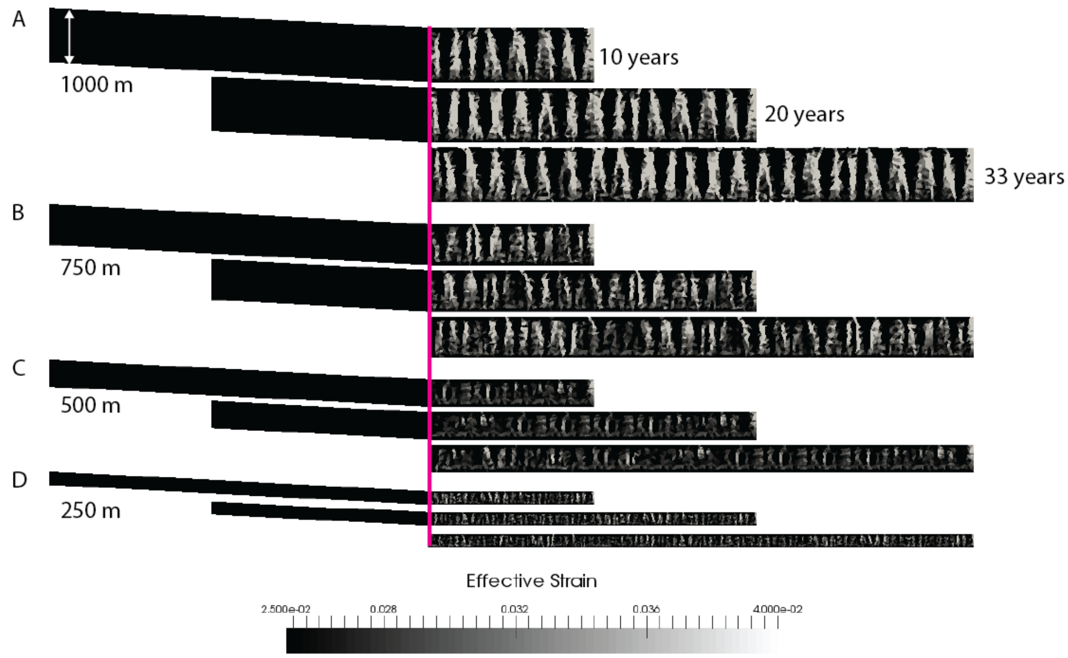

Figure 2.6: Plastic strain fields for experiments with different ice thicknesses, at [A] 1000 m, [B] 750 m, [C] 500 m, and [D] 250 m, for a plastic weakening of $6\times10^5 \rightarrow 3\times10^5$ Pa. The pink line shows the location of the forced bend.

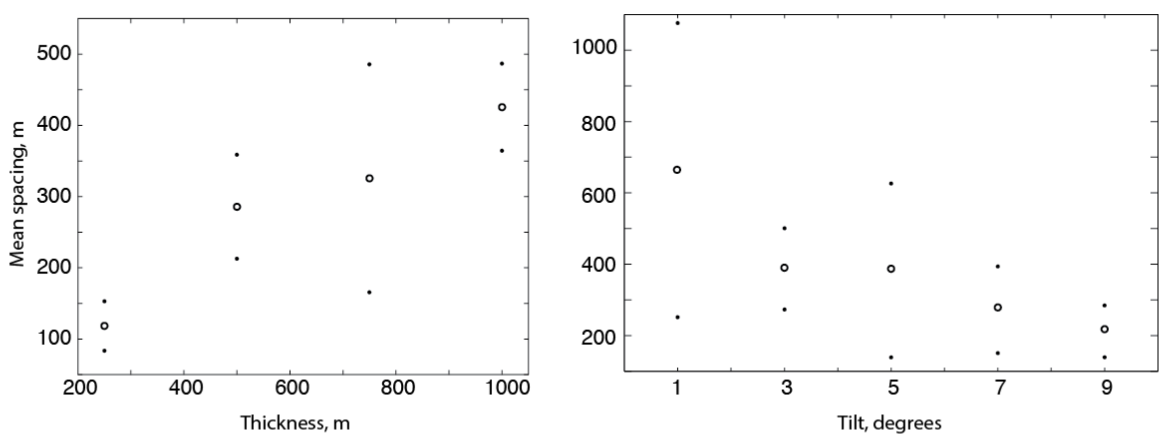

Figure 2.7: Mean spacing of basal crevasses for the two parameter sensitivities explored, [left] ice thickness and [right] bending degree. Means are plotted as open circles with $\pm$ standard deviation plotted as black dots.

Chapter 3: Tidewater glacier calving and the role of basal crevasses

Liz Logan[1], Luc Lavier[1,2], Eunseo Choi[3], and Eh Tan[4]

[1] *Department of Geological Sciences, University of Texas at Austin*

[2] *Institute for Geophysics, University of Texas at Austin*

[3] *Center for Earthquake Research and Information, University of Memphis*

[4] *Institute of Earth Sciences, Academia Sinica, Taipei, Taiwan*

[*] Chapter 3 is a manuscript in preparation.

ABSTRACT

Accurate prediction of mean global sea level rise will depend on our ability to forecast the rate at which ice is discharged from the margins of glaciers and ice sheets into the ocean. However the simulation of mechanical ice mass loss, or calving, from polar ice bodies is a complex and as yet unresolved problem. Recent work has shown that some of the fastest moving glaciers on Earth are calving icebergs whose sizes are determined by the spacing of basal crevasses – fractures that originate on the bottom side of ice and propagate upward – formed through bending at the grounding line, where ice transitions from resting on land to floating in the ocean. We simulate the formation and development of basal crevasses at the grounding line and investigate the role that ice thickness and basal melting rate have on the spacing of these features. We employ a numerical model, DynEarthSol3D, with the capability of accounting for both viscous and elastic stresses and employ a Mohr-Coulomb failure criterion to account for the brittle failure of ice. We show that the implementation of a ductile to brittle transition in the ice sheet as well as the addition of weakening of basal crevasses by water infiltration is critical to simulate the deformation of ice sheet at the terminus. This result may help

provide constraints to predict whether ice sheets are primed to fail catastrophically or calve in a stable ways.

1. INTRODUCTION

The Greenland and Antarctic ice sheets lose mass to the ocean via two mechanisms: basal melting and iceberg calving. While these two processes roughly split the global budget of ice flux to the ocean (Rignot et al., 2013, van den Broeke et al., 2009), the potential for calving to disproportionately impact the rate of ice discharge is extreme. For example, the complete disintegration of the Larsen B Ice Shelf over the course of six weeks in 2002 led to an acceleration of those feeding tributary glaciers that has continued to this day (Rignot et al., 2004; Scambos et al., 2004). Similarly, Jakobshavn Isbrae – one of Greenland's largest outlet glaciers – saw a retreat over a four-year span that has resulted in a 5% increase in ice speed (Joughin et al., 2008). Thus while calving directly accounts for only half of the total ice mass lost to the ocean, the accompanying ice acceleration due to the loss of forces buttressing the ice makes calving a much more dynamic and important problem. Further, because accurate prediction of global sea level rise depends on our ability to predict glacier and ice shelf retreat rates we must understand how calving impacts ice dynamics in a more precise way.

As yet no single theory exists that unifies the different calving styles seen in nature. While the ice shelves that fringe Antarctica typically calve large, stable icebergs many square kilometers in size (Liu et al., 2015), the tidewater glaciers that discharge ice from the Greenland Ice Sheet at its margins often form icebergs that are at their largest on the order of the local ice thickness (Amundson et al., 2010). Some empirical relationships have linked the calving rate at tidewater glaciers to water depth (Pelto and Warren, 1991) or the glacier's terminus height above buoyancy (van der Veen, 1996), but these only apply to glaciers without a floating tongue. Benn et al. [2007] suggested that calving occurs when surface crevasses propagate to sea level; indeed, researchers have largely focused on how surface cracks drive calving. However, recent work has shown that basal crevasses may play a larger role than previously thought in determining the calving rate at some of the world's largest and most dynamic glaciers (Murray et al., 2015). James et al. [2014] showed that the terminus of Helheim Glacier in Greenland is currently calving back to the location where basal crevasses reach the surface of the ice. Similarly, Thwaites Glacier in the West Antarctic Ice Sheet is discharging icebergs equal in size to surface depressions seen just upstream at the grounding line, corresponding to the surface expression of basal crevasses (Figure 1; Logan et al., 2013; McGrath et al., 2012a,b). Basal crevasses are often seen either via their surface expressions which result from the ice above the crack tip sinking to meet hyrdrostatic floatation (Bassis and Ma, 2015) or as diffraction patterns in ice penetrating radar data (Logan et al., 2013). They typically penetrate hundreds of meters vertically into the ice and are spaced usually at regular intervals, typically about 1 km apart (e.g., the Larsen C Ice Shelf, McGrath et al., 2012; Thwaites Glacier, Logan et al., 2013) although they can be spaced much closer, at several hundred meters apart (e.g., Kamb Ice Stream, Logan et al., 2013). Thus it may appear that basal crevasses provide a first-order control on the calving rate at some of the most dynamic glaciers in the world. Understanding calving through the lens of basal crevasse formation may provide a great deal of insight for researchers trying to provide more accurate sea level rise projections.

A glacier can calve in several ways: the 'serac style', in which a highly crevassed marine-terminating glacier effectively crumbles from surface crevasses meeting the base of the glacier at the ice tongue, often aided by extreme basal melting (e.g., Bartolomaus et al., 2013); intermittent tabular iceberg calving, where full thickness rifts in the ice propagate periodically and eventually meet, releasing a large, stable mass of ice (common in large ice shelves; e.g., Joughin and MacAyeal, 2005); and a basal crevasse-aided calving event, which releases an ice berg smaller than the massive tabular bergs but larger than the serac style masses, which occurs in marine-terminating glaciers approaching floatation (e.g., Murray et al., 2014). The concept that basal crevasses – as opposed to surface crevasses – provide the largest control on calving rates at tidewater glaciers is rather new and so not many researchers have developed models for glacier retreat that are basal crevasse-centric. Logan et al. [2013] showed that a thin-elastic beam approximation for ice could be used to predict order-of-magnitude size basal crevasses seen at the grounding lines of Antarctic ice streams in radar data, but this model did not provide for the temporal development of the basal crevasses in a way that could readily be applied for calving studies. Bassis and Jacobs [2014] used a discrete particle model to show the development of basal crevasses throughout time, eventually forming tabular icebergs. The rheology in both of these studies included elasticity and utilized Mohr-Coulomb failure criterion, but lacked consideration for the viscous components of stress widely assumed to capture the long-term flow of ice. Other studies however have shown a strong correlation between calving rate and strain rate, which is typically used to estimate viscous stresses in ice (Alley et al., 2008). Thus a model that incorporates both elastic and viscous stresses while providing a framework for the temporal evolution of ice failure would be ideal for testing those parameters that most greatly impact the formation and development of basal crevasses.

In this paper we study the formation of basal crevasses at grounding lines, where bending stresses due to buoyancy are highest and believed to promote ice failure. We extend the work of previous authors by using a numerical model with visco-elasto-plastic rheology, DynEarthSol3D (DES; Tan et al., *in prep*; Choi et al., 2013). DES enables us to account for viscous and elastic stresses while simulating the brittle failure of ice throughout time.

2. EXPERIMENTAL SETUP: GEOMETRY AND RHEOLOGY

We performed a suite of idealized experiments to examine the relationship between the spacing of basal crevasses – which are represented by zones of brittle failure in DES – and the local ice thickness and basal melting rate applied to the floating ice tongue. DES solves the fully dynamic momentum balance equation and conservation of energy and ice can be treated as a Maxwell viscoelastic or visco-elasto-plastic solid (Logan et al, in prep, Chapter III).

The ice is initially given a wedge-shaped profile of varying thicknesses (Figure 2). The gradient in ice thickness drives the ice flow entirely, and the ice rides over a frictionless base. Buoyancy forces are applied to the boundary elements once they advect past a fixed grounding line at 48 km. This means that two stresses are applied to boundary elements that are floating: the first balances the weight of the ice column that has displaced water and is below sea level, while the second is a time-varying diurnal tide that corresponds to a 1 m fluctuation in water height (Brunt and MacAyeal, 2014). While these are extremely idealized conditions – ice glides over a flat, frictionless base, the left-hand side of the domain is pinned by enforcing the horizontal velocity equal zero – the previous chapter has shown that in DES the boundary conditions can affect the ice flow and deformation to a large degree. Maintaining simple boundary conditions and bedrock geometry allow us to attribute patterns of deformation to the choices in rheology and initial geometry. We found through trial and error that a triangular wedge of ice added to a uniform thickness slab – thick on the left-hand side of the domain and tapering to the right – provided enough gradient in thickness to drive the flow of ice at speeds comparable to those where basal crevasses are observed in nature: on the order of hundreds of meters to several kilometers per year. As is common in the literature (Larour et al., 2012; Isaac et al., 2014), we make use of Glen's flow law to determine the ice viscosity, taking the full non-linear form:

$$\eta = \frac{1}{2}A^{-1/n}\dot{\varepsilon}_e^{(1-n)/n} \qquad (1)$$

where A is an Arrhenius relationship that accounts for temperature, $\dot{\varepsilon}_e$ is the effective strain rate, and n is the flow law exponent, set to 3. We set a minimum allowable viscosity to 1×10^{13} Pa s. For both Maxwell and visco-elasto-plastic solids the minimum viscosity corresponds to a relaxation time of about 1 hour. The typical explicit time step in DES is 150 s which is less than the Maxwell relaxation time, ensuring that we are properly resolving elastic stresses. We set the base of the ice equal to 0℃ and the surface to -30℃ with a linear thermal gradient for the ice interior (MacAyeal, 1991). We initialized the domain with a coarse resolution of 100 m, anticipating that DES' ability to dynamically remesh would develop much finer resolution in areas of failure.

We first run the experiments using a Maxwell viscoelastic rheology (Figure 3) to establish a baseline result in ice flow so that we can understand the effects of the inclusion of brittle failure on the ice dynamics. For experiments with a visco-elasto-plastic rheology, we make use of a ductile-brittle transition zone based on longitudinal strain rate to determine whether the ice at any given element behaves in a brittle or ductile manner (following Schulson and Duval, 2009). We approximate ductile behavior using Maxwell viscoelasticity and brittle behavior using Mohr-Coulomb elastoplasticity, where ice follows a non-associative plastic flow law once failure in shear or tension has been reached. Once ice has failed in a brittle fashion it remains brittle: ice that has accumulated more than .0025 plastic strain continues to be evaluated as elastoplastic (Mahrenholtz and Wu, 1992). For the Mohr-Coulomb failure threshold we have an initial cohesion of $6x10^5$ Pa that decreases linearly to $1x10^5$ Pa over .001 accumulated plastic strain (chapter II). We set the angle of internal friction to 30° (Schulson, 2006) and use a tension strength of σ_T = .1 MPa (Schulson and Duval, 2009). The geometric setup and set of parameters explored used in the experiments are outlined in Figure 1 and Table 1, respectively. Choi et al. [2013] and Logan et al., [in prep, chapter II] present a more detailed explanation on the numerical methods employed in DES.

All experiments are performed for three different ice thickness values, H = {300, 600, and 900} m, with each thickness undergoing a range of basal melting rates of $\dot{m}$ = {0, 10, 20, and 30} m yr^{-1}, which are applied once an element has advected past the fixed grounding line and uniformly along the entire length of the floating tongue. The suite of experiments performed is as follows: 1 – purely Maxwell viscoelastic material without failure and different basal melt rates (Figure 3); 2 – visco-elasto-plastic (VEP) material with a ductile-brittle transition zone based on longitudinal strain rate (Figure 5); 3 – VEP material and a drop in angle of internal friction to simulate the effect of water saturation within basal cracks in the ice (Figure 10); 4 – VEP material and drop in internal friction simulated for Thwaites Glacier (Figure 16).

3. RESULTS

3.1 Viscoelastic ice only

Ice takes the full range of nonlinear viscosity here, shown for the zero melt rate case in Figure 3. Ice is weakest at the grounding line where the buoyancy and tidal stresses are first applied. Stresses here are also the highest, as shown in Figure 3A-C; indeed, for all three ice thicknesses and melt rates stresses are highest at the grounding line. Thicker ice experiences correspondingly higher effective stress (defined as the second invariant of the stress tensor), at just over 1 MPa, while the thinner ice experienced a maximum effective stress in the hundreds of kPa. Stresses are also high at the surface of the right-hand side of the domain, where ice is often highly crevassed and calving of the terminus cliff occurs (although this is not simulated in our model). A force imbalance acts on the ice front as the portion of ice above water is stress-free while submerged ice feels increasing pressure with water depth. The result is an overhanging terminus cliff tilted seaward. The overhanging terminus cliff is most tilted for the thickest ice, where higher stresses are applied to thicker ice submerged deepest in water.

Figure 3D-F shows that the highest effective strain rates (the second invariant of the strain rate tensor) in the domain are also at the grounding line. We use this field to set a strain rate threshold for brittle behavior in later experiments, and confirm that the threshold lies in the range that Schulson and Duval [2009] reported, of approximately 10^{-8} to 10^{-7} s^{-1}.

Finally, we explored the effect that basal melting has on ice approximated as a viscoelastic material. Figure 4 shows the terminus velocity after 6 months real model runtime for the three thicknesses each with 0, 10, 20, and 30 m yr^{-1} basal melting. All three ice thicknesses experience increasing terminus velocity with increasing melt rate, with the terminus velocity also increasing with ice thickness. The thickest ice flowed at a maximum velocity of about 7200 m yr^{-1} while the thinner ice flowed at less than 6000 m yr^{-1}, experiencing a much greater increase in velocity with melt rate than the thicker ice. The effect of added melting in thinner ice increased the terminus velocity by almost 500 m yr^{-1} whereas the thicker ice increased in velocity by about half that amount.

3.2 Visco-elasto-plastic ice

Using the Mohr-Coulomb properties listed in Table 1 that are compatible with Schulson and Duval [2009] and a brittle-to-ductile transition zone based on longitudinal strain rate, we simulated the visco-elasto-plastic (VEP) behavior of ice as it advects over a grounding line with no melting. The VEP rheology employed here is an extension of the work presented in chapter II and supported by laboratory data (Schulson and Duval, chapter 9, 2009) that show that a stiffening of ice at high strain rate will be accompanied by fracture only at correspondingly high tensile stress (from 10^5 to 10^6 Pa) (Bassis and Jacobs, 2014; Schulson and Duval, 2009). The strain rate dependent nature of the transition from ductile to brittle implies that – depending on the viscosity – fracture in ice occurs on time scales of less than a few seconds to hours, which DES easily resolves. When the local strain rate of the ice exceeds the threshold value, set here to 10^{-7} s^{-1}, ice experiences stresses greater than 0.1 MPa (from chapter II) and will fail in a brittle manner and deform according to a non-associative plastic flow law.

Figure 5 shows the effective stress, strain rate, and viscosity at 6 months real model run time. Stresses at the grounding line in this simulation are higher than those with only Maxwell rheology (increasing from ~0.2 MPa to ~0.5 MPa): the thickest ice had a maximum effective stress of approximately 3 MPa, with the value decreasing to about 1 MPa for the thinner ice – all of these occurring at the grounding line.

Figures 6, 7, and 8 show the plastic strain field – which shows the level of strain an element undergoes once it has reached the failure envelope – for all three ice thicknesses with zero basal melt rate applied. Ice at the surface is regularly and heavily strained as the yield strength there is the lowest (this is the case for all frictional materials in the vertical plane). This effective strain increases with time as the floating tongue is allowed to relax into the water – reaching effective strains of approximately .75 to 100 m deep below the ice surface. As the floating portion of the ice extends further and further into the water the ice thins, allowing for necking at the grounding line. This thinning as ice begins to float is a feature of marine-terminating ice sheets. The thickest ice thins by

~400 m – almost half the original ice thickness – while the thinnest ice sheet (originally 300 m) thins by less than 50 m, almost 16%. However the basal side of the ice shows very little damage: only several elements have reached the brittle failure. The pattern remains the same for ice undergoing all rates of melting applied and so we only show the zero melt cases. Ice velocities drop with the inclusion of brittle failure, although ice velocity still increases with increasing melt (Figure 9). The velocities for the thickest and thinnest ice have decreased by just over a kilometer per year. Similarly, the increase in velocity due to melting has also decreased, although the largest speedup is still experienced by the thinnest ice, at approximately 400 m yr^{-1}.

3.2 Visco-elasto-plastic ice with added 'water' weakening

Because our results from a purely VEP simulation indicated that a ductile-brittle transition zone is not sufficient to produce basal failure, we included an extra measure of weakening to account for the effect of buoyant water in basal cracks. For any element that has failed below sea level we decrease the angle of internal friction from ϕ = 30° to ϕ = 7°. Trial and error indicated that a decrease from 30° to 7° was necessary to produce the observed basal crevasse fields. We do not explicitly model water flow or simulate the intrusion of water into failed elements; rather the decrease in angle of internal friction *represents* the mechanism of buoyant water infiltrating cracks, subsuming this process into the Mohr-Coulomb weakening properties

We again show the resulting stress, strain rate, and viscosity fields after 6 months real model run time (Figure 10). The maximum effective stresses in this case are yet still higher, with values of 6 MPa, 3 MPa, and 2.5 MPa experienced at the grounding lines of the 900, 600, and 300 m thick ice. With the inclusion of this rule, failure at the grounding line occurs with regularity. Figures 11, 12, and 13 show the plastic strain fields for ice of thicknesses 900, 600, and 300 m, respectively. The plastic strains, reaching values greater than 1 for the 900 and 600 m thick ice, extend roughly halfway through the thickness of the ice, approximately 450 to 300 m in height, while the 300 m thick ice experiences plastic strains of approximately .5 that essentially extend through the entire thickness of the ice. These figures also show that toward the end of the simulation time the floating tongue has accumulated so much strain that it begins to form boudin-like structures, very much like those see on Pine Island and Thwaites Glaciers (Bindschadler et al., 2012; Logan et al., 2013). We define boudins by their corresponding undulated bottom and surface topography, with the bottom topography deriving its shape from the propagation of basal crevasse failure zones and the surface topography where the ice surface sinks toward the apex of a basal crevasse, meeting hydrostatic floatation and necking due to high strain (seen in Figure 19). This is especially pronounced in the thinnest ice (Figure 13). While the basal crevasses form sequentially, that is – failure zones to the right of the domain are older than those to the left – these features develop into the characteristic boudin-like shape all at the same time. Once the ice has lost all its driving stress the ice begins to thicken just beyond the grounding line, which is a consequence of the boundary conditions and the lack of true bedrock below the ice. Similar to the previous cases the viscous necking of the ice tongue still occurs even though the ice is behaving partly in a brittle manner. The ice sheet thins by about a third of the initial thickness. This time the amount of thinning is independent of the initial thickness.

With the inclusion of the extra failure criterion we are able to observe the basal crevasse spacing as a function of thickness and melt rate (Figure 15). While it remains true in this case that thicker ice flows faster than thinner ice, increasing melt rate for these simulations lead to decreases in velocity. Ice flows mostly faster than in the previous case (without the added water-assisted basal failure), with thicker ice flowing approximately

6000 to 7000 m yr^{-1}, and thinner ice flowing between 5500 and 3750 m yr^{-1}. Melting however decreases the terminus velocity, by approximately 1500 m yr^{-1} for all ice thicknesses. In this case basal crevasse spacing decreases with increasing melt rate, and the thinner ice produces the widest spaced basal crevasses, whereas thicker ice produces basal crevasses that are more closely spaced. Basal crevasses formed in thicker ice about every 700 m while in thinner ice basal crevasses were spaced about every 800 m. Increased melting produced a decrease of about 250 – 300 m between the spacing of basal crevasses in all ice thicknesses.

3.3 Thwaites Glacier

Using Operation Ice Bridge data flown over the center line of Thwaites Glacier (Figure 19; Joe MacGregor, personal correspondence), we generated a mesh to simulate the flow and deformation of the glacier for two years. We ran these simulations for varying levels of basal melt, $\dot{m}$ = {0, 10, 20, and 30} m.yr^{-1}, (for comparison, Thwaites Glacier has an estimated 18 m yr^{-1} of basal melting, Rignot et al., 2013) and found no difference in the results at all and so we show results with zero melt rate. The velocity structure of the simulation largely matches observations (Rignot et al., 2011), with a terminus speed of approximately 3 km yr^{-1} and ice speed upstream of the grounding line at the location simulated here of approximately 300 m yr^{-1} (Figure 18). The ice advects about 20 km over the grounding line. Our simulation shows a slight decrease in velocity as the ice rides over the bump upstream of the grounding line, which acts as a resisting feature for ice flow. Figure 16 shows the effective stress, effective strain rate, viscosity, and velocity after 2 years real model run time. These outputs confirm that basal topography influences the stress and strain rate fields enormously: viscosities immediately preceding and following the bump in basal topography are 1 to 2 orders of magnitude smaller than the viscosities elsewhere. Effective stresses are highest immediately preceding and following the bump in basal topography, at values just exceeding 1 MPa. Following the change in boundary conditions the effective stresses drop, as soon as the ice is floating, to the order of tens of kPa. The viscosity of the floating tongue however is high, indicating that this portion of the ice is stiffer and more apt to break in a brittle manner. Figure 17 shows the failure pattern for the ice after 2 years; failed ice representing basal crevasses extends several elements into the ice thickness, measuring approximately 200 – 300 m in height. Near the grounding line, just as in the idealized, wedge-shaped experiments above, the ice fails sequentially, with older crevasses to the right-hand side in the domain, and the boudin-like features form shortly after the ice has failed. However evenly spaced fractures form initially in the floating ice tongue. After 2 years the floating ice tongue begins to form the boudin-like structures seen toward the end of the idealized glacier experiments. These are located with a mean spacing of 730 m apart and a standard deviation of 675 m. The boudin-like structures do not correlate with every basal crevasse however, which have a mean spacing of 1590 m and a standard deviation of 1030 m. Logan et al. [2013] measured the spacing of the surface depressions corresponding to basal crevasses on Thwaites Glacier and found a mean spacing of 1034 m and a standard deviation of 217 m.

4. Discussion and Conclusion

We find that for viscoelastic ice, increases in melting correlate with higher terminus velocities and that thicker ice flows faster than thinner ice. Ice simulated here flows only under the force of gravity and behaves essentially as a fluid. These model results make sense: higher melt rates lead to higher gradients in ice thickness, which produce greater longitudinal stress gradients within the ice, causing it to flow faster. Thicker ice has a higher gravitational potential and so discharges faster across the grounding line. Additionally, fast flowing ice and high thickness gradients produce plastic necking, where the ice thins preferentially due to high effective strains. This plastic necking causes even more thinning, adding to the gradient in thickness and driving the flow even faster. While the most commonly cited reason for positive correlations between ice velocity and basal melt rate invoke loss of resistive frictional forces (e.g., Joughin et al., 2008), our static grounding line precludes this as an explanation. Indeed we believe that were DES capable at this point in allowing the grounding line to migrate, we would see an additional signal of velocity increase in our results. However as this is not yet a feature in the model the only reasonable conclusion is that higher melting drives faster flow through increasing ice thickness gradients.

We also see that viscoelastic ice flows faster than our visco-elasto-plastic ice. The inclusion of a strain rate threshold for brittle behavior in our rheology means that, whereas before every element in the domain behaved as a lower viscosity fluid, elements with high strain rate now behave as a yielding elastoplastic solid. The effective viscosity for such elements can be as much as an order of magnitude higher and so their response is to deform slower. A comparison of Figure 3G-I and Figure 5G-I shows that the process zone for the grounding line is smaller for VEP ice – that is, ice there is largely stiffer than for purely viscoelastic ice. The result is that stiffer ice flows slower across the grounding line. Additionally, VEP ice exhibits higher stress levels than in VE ice only: in chapter II we established that the elastic stresses are always higher than the viscous stresses in ice, which is why VEP simulations where the choice between viscous and elastic behavior were determined by the minimum energy principal resulted in stress fields that appeared to be almost entirely viscous. With the application of a strain rate threshold, however, regions that are straining quickly are evaluated as elastic, and thus experience higher effective stress values.

A very important result comes out of a comparison between purely VEP ice and VEP ice with added failure to simulate the effect of water in basal cracks. A comparison of the patterns of failure for purely VEP ice (Figures 6, 7, and 8) versus ice with water saturation failure (Figures 11, 12, and 13) shows that without the extra drop in strength due to water-filled cracks, basal crevasses do not form with any regularity. Several researchers (e.g., Bindschadler et al., 2011 in Figure 18; McGrath et al., 2012a; Luckman et al., 2012; Logan et al., 2013) have observed radar diffraction patterns indicating that basal crevasses originating from the grounding lines of glaciers form with a marked regularity – typically spaced approximately every 1000 m. That DES is unable to simulate this regular formation of basal crevasses using the VEP rheology alone is important: the added mechanism of ice weakening due to the filling of voids with buoyant ocean water is a crucial mechanism by which these features are formed. Without this process ice remains largely intact and strong.

One puzzling result is shown in Figure 14: whereas all ice bodies show increases in velocity with increases in melting, VEP ice with added water failure does not follow this trend. Ice melting without the extra water-assisted basal crack failure maintains a fairly uniform profile: it does not form boudin-like structures. However with the inclusion of the extra failure mechanism the floating tongue loses this uniformly thinning geometry, and so loses the extra driving force of a smooth gradient in ice thickness. Thus when the floating ice tongue begins to form boudins it no longer derives extra velocity from a gradually thinning tongue, and all of the deformation is focused on the thinning of failed ice. Were DES able to remesh based on output variables such as plastic strain (instead of geometric requirements based on the mesh) this would result in full-thickness ice rifts, and thus directly simulate calving.

With the inclusion of water-aided basal failure we are able to observe several key characteristics of basal crevasse formation. The first is that basal cracks indeed create the boudin-like features observed universally in floating ice masses (Bindschadler et al., 2011; Luckman et al., 2012; McGrath et al., 2012; Logan et al., 2013). Figures 11, 12, and 13 show that, once enough strain in the floating ice tongue has accumulated, the basal surfaces that have failed begin to stretch up into the thickness of the ice and the surface above these failure zones begin to sink down. These features can be seen in many places, and are most easily spotted at the surface in satellite imagery as regularly spaced surface depressions or undulated topography. As in the cases of Helheim and Thwaites Glaciers, calving eventually occurs at these thin spots where the ice is more susceptible to fatigue from tidal motion and extra thinning from melt. We also see that basal crevasses are spaced relatively wider in thinner ice than in thicker ice (Figure 15). This is likely because thicker ice that is at floatation experiences higher stresses at the base and grounding line and thus is able to reach the failure threshold more often than thinner ice, which experiences correspondingly lower stresses to maintain floatation. A comparison of the simulated basal crevasse spacing for 300 m thick ice with a mean value of approximately 800 m compares well with basal crevasses observed by Luckman et al. [2012] in the Larsen C Ice Shelf, which are spaced on average 1 km apart and a corresponding ice thickness of approximately 300 m. Similarly, basal crevasse spacing downstream of the grounding line of Kamb Ice Stream, in the Siple Coast of Antarctica, shows a mean spacing of 832 m in 600 m thick ice, which compares well with our simulation of 750 m spacing in 600 m ice.

From our Thwaites Glacier simulations we can draw several important conclusions. The first is that the added process of basal melting can only lead to ice acceleration if the grounding line can migrate. Our simulations, which do not include grounding line retreat due to melting, show no increasing velocity with increasing melt rate. If numerical models are to accurately capture ice acceleration due to melting the inclusion of a moving grounding line is a crucial process to simulate. Secondly, while our boudin-like structures do not always match the location of ice failure, their spacing corresponds reasonably well with observed spacing of boudin features measured on Thwaites previously, of 1034 m (Logan et al., 2013). If DES is to be used in the future to estimate the calving rates of other glaciers, we can expect reasonable agreement between modeled and observed crevasse spacing. Thirdly, the presence of a bump in basal topography affects the flow and strength of ice enormously. The viscosity field in Figure 16D shows that ice there is an order of magnitude weaker than the ice immediately upstream and downstream of the bump. This bump has a width of approximately 10 km, meaning that models attempting to capture the accurate flow of ice with nonlinear viscosity need kilometer to sub-kilometer resolution at the grounding line.

The manner in which the floating tongue deforms – for both the wedge-shaped and Thwaites Glacier simulations – is critical: both modes of deformation lead to the geometric development of the ice as it achieves floatation. Brittle failure of the ice occurs immediately at the grounding line, weakening the ice there through the Mohr-Coulomb properties. Subsequent viscous deformation leads to the formation of the boudin like features, so that the shape of the tongue ultimately reflects a truly semi-brittle rheology. But while the ice fails sequentially at the grounding line, the boudin features develop all at once in the floating portion of the tongue. Once the ice has failed the plastic weakening properties prime the ice for further deformation, leading to plastic necking and boudinage. Although the shapes are more exaggerated in cases with high levels of melting, this occurs for all simulations. The wholesale development of these boudinage features implies that the ice is primed for large-scale failure. That is, the boudinage that develops in the floating portions of glaciers and ice shelves indicates that large-scale disintegration is a possibility, given that the ice is weakening and necking at all locations where a basal crevasse exists all at once.

Boudinage may be explained physically by the fact that opening basal fractures allow for water to drive deformation further by buoyancy driven processes (Bassis and Walker, 2011), and pinches the ice tongue at this location. The initial wavelength of the pinch and swell structures is imposed either by sequential deformation at the grounding line or widespread coincident semi-brittle deformation in the ice tongue.

We believe that the most important result from the suite of experiments performed here is the success DES has shown in making use of a ductile-brittle transition to determine whether or not the ice behaves in a Maxwell viscoelastic or a Mohr-Coulomb elastoplastic manner. To our knowledge no other numerical simulations have explored this possibility, although such a transition is well-established through laboratory studies (Schulson and Duval, 2009). Whereas authors have previously neglected the simulation of both brittle and ductile behavior in ice – choosing simply to approximate stresses using either purely elastic (Bassis and Jacobs, 2014), viscous (Borstad et al., 2012), or viscoelastic frameworks (Duddu et al., 2013) – we have shown in this work that DES is able to self-consistently model the flow of ice using visco-elasto-plasticity. This numerical formulation is especially useful in simulating ice flow on the year to decade scale and helpful in understanding the conditions that lead to patterns of ice failure that may ultimately determine the calving rate of glaciers. As yet larger numerical models that simulate entire ice sheet flow struggle to simulate the retreat of ice at their margins via calving (e.g., Larour et al., 2012). DES and its use of the ductile-brittle transition zone then could prove very useful in establishing and testing different calving relationships, based on its ability to accurately simulate ice deformation and its flexibility in employing different boundary conditions and geometries.

Symbol	*Constant*	*Value*	*Units*
ϱ	Density of ice	911	kg m^{-3}
n	Power in Glen's Law	3	-
A	Multiplier in Paterson and Budd (1982)		
	if T < 263 K	3.615×10^{-13}	s^{-1} Pa^{-3}
	if T ≥ 263 K	1.733×10^{3}	s^{-1} Pa^{-3}
Q	Activation energy for creep in Paterson and Budd (1982)		
	if T < 263	6×10^{4}	J mol^{-1}
	if T ≥ 263 K	13.9×10^{4}	J mol^{-1}
σ_T	Strength in tension	.1	MPa
K	Bulk modulus	9500	MPa
G	Shear modulus	3000	MPa
c	Heat capacity	2000	J kg^{-1} K^{-1}
k	Thermal conductivity	2.1	W m^{-1} K^{-1}
η_{min}	Minimum viscosity allowed	10^{13}	Pa s
c	Cohesion drop over .001 plastic strain	$6 \times 10^{5} \rightarrow 1 \times 10^{5}$	Pa
ϕ	Angle of internal friction	30	°
H	Ice thickness of right-hand side	300, 600, 900	m
$\dot{m}$	Basal melting rate	0, 10, 20, 30	m a^{-1}

Table 3.1: Parameters used in DES simulations.

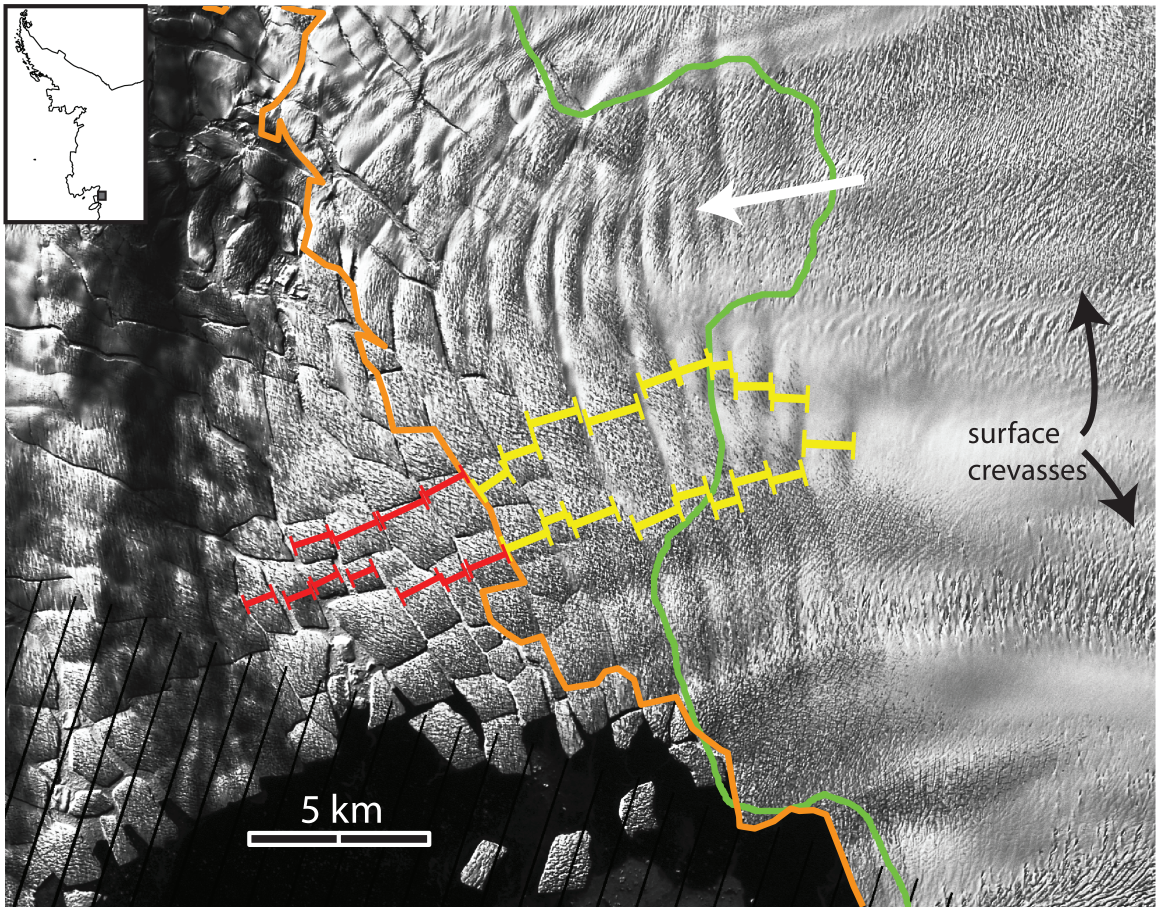

Figure 3.1: Landsat-7 ETM+ band 8 (15 m resolution) image of Thwaites Glacier (from January 2013) and MOA-derived grounding line (green line). Ice velocity is indicated by the thick white arrow. Surface crevasses appear as highly textured areas indicated by the black arrows. Spacing between topographic undulations (yellow bars) is compared to iceberg width (red bars). Ice still connected to TG is upstream of the calving front (orange line). Average distance between surface depressions is 1034 m; average width of icebergs is 1035 m (standard devations 217 and 224 m, respectively).

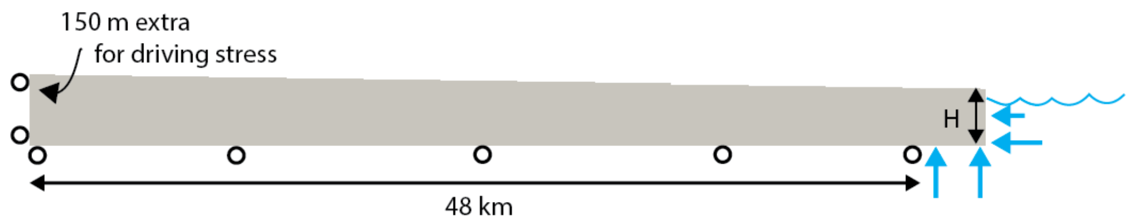

Figure 3.2: Schematic of experiments. All experiments are 48 km long with a fixed grounding line at 48 km and an initial 2 km of floating tongue. We vary the thickness of the base rectangle, H, and give each rectangle a driving stress with an extra 150 m of ice on the left-hand side of the domain which tapers off to H on the right-hand side. The left-hand side velocity is fixed horizontally. Hyrdrostatic stress is applied to the bottom and right-hand side of the domain past 48 km, and different melt rates are applied to the nodes there.

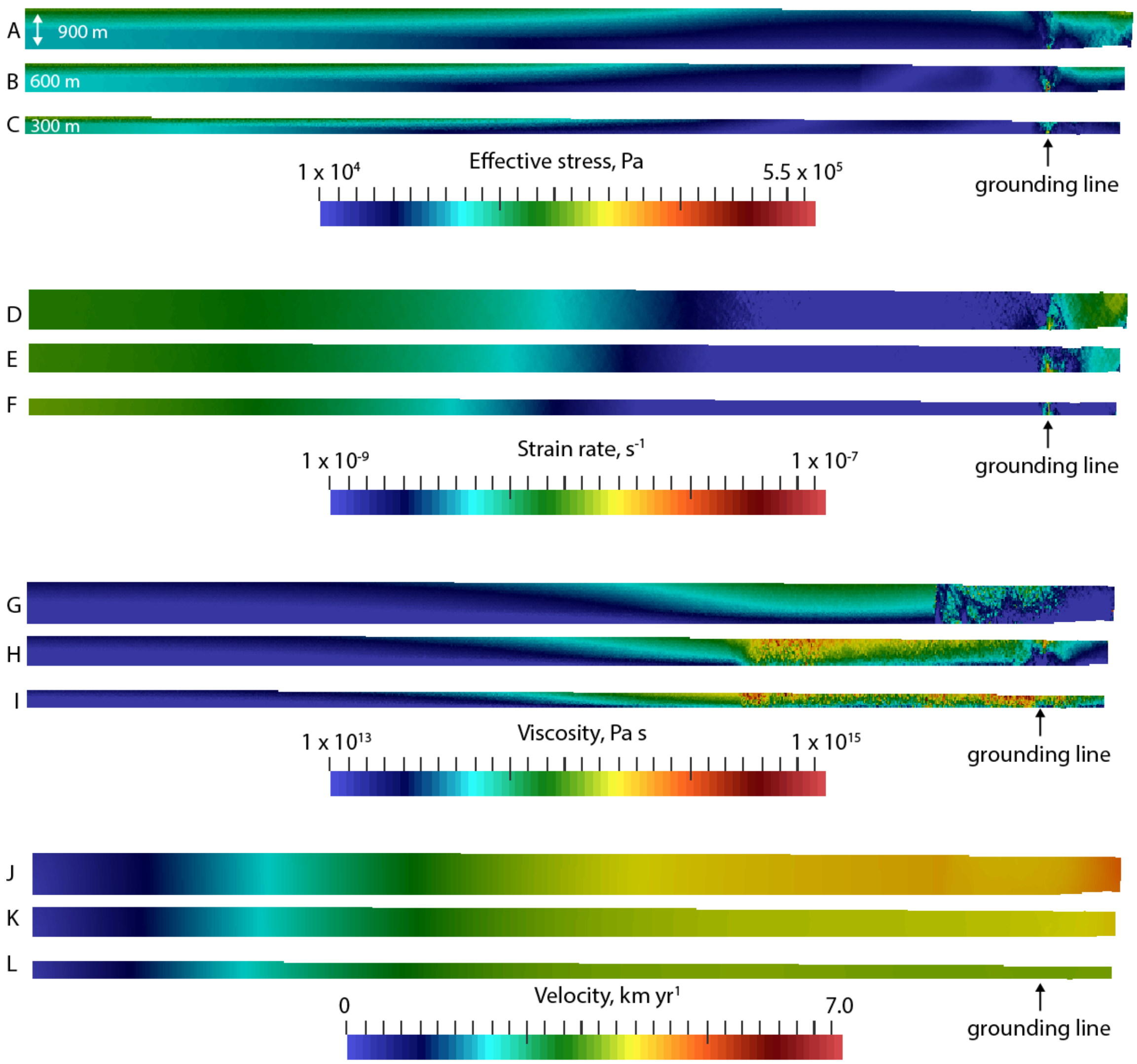

Figure 3.3: Outputs for viscoelastic ice after 6 months real model run time. [A-C] Effective stress, [D-F], effective strain rate, [G-I] viscosity, and [J-L] velocity for all three ice thicknesses with no applied basal melt. The grounding line is indicated by the black arrow.

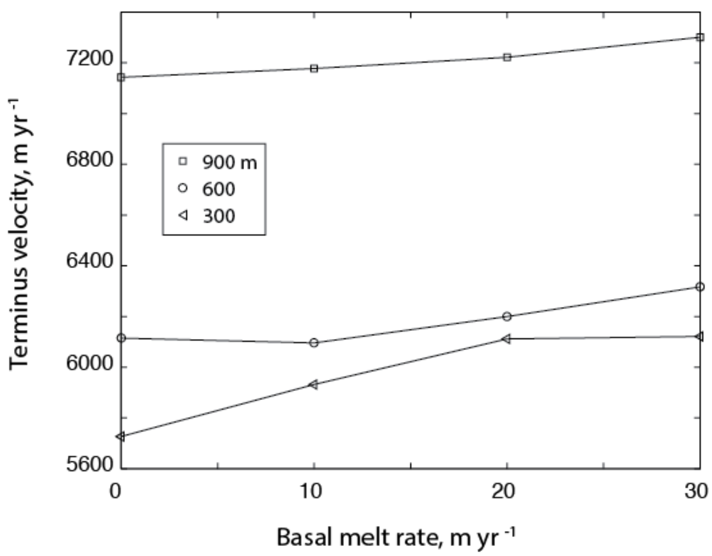

Figure 3.4: Terminus velocity for three different thickness wedges with different applied basal melt rates. All three thicknesses see increasing velocity with increasing melt rate.

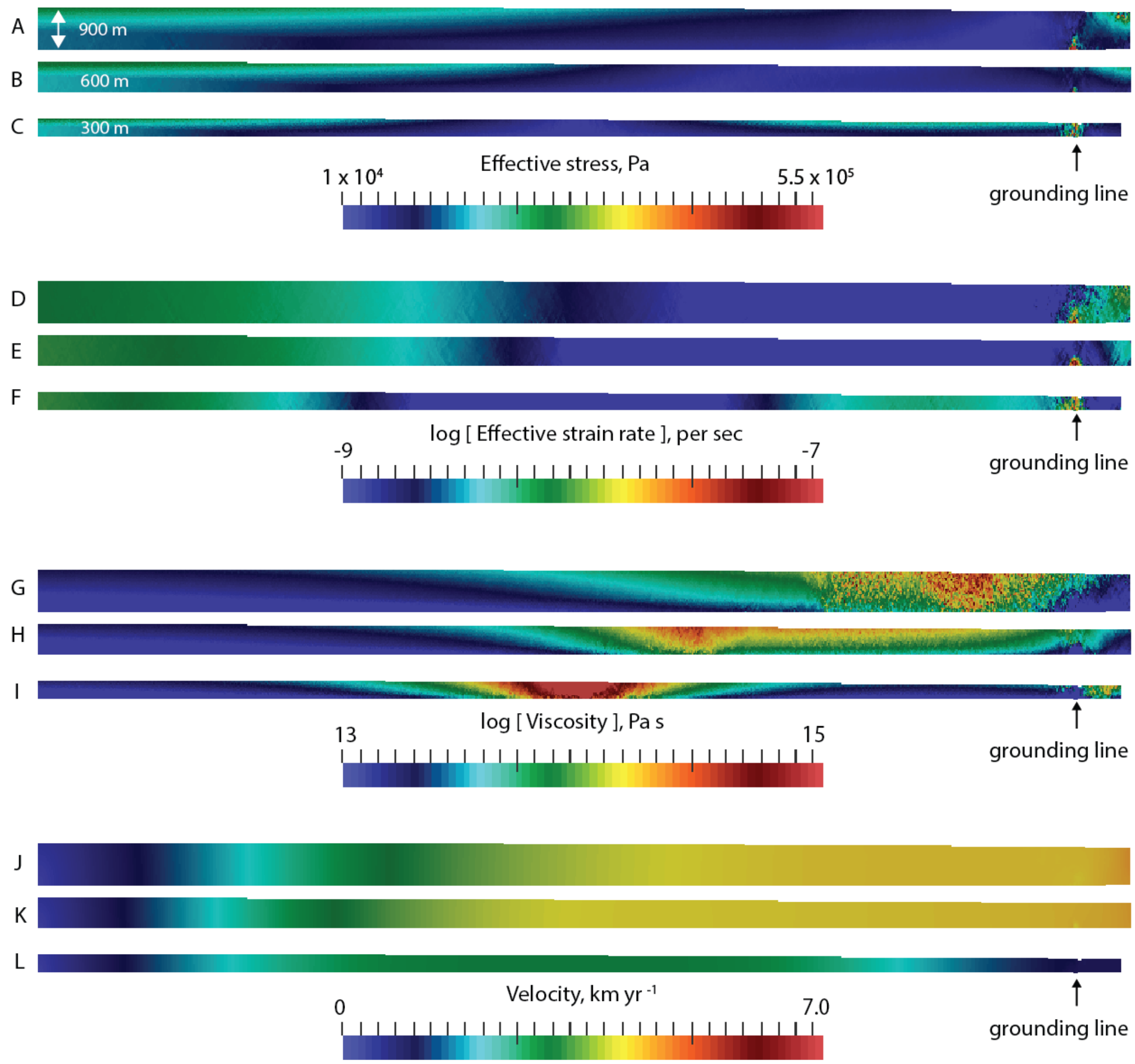

Figure 3.5: Outputs for visco-elasto-plastic ice after 6 months real model run time. [A-C] Effective stress, [D-F], effective strain rate, [G-I] viscosity, and [J-L] velocity for all three ice thicknesses with no applied basal melt. The grounding line is indicated by the black arrow.

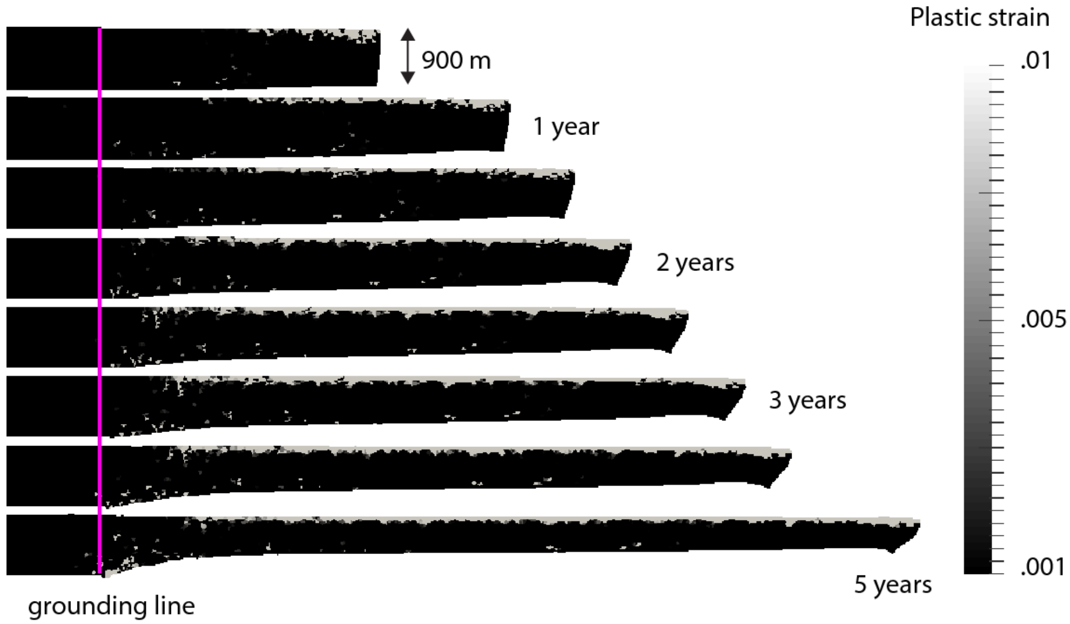

Figure 3.6: Plastic strain field for 900 m thick ice over 5 years real model runtime. Ice fails in tension at the surface near the terminus, and sporadically at the base.

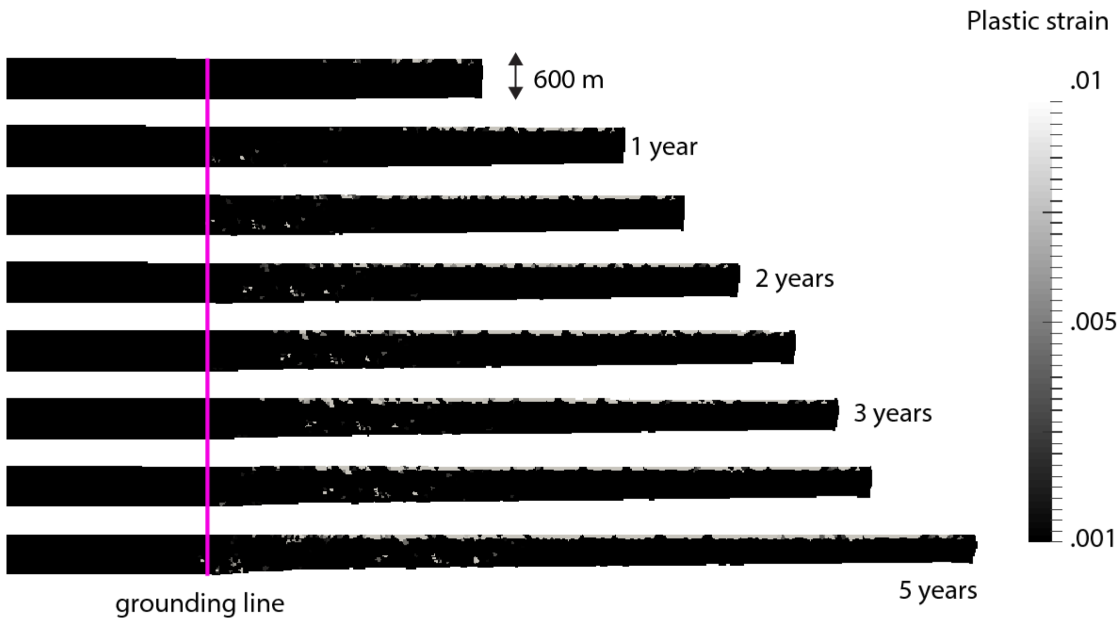

Figure 3.7: Plastic strain field for 600 m thick ice over 5 years real model runtime. Ice fails in tension at the surface near the terminus, and sporadically at the base.

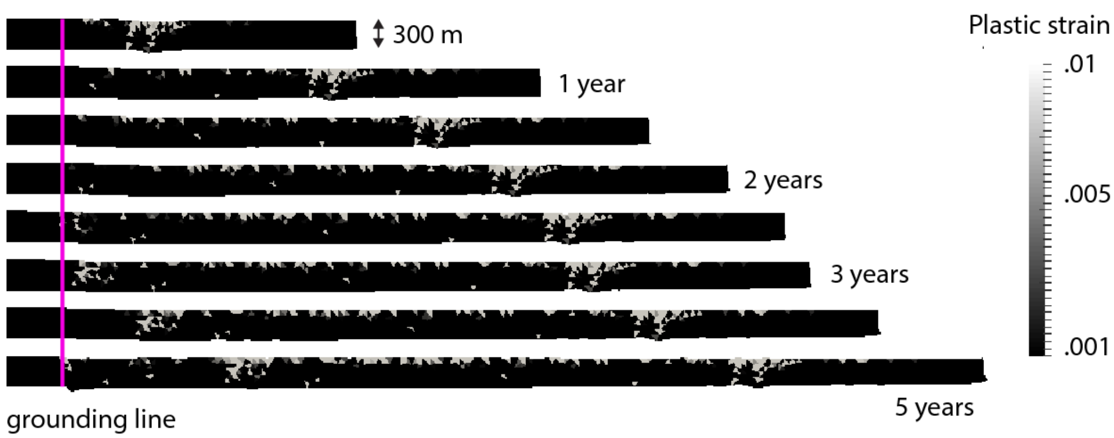

Figure 3.8: Plastic strain field for 300 m thick ice over 5 years real model runtime. Ice fails in tension at the surface near the terminus, and sporadically at the base.

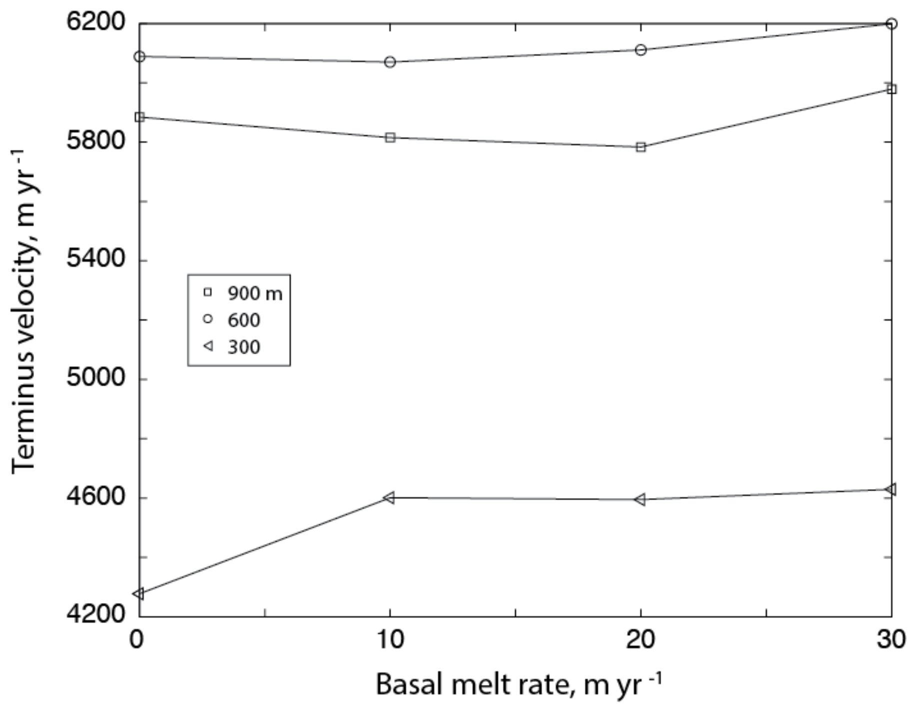

Figure 3.9: Terminus velocity for all three ice thicknesses versus melt rate after 6 months real model run time. Again ice velocity increases with increasing melt rate, however the thickest ice does not show the highest velocity and velocities are on average about 1000 m yr^{-1} lower than for Maxwell ice.

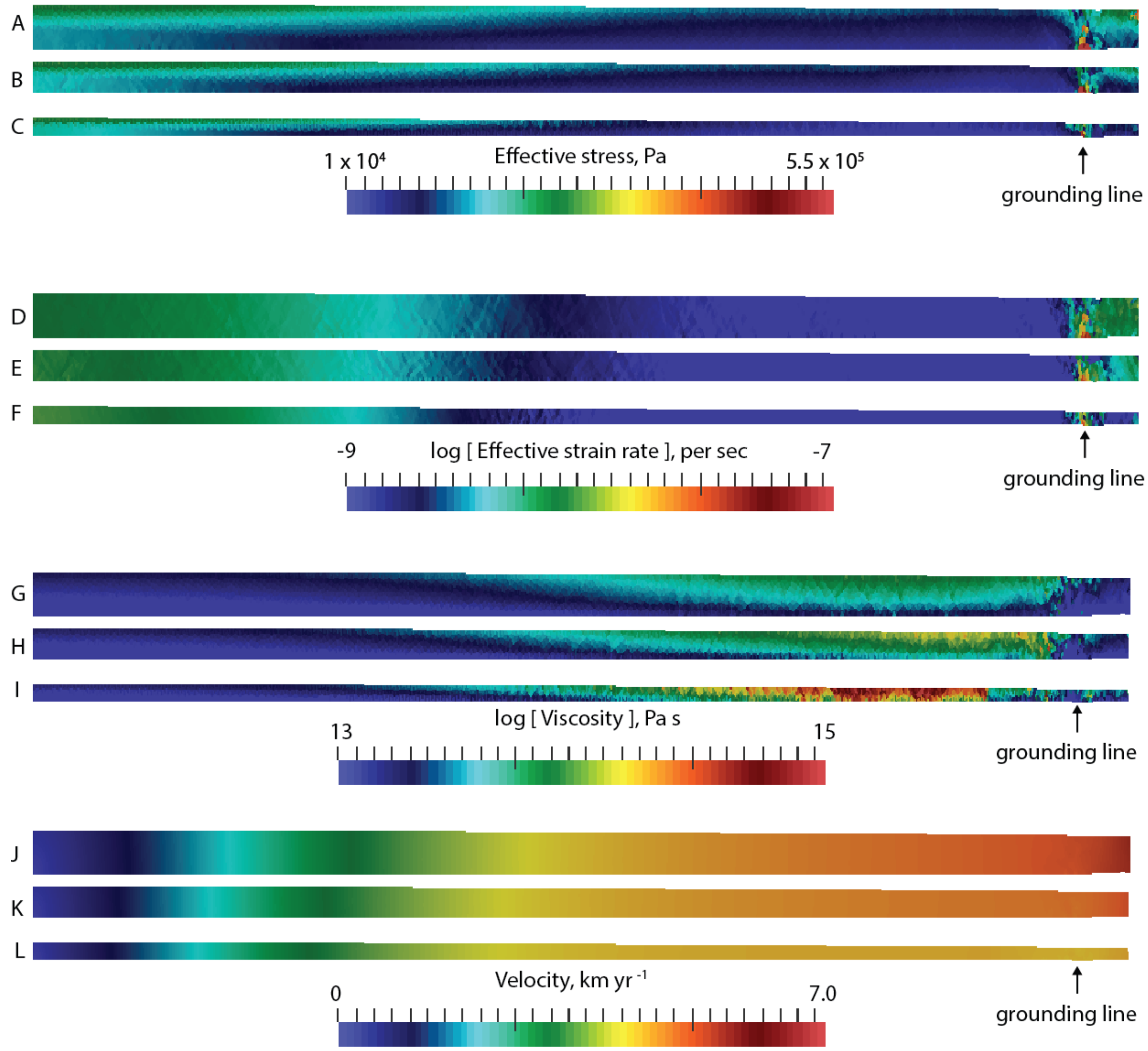

Figure 3.10: Outputs for visco-elasto-plastic ice with additional water-saturation failure after 6 months real model run time. [A-C] Effective stress, [D-F], effective strain rate, [G-I] viscosity, and [J-L] velocity for all three ice thicknesses with no applied basal melt. The grounding line is indicated by the black arrow.

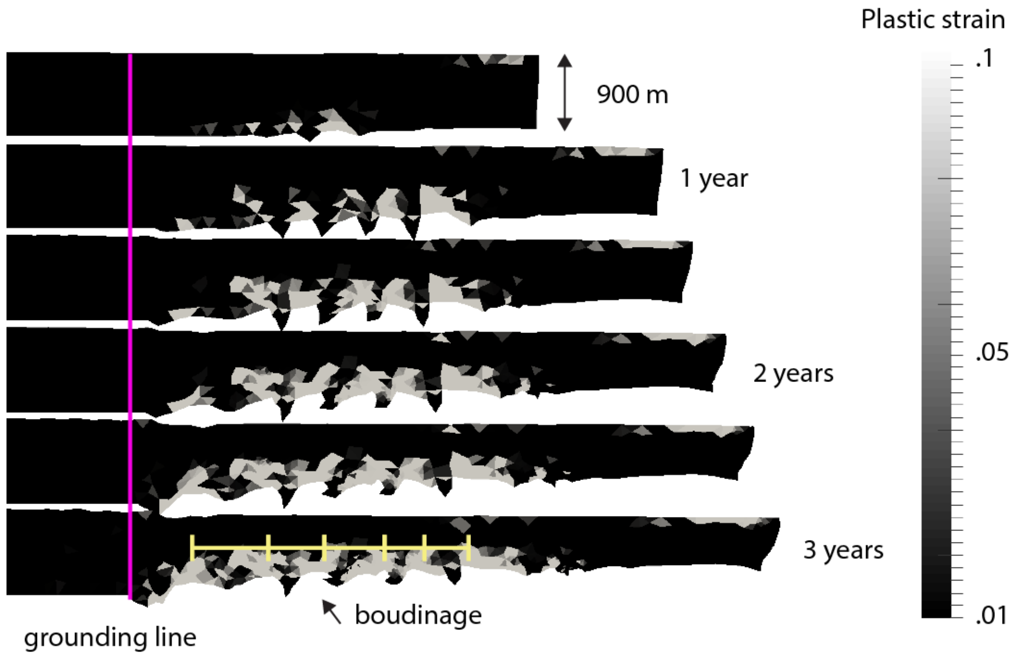

Figure 3.11: Plastic strain field for 900 m thick ice over 3 years real model runtime. Ice fails in tension at the surface near the terminus, but now fails with regularity at the grounding line where hydrostatic stress is applied (in pink). Ice forms boudin-like features after accommodating a large amount of strain.

Figure 3.12: Plastic strain field for 600 m thick ice over 3 years real model runtime. Ice fails in tension at the surface near the terminus, but now fails with regularity at the grounding line where hydrostatic stress is applied (in pink). Ice forms boudin-like features after accommodating a large amount of strain.

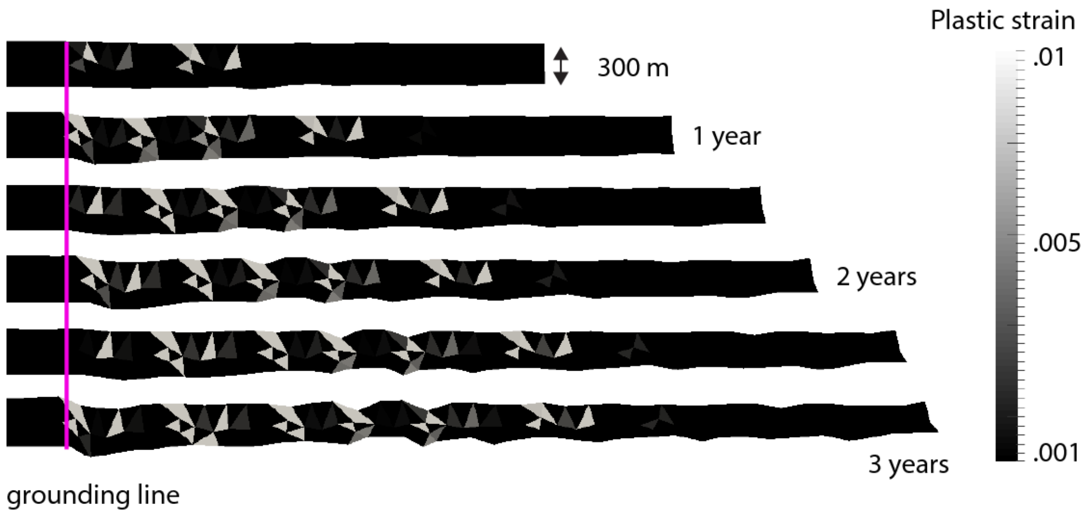

Figure 3.13: Plastic strain field for 300 m thick ice over 3 years real model runtime. Ice fails in tension at the surface near the terminus, but now fails with regularity at the grounding line where hydrostatic stress is applied (in pink). Surface and bottom features now propagate far enough through the ice thickness to be considered full thickness rifts.

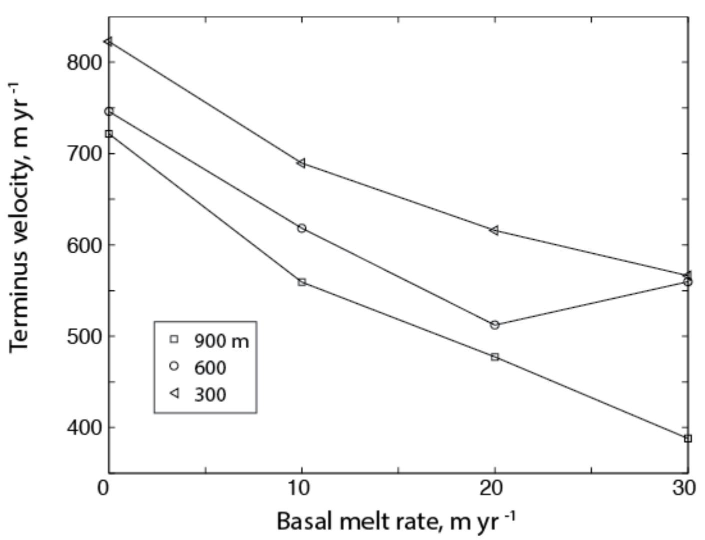

Figure 3.14: Terminus velocity for all three ice thicknesses versus melt rate after 6 months real model run time. For these simulations ice velocity does not appear to increase with increasing melt rate.

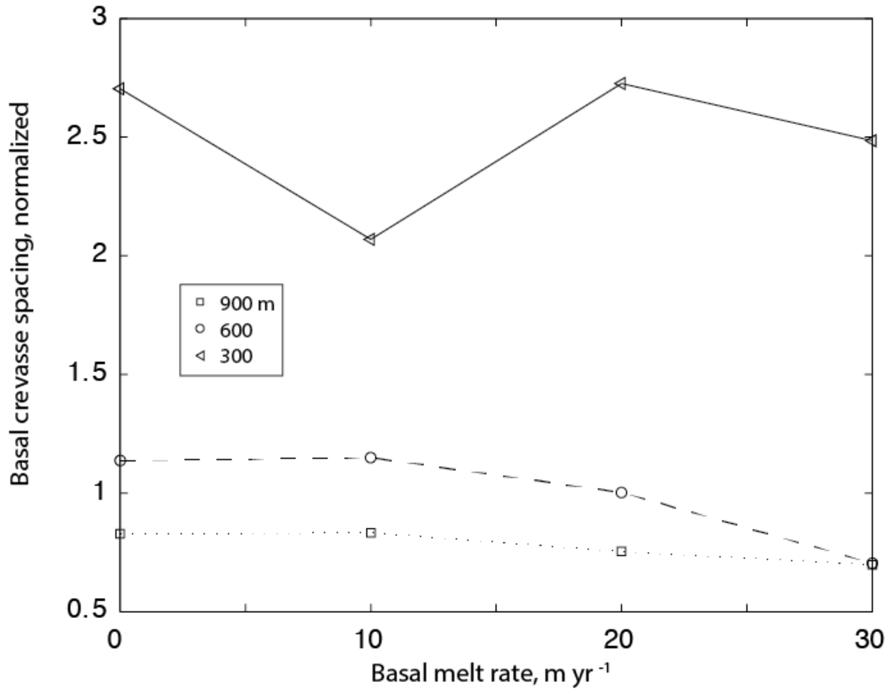

Figure 3.15: Basal crevasse spacing normalized to local ice thickness. Spacing mostly decreases with increasing melting. The thinnest ice has the largest basal crevasse spacing

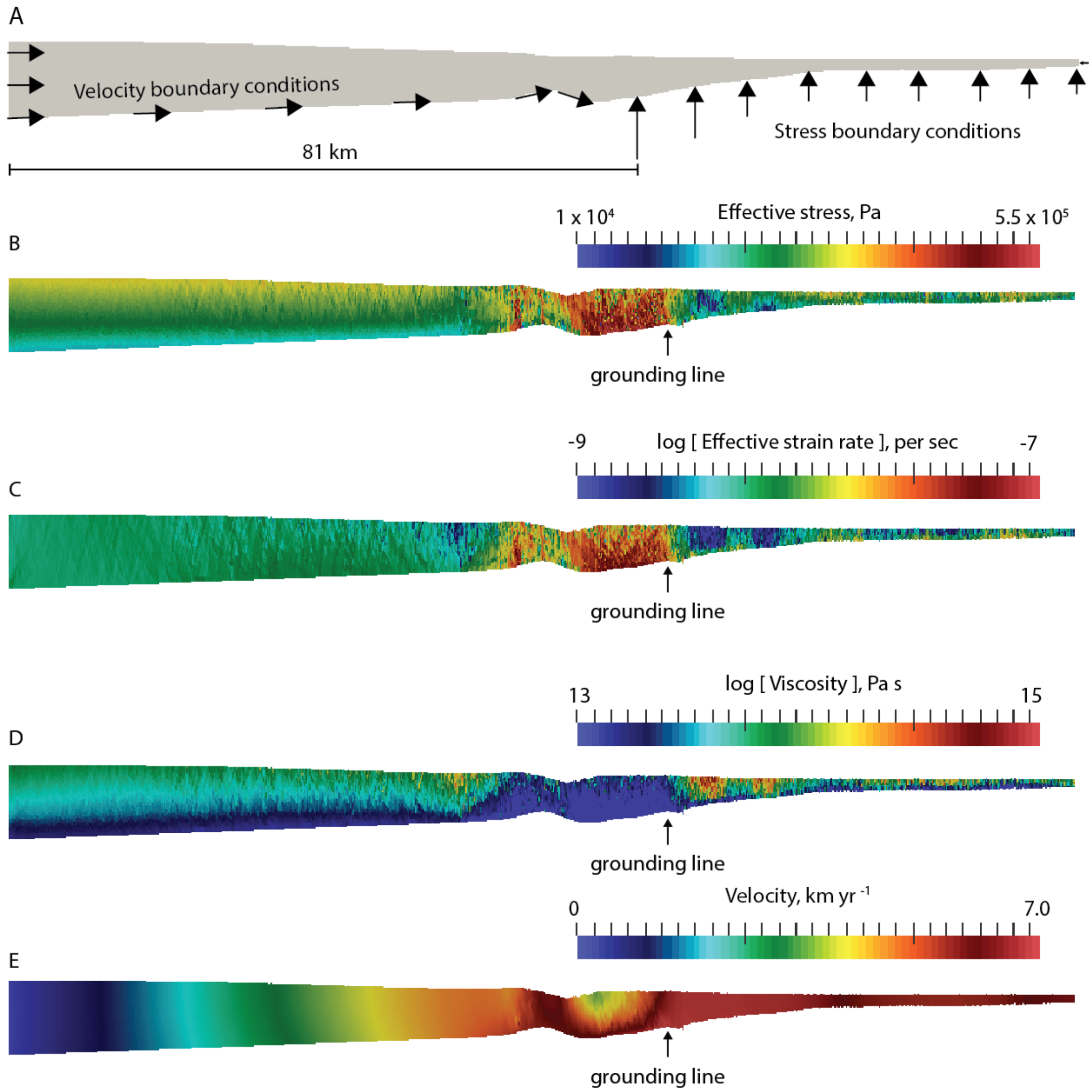

Figure 3.16: [A] Initial geometry, [B] effective stress, [C] effective strain rate, [D] viscosity, and [E] velocity for Thwaites Glacier after 2 years real model runtime. Bedrock topography has a great deal of influence over the resulting fields shown here, emphasizing how important this feature of glacier flow is. The ice tongue has a high viscosity, implying that it acts as one brittle unit.

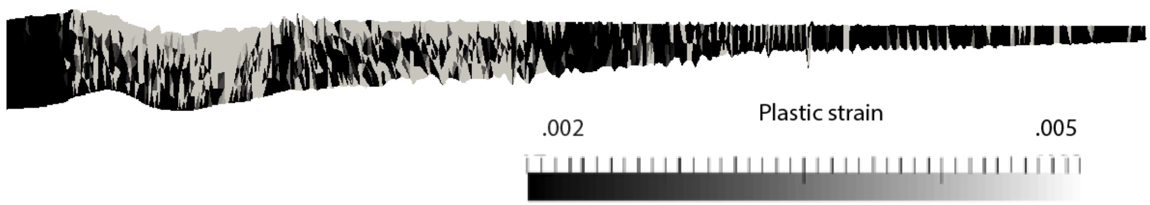

Figure 3.17: Plastic strain field for the Thwaites Glacier tongue after 5 years real model runtime. Present are numerous basal crevasses with an average spacing of 1588 m. A boundin-like structure appears after this time that does not largely coincide with the locations of basal crevasses, with an average spacing of 729 m.

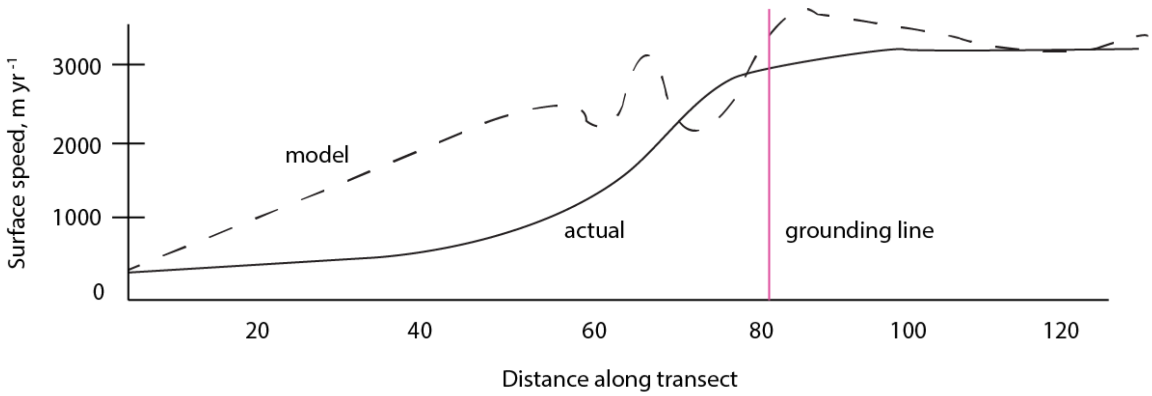

Figure 3.18: Comparison between model-derived surface velocities and actual velocities of Thwaites Glacier (Rignot et al., 2012). That DES overpredicts the velocity in the first 60 km of the domain is due to the fixed velocities there where a linear gradient in velocity is applied, and the basal topography is smoothed compared to data (Figure 19). The large bump in topography upstream of the grounding line impacts the flow with as it provides a resistive force.

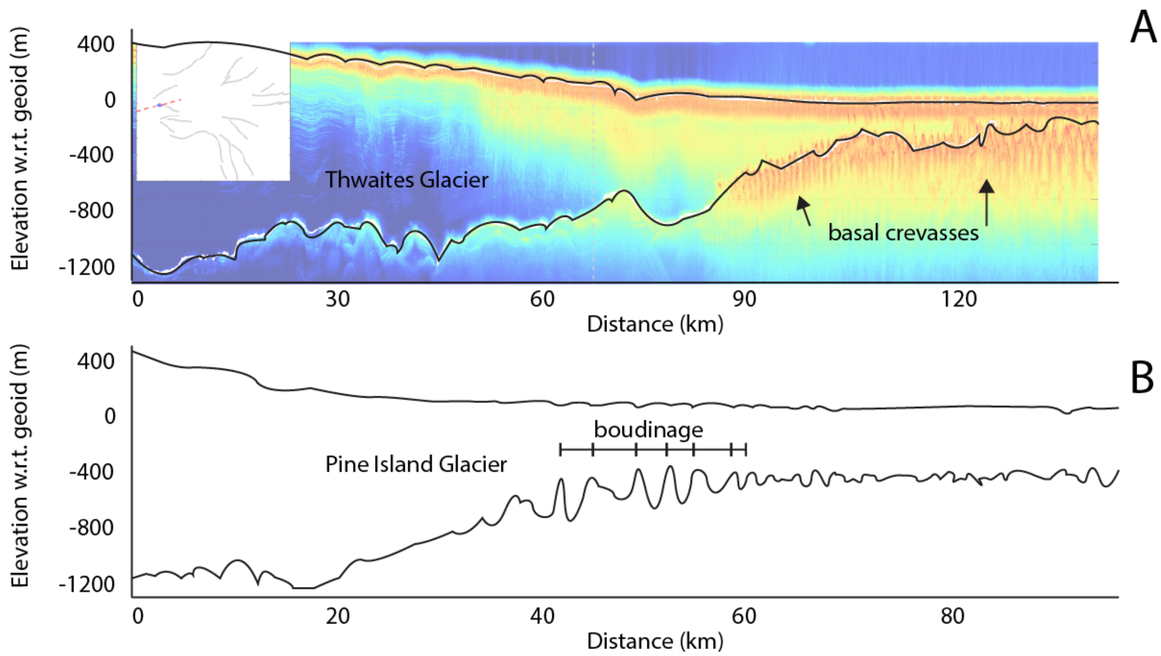

Figure 3.19: Geometry of [A] Thwaites (personal correspondence, Joe MacGregor) and [B] Pine Island Glaciers (adapted from Bindschadler et al., 2011). Boudinage seen provided for comparison to Thwaites Glacier (shown from above in Figure 1) and a simulation of the formation of boudins of Thwaites Glacier (Figure 17). Several very large boudins are seen between 40 and 60 km, of about 400 m high into the floating tongue and spaced every several km.

Conclusion

The goal of this dissertation research was to further develop our understanding of the connection between ice flow and failure, with the ultimate objective of formulating a numerical model that could simulate the calving of ice. A key element in this work was the study of ice rheology.

In Chapter 1 we found that – through the observation of basal crevasses at ice stream grounding lines in Antarctica – elasticity is an oft-ignored yet key aspect of ice failure. We found that, while extremely simple, the use of a thin elastic beam to approximate stresses at grounding lines around Antarctica provided order-of-magnitude predictions for the height of basal crevasses formed by bending. This motivated our study in Chapter 2, which examined the difference in flow and failure of ice using a visco-elasto-plastic rheology. Because our findings in Chapter 1 revealed that basal crevasse propagation height depends on ice thickness and ice bending, we simulated elastoplastic ice advecting over a static grounding line for a range of ice thicknesses and tilt degrees. We found that thicker ice produced wider spaced zones of failure, and that glaciers that experience higher levels of bending produce more closely spaced basal crevasses. We also established Mohr-Coulomb parameters that provided reasonable failure patterns. Lastly, we found that a visco-elasto-plastic rheology where the minimum energy principle was used to select either the Maxwell viscoelastic or Mohr-Coulomb elastoplastic almost always resulted in a simulation that was entirely viscoelastic: that is, the viscoelastic stress was always smaller than the elastoplastic stress.

To overcome this problem we tested the effect that the inclusion of a ductile-brittle transition based on longitudinal strain rate would have on the pattern of brittle failure in the ice. Laboratory experiments indicate that when ice is straining quickly it fails in a brittle manner and behaves in a ductile manner when flowing slowly. We approximated the ductile and brittle deformation of ice using Maxwell viscoelasticity and Mohr-Coulomb elastoplasticity and found, when subject to a transition in boundary conditions simulating a grounding line, that basal crevasses – represented by zones of brittle failure – formed with the regularity often seen in nature. These crevasses developed however only with the inclusion of an extra measure of weakening that represents the infiltration of buoyant ocean water in basal cracks. The failed ice, being weaker, has a lower viscosity and starts to neck, forming the boudin-like patterns seen in many floating ice tongues around the world, including Thwaites and Pine Island Glaciers. We applied a range of melting rates to floating tongues subject to hydrostatic stresses and observed several key findings: 1 – that a ductile-brittle rheological transition based on longitudinal strain rate *and* extra ice weakening due to water-filled cracks are necessary for the realistic simulation of the formation and development of basal crevasses; 2 – that thinner ice produces relatively wider spaced crevasses; 3 – basal topography is extremely important in order to resolve the changes in the stress field near the grounding line; 4 – that in order to properly simulate the velocity increases due to basal melting a numerical model must incorporate a freely-evolving grounding line. Future work with DynEarthSol3D will proceed after this has been developed within the model.

References

Albrecht, T., Martin, M., Haseloff, M., Winkelmann, R., and Levermann, A. (2011) Parameterization for subgrid-scale motion of ice-shelf calving-fronts, *Cryosphere*, **5**(1), 35–44, doi: 10.5194/tc-5-35- 2011

Albrecht, T. and Levermann, A. (2012) Fracture field for large-schale ice dynamics, *J. Glaciol.*, *58*, doi: 10.3189/2012JoG11J191

Alley, R.B., and 7 others (2008) A simple law for ice-shelf calving. *Science*, **322**(5906), 1344, doi: 10.1126/science.1162543

Amundsen, J. and Truffer, M. (2010) A unifying framework for iceberg-calving models, *J. Glaciol.*, *56*, 822 – 830

Bassis, J., Fricker, H., Coleman, R., and Minster, J.-B. (2008) An investigation into the forces that drive ice-shelf rift propagation on the Amery Ice Shelf, East Antarctica, *J. Glaciol.*, *54*, 17 – 27

Bassis, J. N., and Jacobs, S. (2013) Diverse calving patterns linked to glacier geometry, *Nat. Geosci.*, 6, 833–836, doi:10.1038/NGEO1887

Benn, D. I., Warren, C. R., and Mottram, R. H. (2007) Calving processes and the dynamics of calving glaciers. *Earth Sci. Rev.* **82,** 143–179

Bindschadler, R. (1983) The importance of pressurized subglacial water in separation and sliding at the glacier bed. *J. Glaciol.*, **29**(101), 3–19

Bindschadler, R., Vaughan, D.G., and Vornberger, P. (2011) Variability of basal melt beneath the Pine Island Glacier ice shelf, West Antarctica. *J. Glaciol.*, **57**(204), 581–595, doi: 10.3189/ 002214311797409802

Bodine, J.H., and Watts, A.B. (1979) On lithospheric flexure seaward of the Bonin and Marina Trenches. *Earth Planet. Sci. Lett.*, **43**(1), 132–148

Braun, M., Humbert, A., and Moll, A. (2009) Changes of Wilkins Ice Shelf over the past 15 years and inferences on its stability. *Cryosphere*, **3**(1), 41–56, doi: 10.5194/tc-3-41-2009

Brunt, K.M., King, M.A., Fricker, H.A., and MacAyeal, D.R. (2010a) Flow of the Ross Ice Shelf, Antarctica, is modulated by the ocean tide. *J. Glaciol.*, **56**(195), 157–161, doi: 10.3189/ 002214310791190875

Brunt, K.M., Fricker, H.A., Padman, L., Scambos, T.A., and O'Neel, S. (2010b) Mapping the grounding zone of Ross Ice Shelf, Antarctica, using ICESat laser altimetry. *Ann. Glaciol.*, **51**(55), 71–79, doi: 10.3189/172756410791392790

Burnett, A., Leventer, A., Conley, P., Kirby, M., and Bindschadler, R. eds. *Antarctic Peninsula climate variability: a historical and paleo- environmental perspective.*

(Antarctic Research Series 79) American Geophysical Union, Washington, DC, 79–92

Catania, G.A., Conway, H., Raymond, C.F., and Scambos, T.A. (2006) Evidence for floatation or near floatation in the mouth of Kamb Ice Stream, West Antarctica, prior to stagnation. *J. Geophys. Res.*, **111**(F1), F01005, doi: 10.1029/2005JF000355

Catania, G.A., Hulbe, C.L., and Conway, H.B. (2010) Grounding-line basal melt rates determined using radar-derived internal stratig- raphy. *J. Glaciol.*, **56**(197), 545–554, doi: 10.3189/ 002214310792447842

Cavaliero, D.J., and Ivanoff, A. (2009) *AMSRice03 Landsat-7 ETM+ Imagery*. National Snow and Ice Data Center, Boulder, CO. Digital media: http://nsidc.org/api/metadata?id=nsidc-0431

Choi, E., Tan, E., Lavier, L., and Calo, V. (2013) DynEarthSol2D: An efficient unstructured finite element method to study long-term tectonic deformation, *J. Geophys. Res.*, *118*, doi: 10.1002/jgrb.50148

Conway, H., Hall, B.L., Denton, G.H., Gades, A.M., and Waddington, E.D. (1999) Past and future grounding-line retreat of the West Antarctic ice sheet. *Science*, **286**(5438), 280–283, doi: 10.1126/science.286.5438.280

Cundall, P. A. (1989) Numerical experiments on localization in frictional materials, *Ing. Arch.*, *58*, 148 – 159

De Micheli, P. O., and Mocellin, K. (2009) A new efficient explicit formulation for linear tetrahedral elements non-sensitive to volumetric locking for infinitesimal elasticity and inelasticity, *Int. J. Numer. Methods Eng.*, *79*, 45 – 68, doi: 10.1002/nme.2539

Detournay, C., and Dzik, E. (2006) Nodal mixed discretization for tetrahedral elements, in *4th International FLAC Symposium on Numerical Modeling in Geomechanics*, edited by Hart, and Varona, col. C, Itasca Consulting Group, Inc., Minneapolis.

Doake, C.S.M., and Vaughan, D.G. (1991) Rapid disintegration of the Wordie Ice Shelf in response to atmospheric warming. *Nature*, **350**(6316), 328–330, doi: 10.1038/350328a0

Doake, C.S.M., Corr, H.F.J., Rott, H., Skvarca, P., and Young, N.W. (1998) Breakup and conditions for stability of the northern Larsen Ice Shelf, Antarctica. *Nature*, **391**(6669), 778–780, doi: 10.1038/ 35832

Duddu, R., and Waisman, H. (2013) A nonlocal continuum damage mechanics approach to simulation of creep fracture in ice sheets. *Comput. Mech.*, 51(6), 961–974, doi: 10.1007/s00466- 012-0778-7

Favier, L., Gagliardini, O., Durand, G., and Zwinger, T. (2012) A three- dimensional full Stokes model of the grounding line dynamics: effect of a pinning point beneath the ice shelf. *Cryosphere*, **6**(1), 101–112, doi: 10.5194/tc-6-101-2012

Fish, A., and Zaretsky, Y. (1997) Strength and creep of ice in terms of Mohr-Coulomb fracture theory, *Proc. Of the Eighth International Offshore and Polar Engineering Conf., Montreal, Canada, May 24 – 29*

Gagliardini, O., and Zwinger, T. (2008) The ISMIP-HOM benchmark experiments performed using the Finite-Element code Elmer, *Cryosphere*, *2*, 67 – 76

Gammon, P.H., Kiefte, H., Clouter, M.J., and Denner, W.W. (1983) Elastic constants of artificial and natural ice samples by Brillouin spectroscopy. *J. Glaciol.*, **29**(103), 433–460

Glasser, N. and Scambos, T. (2008) A structural glaciological analysis of the 2002 Larsen B ice-shelf collapse, *J. Glaciol.*, *29*, doi: 103189/002214308784409017

Glen, J.W. (1955) The creep of polycrystalline ice. *Proc. R. Soc. London, Ser. A*, **228**(1175), 519–538

Goldsby, D.L., and Kohlstedt, D.L. (2001) Superplastic deformation of ice: experimental observations. *J. Geophys. Res.*, **106**(B6), 11 017–11 030, doi: 10.1029/2000JB900336

Haran, T., Bohlander, J., Scambos, T., Fahnestock, M., and compilers (2005) *MODIS mosaic of Antarctica (MOA) image map*. National Snow and Ice Center, Boulder, CO. Digital media: http://nsidc.org/data/nsidc-0280.html

Hindmarsh, R.C.A. (2004) A numerical comparison of approximations to the Stokes equations used in ice sheet and glacier modeling. *J. Geophys. Res.*, **109**(F1), F01012, doi: 10.1029/2003JF000065

Horgan, H.J., and Anandakrishnan, S. (2006) Static grounding lines and dynamic ice streams: evidence from the Siple Coast, West Antarctica. *Geophys. Res. Lett.*, **33**(18), L18502, doi: 10.1029/ 2006GL027091

Hughes, T. (1983) On the disintegration of ice shelves: the role of fracture. *J. Glaciol.*, **29**(101), 98–117

Hughes, T. J. (2000) *The Finite Element Method: Linear Static and Dynamic Finite Element Analysis*, 672 pp., Dover Publication, reprint of the Prentice-Hall, Inc., Englewood Cliffs, New Jersey, 1987 edition

Jacobs, S., and 6 others (2012) The Amundsen Sea and the Antarctic Ice Sheet. *Oceanography*, **25**(3), 154–163, doi: 10.5670/ oceanog.2012.90

James, T. D., T. Murray, N. Selmes, K. Scharrer, and O'Leary, M. E. (2014) Buoyant flexure and basal crevassing in dynamic mass loss at Helheim Glacier, *Nat. Geosci.*, 7, 593–596, doi:10.1038/ngeo2204

Jezek, K.C., and Bentley, C.R. (1983) Field studies of bottom crevasses in the Ross Ice Shelf, Antarctica. *J. Glaciol.*, **29**(101), 118–126

Joughin, I., and 7 others (2008) Continued evolution of Jakobshavn Isbrae following its rapid speedup. *J. Geophys. Res.*, **113**(F4), F04006, doi: 10.1029/2008JF001023

Kenneally, J.P., and Hughes, T. (2006) Calving giant icebergs: old principles, new applications. *Antarct. Sci.*, **18**(3), 409–419, doi: 10.1017/S0954102006000459

Khazendar, A., and Jenkins, A. (2003) A model of marine ice formation within Antarctic ice shelf rifts. *J. Geophys. Res.*, **108**(C7), 3235, doi: 10.1029/2002JC001673

Langhorne, P.J. and Haskell, T.G. (2004) The flexural strength of partially refrozen cracks in sea ice. In Chung JS, Izumiyama K, Sayed M and Hong SW eds. *Proceedings of the 14th Inter- national Offshore and Polar Engineering Conference, 23–28 May, 2004, Toulon, France*. International Society of Offshore and Polar Engineers, Cupertino, CA, 819–824

Larour, E., Seroussi, H., Morlighem, M., and Rignot, E. (2012) Continental scale, high order, high spatial resolution, ice sheet modeling using the Ice Sheet System Model (ISSM), *J. Geophys. Res., 117*, F01022, doi:10.1020/2011JF002140

Le Brocq, A.M., Payne, A.J., and Vieli, A. (2010) An improved Antarctic dataset for high resolution numerical ice sheet models (ALBMAP v1). *Earth Syst. Sci. Data*, **2**(2), 247–260, doi: 10.5194/essdd-3-195-2010

Le Meur, E., Gagliardini, O., Zwinger, T., and Ruokolainen, J. (2004) Glacier flow modelling: a comparison of the Shallow Ice Approximation and the full-Stokes equation. *C. R. Phys.*, **5**(7), 709–722

Levermann, A., Albrecht, T., Winkelmann, R., Martin, M. A., Haseloff, M., and Joughin, I. (2012), Kinematic first-order calving law implies potential for abrupt ice-shelf retreat, *Cryosphere*, *6*, doi: 10.5194/tc-6-273-2012

Logan, L., Catania, G., Lavier, L., and Choi, E. (2013), A novel method for predicting fracture in floating ice, *J. Glac.*, *59*, doi: 10.3189/2013JoG12J210

Lipscomb, W.H., Fyke, J., Vizcaino, M., Sacks, W., Wolfe, Vertenstein, J.M., Craig, A., Kluzek, E., and Lawrence, D. (2013) Implementation and initial evaluation of the Glimmer Community Ice Sheet Model in the Community Earth System Model, *J Climate*, *26*, doi:10.1175/JCLI-D_12-00557.1

Liu, Y., Moore, J.C., Cheng, X., Gladstone, R.M., Bassis, J.N., Liu, H., Wen, J., Hui, F. (2015) Ocean-driven thinning enhances iceberg calving and retreat of Antarctic ice shelves, *PNAS*, doi:10.1073/pnas.1415137112

Lubliner, J. (1990), *Plasticity Theory*, 495 pp., Macmillan, New York

Luckman, A., Jansen, D., Kulessa, B., King, E.C., Sammonds, P. and Benn, D.I. (2012) Basal crevasses in Larsen C Ice Shelf and implications for their global abundance. *Cryosphere*, **6**(1), 113–123, doi: 10.5194/tc-6-113-2012

MacAyeal, D.R., Scambos, T.A., Hulbe, C.L., and Fahnestock, M.A. (2003) Catastrophic ice-shelf break-up by an ice-shelf-fragment- capsize mechanism. *J. Glaciol.*, **49**(164), 22–36, doi: 10.3189/ 172756503781830863

MacAyeal, D. R. and Sergienko, O. V. (2013) The flexural dynamics of melting ice shelves, *Ann. Glac.*, 54(63), doi: 10.3189/2013AoG63A256

MacGregor, J.A., Anandakrishnan, S., Catania, G.A., and Winebrenner, D.P. (2011) The grounding zone of the Ross Ice Shelf, West Antarctica, from ice-penetrating radar. *J. Glaciol.*, **57**(205), 917–928, doi: 10.3189/002214311798043780

Martin, C., Navarro. F., Otero, J., Cuadrado, M., and Corcuera, M. (2004) Three-dimensional modeling of the dynamics of Johnsons Glacier, Livingston Island, Antarctica, *Ann. Glaciol.*, *39*, 1 – 8.

McGrath, D., Steffen, K., Scambos, T., Rajaram, H., Casassa, G., and Rodriguez Lagos, J. (2012a) Basal crevasses and associated surface crevassing on the Larsen C ice shelf, Antarctica, and their role in ice-shelf instability. *Ann. Glaciol.*, **53**(60 Pt 1), 10–18, doi: 10.3189/2012AoG60A005

McGrath, D., Steffen, K., Rajaram, H., Scambos, T., Abdalati, W., and Rignot, E. (2012b) Basal crevasses on the Larsen C Ice Shelf, Antarctica: implications for meltwater ponding and hydrofracture. *Geophys. Res. Lett.*, **39**(16), L16504, doi: 10.1029/2012GL052413

Mottram, R.H., and Benn, D.I. (2009) Testing crevasse-depth models: a field study at Breiðamerkurjo ̈kull, Iceland. *J. Glaciol.*, **55**(192), 746–752, doi: 10.3189/002214309789470905

Mulmule, S. V., and Dempsey, J. P. (1998) A viscoelastic fictitious crack model for the fracture of sea ice, *Mech. of Time-Dependent Mat.*, 1, 331 – 356

Murray, T., Selmes, N., James, T.D., Edwards, S., Martin, I., O'Farrell, T., Aspey, R., Rutt, I., Nettles, M., and Bauge, T. (2015) Dynamics of glacier calving at the ungrounded margin of Helheim Glacier, southeast Greenland, *J. Geophys. Res. Earth Surf.*, 120, doi:10.1002/2015JF003531

Nye JF (1955) Correspondence. Comments on Dr. Loewe's letter and notes on crevasses. *J. Glaciol.*, **2**(17), 512–514

Pattyn, R., et al. (2008) Benchmark experiments for higher-order and full-stokes ice sheet models (ISMIP-HOM), *Cryosphere*, *2*, 95 – 108

Payne, A., and Baldwin, D. (2000) Analysis of ice-flow instabilities identified in the EISMINT intercomparison exercise, *Ann. Glac.*, 30, 204 – 210

Pelto, M. S., and Warren, C. R. (1991) Relationship between tidewater glacier calving velocity and water depth at the calving front, *Ann. Glaciol.*, 15, 115–118

Pralong, A., Hutter, K., and Funk, M. (2006) Anisotropic damage mechanics for viscoelastic ice, *Continuum Mech. Thermodyn.*, 17(5), 387 – 408, doi: 10.1007/s00161-005-0002-5

Rignot, E., and Jacobs, S.S. (2002) Rapid bottom melting widespread near Antarctic ice sheet grounding lines. *Science*, **296**(5575), 2020–2023, doi: 10.1126/science.1070942

Rignot, E., Casassa, G., Gogineni, P., Krabill, W., Rivera, A., and Thomas, R. (2004) Accelerated ice discharge from the Antarctic Peninsula following the collapse of the Larsen B ice shelf, *Geophys. Res. Let.*, 31, L18401, doi:10.1029/2004GL020697

Rignot, E., Mouginot, J., and Scheuchl, B. (2011) Ice flow of the Antarctic Ice Sheet. *Science*, **333**(6048), 1427–1430, doi: 10.1126/science.1208336

Rignot, E., Jacobs, S., Mouginot, J., Scheuchl, B. (2013) Ice-shelf melting around Antarctica, *Science*, 341, 266 - 270

Rist, M.A., Sammonds, P.R., Oerter, H., and Doake, C.S.M. (2002) Fracture of Antarctic shelf ice. *J. Geophys. Res.*, **107**(B1), 2002, doi: 10.1029/2000JB000058

Rott, H., Muller, F., Nagler, T., and Floricioiu, D. (2011) The imbalance of glaciers after disintegration of Larsen-B ice shelf, Antarctic Peninsula. *Cryosphere*, **5**(1), 125–134, doi: 10.5194/tc- 5-125-2011

Rutt, I.C., Hagdorn, M., Hulton, N.R.J., and Payne, A.J. (2009) The Glimmer community ice sheet model. *J. Geophys. Res.*, **114**(F2), F02004, doi: 10.1029/2008JF001015

Sayag, R., and Worster, M.G. (2011) Elastic response of a grounded ice sheet coupled to a floating ice shelf. *Phys. Rev. E*, **84**(3), 036111, doi: 10.1103/PhysRevE.84.036111

Scambos, T., Hulbe, C., and Fahnestock, M. (2003) Climate-induced ice shelf disintegration in the Antarctic Peninsula. In Domack EW

Scambos., T.A., Bohlander, J.A., Shuman, C.A., Skvarca, P. (2004) Glacier acceleration and thinning after ice shelf collapse in the Larsen B embayment, Antarctica, *Geophys. Res. Let.*, 31, L18402, doi:10.1029/2004GL020670

Scambos, T., and 7 others (2009) Ice shelf disintegration by plate bending and hydro-fracture: satellite observations and model results of the 2008 Wilkins ice shelf break-ups. *Earth Planet. Sci. Lett.*, **280**(1–4), 51–60, doi: 10.1016/j.epsl.2008.12.027

Schoof, C. (2007) Ice sheet grounding line dynamics: steady states, stability, and hysteresis. *J. Geophys. Res.*, **112**(F3), F03S28, doi: 10.1029/2006JF000664

Schoof, C. (2011) Marine ice sheet dynamics. Part 2. A Stokes flow contact problem. *J. Fluid Mech.*, **679**, 122–155, doi: 10.1017/ jfm.2011.129

Schulson, E.M. (2006) The fracture of water ice Ih: a short overview, *Meteorites and Plan. Sci.*, 41, 1497 - 1508

Schulson, E.M., and Duval, P. (2009) *Creep and fracture of ice*. Cambridge University Press, Cambridge

Sergienko, O., and MacAyeal, D.R. (2005) Surface melting on Larsen Ice Shelf, Antarctica. *Ann. Glaciol.,* **40**, 215–218, doi: 10.3189/ 172756405781813474

Shepherd, A., Wingham, D.J., Mansley, J.A.D., and Corr, H.F.J. (2001) Inland thinning of Pine Island Glacier, West Antarctica. *Science*, **291**(5505), 862–864, doi: 10.1126/science.291.5505.862

Shewchuk, J. (1996) Triangle: Engineering a 2D quality mesh generator and Delaunay triangulator, in *Applied Computational Geometry: Towards Geometric Engineering, Lecture Notes in Computer Science,* edited by M. C. Lin, and D. Manocha, pp. 203 – 222, vol. 1148, Springer-Verlag, Berlin

Simo, J. C., and Hughes, T. J. R. (2004), *Computational Inelasticity*, Springer, New York

Timoshenko, S.P., and Woinowsky-Krieger, S. (1959) *Theory of plates and shells*, 2nd edn. McGraw-Hill, New York

Turcotte, D.L., and Schubert, G. (1982) *Geodynamics: appli- cations of continuum physics to geological problems*. Wiley, New York

Van der Veen, C. J. (1996) Tidewater calving, *J. Glaciol.*, 42(141), 375–385

Van der Veen, C.J. (1998a) Fracture mechanics approach to penetration of surface crevasses on glaciers, *Cold Reg. Sci. Tech.*, *27*, 31 – 47

Van der Veen, C.J. (1998b) Fracture mechanics approach to penetration of bottom crevasses on glaciers. *Cold Reg. Sci. Technol.*, **27**(3), 213–223, doi: 10.1016/S0165-232X(98)00006-8

Vaughan, D.G. (1993) Relating the occurrence of crevasses to surface strain rates. *J. Glaciol.*, **39**(132), 255–266

Vaughan, D.G. (1995) Tidal flexure at ice shelf margins. *J. Geophys. Res.*, **100**(B4), 6213–6224, doi: 10.1029/94JB02467

Vaughan, D.G., and 8 others (2012) Subglacial melt channels and fracture in the floating part of Pine Island Glacier, Antarctica. *J. Geophys. Res.*, **117**(F3), F03012, doi: 10.1029/2012JF002360

Walter, J.I., Brodsky, E.E., Tulaczyk, S., Schwartz, S.Y., and Pettersson, R. (2011) Transient slip events from near-field seismic and geodetic data on a glacier fault, Whillans Ice Plain, West Antarctica. *J. Geophys. Res.*, **116**(F1), F01021, doi: 10.1029/2010JF001754

Weertman, J. (1973) Can a water-filled crevasse reach the bottom surface of a glacier? *IASH Publ.* 95 (Symposium at Cambridge 1969 – *Hydrology of Glaciers*), 139–145

Weiss, J. (2004) Subcritical crack propagation as a mechanism of crevasse formation and iceberg calving, *J. Glaciol.*, *50*, 109 – 115

Wilkins, M. L. (1964) Calculations of elastic-plastic flow, in *Methods in Computational Physics*, edited by B. Alder, S. Fermback, and M. Rotenberg, pp. 211 – 264, Academic Press, New York

Winberry, J.P., Anandakrishnan, S., Alley, R.B., Bindschadler, R.A., and King, M.A. (2009) Basal mechanics of ice streams: insights from the stick– slip motion of Whillans Ice Stream, West Antarctica. *J. Geophys. Res.*, **114**(F1), F01016, doi: 10.1029/2008JF001035